LONGITUDINAL INTRAVITAL MULTIPHOTON MICROENDOSCOPY IN THE BONE MARROW OF MICE

Inaugural-Dissertation

to obtain the academic degree

Doctor rerum naturalium (Dr. rer. nat.)

submitted to the Department of Biology, Chemistry and Pharmacy

of Freie Universität Berlin

by

DAVID REISMANN

from Oelde

2018

This work was carried out in the period from September 1st, 2014 to January 14th, 2018 at the German Rheumatism Research Center in Berlin in the research group "Biophysical Analytics" headed by Dr. rer. nat. Raluca A. Niesner.

1st Reviewer: Professor Dr. med. vet. Anja E. Hauser

2nd Reviewer: Professor Dr. Ing. Georg N. Duda

Date of disputation: June 7th, 2018

Acknowledgment

I would like to express my sincere thanks to Dr. Raluca Niesner for her outstanding mentoring, the numerous creative discussions and paving my way at the Institute. I really enjoyed working with her.

I would also like to thank Prof. Dr. Anja Hauser, who was equally enthusiastic about the subject of my work and who repeatedly motivated me in scientific discourses, and Prof. Dr. Georg Duda, to whom I am particularly grateful for supervision and excellent support on the field of regeneration.

My special thanks go to Jonathan Stefanowski and Robert Günther. Robert is an excellent teacher for working with mice and he provided the surgical expertise. His technical understanding and anatomical knowledge have shaped this project. Jonathan has been a reliable and exceptionally competent companion in this project - and most of all a very good friend. I had a lot of fun working with both over these years.

Romano Matthys and Reto Nützi from RISystem AG, Switzerland, had a significant contribution to the development and production of the implant.

I would like to thank Dr. Asylkhan Rakhymzhan for assistance with the microscope optics and his expertise in the field of non-linear optics, which led to many intriguing discussions.

Mario Thiele from the Julius Wolff Institute provided expertise for µCT and helped me with the recordings and data interpretation.

I would like to thank all other current and former colleagues of the Biophysical Analytics Lab and Immunodynamics Lab, who have supported me and whose professional input has always shown me new facets.

Finally, I would like to thank my family and especially my wife Katharina. They kept asking me about the progress of my project, always showing me their great interest in what I do and, thus, providing wonderful support.

Thank you all.

Table of contents

Abbreviations

2PM	two-photon microscopy
3D	three-dimensional
ATPE	asymmetric two-photon excitation
BLI	bioluminescence imaging
c-Kit *or* CKit	receptor tyrosine kinase
CD	cluster of differentiation
(e)CFP	(enhanced) cyan fluorescent protein
(μ)CT	(micro-) computed tomography
CV	curriculum vitae
DAPI	4',6-diamidino-2-phenylindole
EMCM	endomucin
EdU	5-Ethynyl-2´-deoxyuridine
(e/pa-)GFP	(enhanced/photo-activatable) green fluorescent protein
GRIN	gradient index
HEK	human embryonic kidney 293
HSC	hematopoietic stem cell
ISO	international organization for standardization
LASER	light amplification by stimulated emission of radiation
LIMB	longitudinal intravital microscopy in the bone marrow
MHC	major histocompatibility complex
MRI	magnetic resonance imaging
N.A. or NA	numerical aperture
NIR	near IR
PBS	phosphate buffered saline
PET	positron emission tomography
PFA	paraformaldehyde
PMT	photomultiplier tube
(td)RFP	(tandem-dimer) red fluorescent protein
RFID	radio-frequency identification
OPO	optical parametric oscillator
Sca-1	stem cell antigen-1
SHG	second harmonic generation
THG	third harmonic generation
Ti:Sa	titanium:sapphire
TIFF	tagged image file format

Abstract

Bone forming cells of mesenchymal origin and hematopoietic cells of the immune system interact in the bone marrow. Both cell types show high plasticity under homeostatic conditions as well as during bone healing after an injury. Bone marrow is also the central organ for hematopoiesis and harbors the immunological memory. Above all, regeneration and formation of an immunological memory are processes that take place over a period of weeks to months. Since the underlying mechanisms are controlled on the cellular level, *in vivo* multiphoton fluorescence microscopy is the most appropriate and common method to gain insight into the dynamics of these interactions in living tissue under physiological and pathological conditions. However, already established methods for intravital microscopy in the bone marrow of mice are, either designed for imaging a few hours and thus not for repeated, i.e. longitudinal observations, or not designed for long bones, but only for flat bones, i.e. calvarium. In addition, they are physically limited to penetration depths of approx. 100 - 150 µm below the bone cortex.

In the present work, in order to fulfil the needs in understanding bone biology a new microendoscopic technique based on gradient index (GRIN) lenses was developed and applied to analyze cellular dynamics *in vivo*. An internal fixation system ensured the precise positioning of a GRIN endoscope in the femoral bone marrow tissue over months. The optical performance of the endoscope system was comparable to other methods for intravital microscopy in the bone marrow. Via a chronic window, which can be introduced into the bone marrow cavity both centrally and pericortically, we were able for the first time to observe and quantify changes in the vascular structure in one and the same individual over month. The observed plasticity of the blood vessels seems to be unique compared to other tissues. Using histological and flow cytometric methods, we could exclude the possibility that this is a process driven by regeneration processes caused by implantation procedure.

Additionally, to account for the complex dynamic interactions between various cellular and extra-cellular compartments, a method for non-linear asymmetric two-photon excitation (ATPE) and digital unmixing of the recorded fluorescence signals was established, which can be used for the multiplexed recording of eight different tissue components.

The novel endoscope system enables longitudinal intravital microscopy in the murine bone marrow (LIMB) to analyze the osteoimmune system *in vivo* under homeostatic and pathological conditions. With LIMB we expect to gain a deeper insight into the role of the immune system in bone healing, as well as into the establishment and maintenance of immunological memory cells, such as long-lived plasma cells in their special survival niches.

Zusammenfassung

Knochenbildende Zellen mesenchymalen Ursprungs und hämatopoetische Zellen des Immunsystems interagieren im Knochenmark. Sie besitzen sowohl unter homöostatischen Bedingungen als auch während der Knochenheilung nach einer Fraktur eine hohe Plastizität. Das Knochenmark ist das zentrale Organ für die Hämatopoese und unser immunologisches Gedächtnis. Knochenregeneration und die Bildung des immunologischen Gedächtnisses sind Vorgänge, die innerhalb von Wochen oder Monaten ablaufen. Da die zugrundeliegenden Mechanismen auf zellulärer Ebene kontrolliert werden, ist die *in vivo* Multiphotonen-Mikroskopie die geeignetste Methode, um einen Einblick in die dynamischen Interaktionen im lebenden Gewebe unter physiologischen und pathologischen Bedingungen zu gewinnen. Die bereits etablierten Methoden zur Intravitalmikroskopie im Knochenmark von Mäusen sind jedoch zum einen entweder auf Aufnahmen über wenige Stunden und nicht für wiederholte, d.h. longitudinale Beobachtungen ausgelegt, sowie physikalisch auf Eindringtiefen von ca. 100 - 150 µm beschränkt, oder lassen sich nicht auf Röhrenknochen anwenden.

Um den Anforderungen der Analyse der Knochenbiologie entgegenzutreten, wurde eine neue mikro-endoskopische Technik, die auf Gradienten-Index-Linsen (GRIN-Linsen) basiert, entwickelt und getestet. Dabei wurde ein interner Fixateur verwendet, welcher über Monate die präzise Positionierung eines GRIN-Endoskops im Knochenmarksgewebe des Femurs von Mäusen gewährleistet. Die optische Leistungsfähigkeit des Endoskops war mit anderen Methoden zur Intravitalmikroskopie im Knochenmark vergleichbar. Mit Hilfe des Endoskops, welches sowohl zentral als auch perikortikal ins Knochenmark eingebracht werden kann, waren wir erstmals in der Lage Veränderungen in der Gefäßstruktur in ein und demselben Individuum über Monate zu verfolgen und zu quantifizieren. Es zeigte sich eine hohe Plastizität der Blutgefäße, welche im Vergleich zu anderen Geweben einzigartig zu sein scheint. Wir konnten dabei mittels histologischer und durchflusszytometrischer Methoden ausschließen, dass es sich um einen durch Regenerationsprozesse getriebenen Vorgang handelt, der als Reaktion auf die Implantation des Systems ausgelöst wurde.

Um die komplexen, dynamischen Wechselwirkungen zwischen verschiedenen zellulären und extrazellulären Kompartimenten in der intravitalen Bildgebung zu berücksichtigen, wurde des Weiteren ein Verfahren zur nichtlinearen asymmetrischen Zwei-Photonen-Anregung (ATPE) und der digitalen Entfaltung der aufgenommenen Fluoreszenzsignale

etabliert, welches zur parallelen Aufnahme von acht verschiedenen Gewebekompartimenten genutzt werden kann.

Damit ermöglicht das neuartige Endoskopsystem die longitudinale Intravitalmikroskopie im murinen Knochenmark (LIMB) zur Analyse des Osteo-Immunsystems *in vivo* unter homöostatischen und pathologischen Bedingungen. Mit LIMB erhoffen wir uns einen tieferen Einblick in die Rolle des Immunsystems im Verlauf der Knochenheilung, sowie in die Etablierung und des Erhalts immunologischer Gedächtniszellen, wie z.B. langlebiger Plasmazellen in den speziellen Überlebensnischen, zu gewinnen.

1. Introduction

1.1. Biology of bone and marrow – a complex system at the interplay of mesenchymal and hematopoietic cells

The bone marrow under physiological and pathological conditions

In all vertebrates, bone marrow is the main organ for hematopoiesis, which is the continuous generation of red and white blood cells. Whereby white blood cells, called leukocytes, build up the immune system of higher vertebrates and red blood cells, called erythrocytes, take up oxygen in the lungs and provide it to all tissues via the blood flow. Since all blood cells have only a certain lifespan, they have to be constantly reproduced. New leukocytes and erythrocytes that differentiate and mature from hematopoietic stem cells (HSCs) continuously migrate from the bone marrow into the bloodstream (1).

B cells, for instance, complete their maturation in the marrow tissue depending on signaling factors provided by the microenvironment and are only able to leave, when they do not show autoreactivity (2). The bone marrow is, therefore, also a primary lymphoid organ. From the bone marrow, B cells migrate into the blood vessel system and reach the peripheral lymphatic organs, where they further mature to naïve B cells. In these secondary lymphoid organs B cells get initially activated upon antigen-binding by the B cell receptor (BCR). In the following germinal center reaction somatic hypermutation randomly introduces point mutations in the variable regions of the BCR and thus changes the antigen-affinity. BCRs exist membrane-bound and in a secreted form and can, thus, directly recognize antigens bound to surfaces or pathogens. During the affinity maturation, B cells with high-affinity BCRs are positively selected and subsequently differentiate into either plasma blasts, and later plasma cells, or memory B cells and emerge the germinal center (3). Plasma blasts are able to migrate and are only responsive to the chemokine CXCL12 by its receptor CXCR4 (4). When they follow the blood stream into the bone marrow vasculature, they can enter the tissue, where specialized reticular stromal cells secrete high amounts of CXCL12 and other shorter-lived cells provide a stable cytokine environment that keeps the cells alive (5, 6). This specific zone in the bone marrow tissue is, consequently, named survival niche.

In mice, plasma cells were identified that persist in the bone marrow for month and are therefore defined as long-lived (7, 8). Since long-lived plasma cells are non-proliferative and have lost their responsiveness to antigens, they are also called memory plasma cells

(7–11). Memory plasma cells provide early protection against reappearing infections by providing stable antibody titers (5).

T cells in contrast to B cells mature in the thymus and various subsets of T cells are described. Two major groups are the T helper cells and cytotoxic T cells, which can be distinguished by the surface-expression of either CD4 or CD8, respectively. Analogous to B cells, T cells express the T cell receptor (TCRs), albeit it does not exist in a secreted form. TCRs, instead, only recognize peptides, which got processed by other cells and then presented on their surfaces by major histocompatibility complex (MHC) molecules. CD4 and CD8, which are both co-receptors, facilitate binding together with the primary TCR to either class I MHC (only CD8) or class II MHC molecules (only CD4) that are presented on other antigen-presenting cells. CD4+ T cells are called helper cells, because they support the activity of other immune cells, for instance B cells, by secreting cytokines upon activation. Whereas, CD8+ T cells upon activation directly kill the antigen-presenting cell to which they bind. Since class I MHC molecules are presented on every nucleated cell, cytotoxic T cells can fight tumor cells, virus-infected cells as well as damaged cells.

In the course of an infection, naïve T cells also form a small memory population. These are by definition long-lived and begin to divide after re-exposure to its previously encountered pathogen. Unlike memory B and plasma cells, memory T cells can be either tissue resident, e.g. to the gut, lung and lymph nodes, or stay in the peripheral circulation. Similar memory subsets seem to exist for cytotoxic and helper T cells, whereas they can be separated from its naïve state by an increased expression of CD44 (12). Specific bone marrow niches for memory T cells have also been described. For instance, murine CD4+ T cells migrate into the bone marrow mediated by CD49b and CD69 and survive in a resting state and in the absence of antigens in direct vicinity to IL-7 producing reticular stromal cells (13, 14). Memory CD8+ T cells are maintained in the bone marrow by homeostatic proliferation, which is dependent on IL-7 and IL-15 (15–17).

Hence, the bone marrow is an important harbor for the immunological memory, but, beside its immunological functions, the marrow tissue also has a direct influence on the regeneration capacity of the bone after fracture, as stated below. Since the immune system and, thus, the bone marrow tissue is highly dynamic and affected by local stimuli of the surrounding tissues as well as by systemic reactions, physiological and pathological processes can only be investigated under *in vivo* conditions. Meaning, the migration of

cells into or out of the bone marrow must be investigated and interpreted in interaction with the entire organism, because differentiation and migratory behavior of bone marrow cells depend on, both, intramedullary and extramedullary factors. In addition, these stimuli occur on different time scales. They may peak only for a short period but can also persist for days and weeks, such as in fracture healing or formation of the aforementioned immunological memory.

Vascular system in long bones

The bone marrow is connected to the blood system by nutrient arteries and veins that penetrate the cortical bone through canals called nutrient foramina. The foramina and, thus, the bone marrow are only traversed by blood and not by lymphatic vessels, as shown by staining for specific lymphatic endothelial markers LYVE-1 and podoplanin [18]. Hence, for cells the blood circulation is the only route in and out. Inside the medullary cavity the vessel network is formed by arteries, distal arterioles and sinusoids, which, in addition to providing nutrients and oxygen, must also facilitate the migration of cells [1, 19]. The most prominent vessel structure is the central sinus. The nutrient arteries run in parallel to the central sinus and from there branch into the radial arteries and smaller arterioles towards the endosteum. There, close to the cortical bone, they form a dense network of capillaries and venous sinusoids. The permeability of the sinusoids is increased by fewer tight junctions and inter-cellular clefts. The collection veins lead back to the central sinus [20].

The blood vessel network plays a central role in the development and regulation of hematopoiesis, since HSC niches are arranged in the intersinusoidal areas [21]. Intravital multiphoton microscopy has contributed to enormous progress in the understanding of the mobilization of HSCs in the bone marrow, hematopoiesis itself and the static and dynamic processes of the immunological memory [15, 19, 22, 23]. Furthermore, the endothelial cells of the vascular structure are currently getting more and more in the focus of bone formation and fracture healing studies. Not only the (re-)establishment of nutrient supply in the bone marrow by the vessels, but also the direct interaction of endothelial cells with the osteoblasts that form bone appears to be interlinked.

Recently, it has been shown that angiogenesis and osteogenesis in the bone marrow are directly linked via endothelial cells characterized by a high expression of the cell adhesion molecule CD31 and the sialoglycoprotein endomucin (Emcn) (CD31^{hi} Emcn^{hi}). These

cells belong to type H endothelium (24). During the osteogenesis of young mice, type H endothelium was identified exclusively near the growth plates and in the immediate vicinity of the endosteum. Type H endothelium connects the oxygen-rich arterioles with the sinusoids. Proangiogenic signal proteins such as VEGFA, which is secreted by osteoblasts, or PDGFR-β, which is expressed by mesenchymal cells, in combination with the increased transcription of *Pdgfa* and *Pdgfb* compared to other endothelial cells, seem to be a direct cause of co-localization (24, 25). Thus, type H endothelial cells directly depend on bone growth and regeneration. Finally, the presence of CD31^{hi} Emcn^{hi} endothelium can be used as an indicator for active vascular remodeling of the surrounding bone marrow tissue in all age groups.

Bones are the main components of the skeleton

All vertebrates have a supporting skeleton consisting of cartilage and bone, whereby the bone is in principle a particularly hard form of connective tissue. The cortex of the bone is a fiber-reinforced composite material whose morphology is closely related to its mechanical properties (26). Muscles and tendons are attached to the bones. As a structural unit, the skeleton enables locomotion and protects the internal organs.

In addition, bone matrix is an important storage for calcium and phosphate. In order to guarantee the function of the skeleton in the body, the bones must be extremely rigid and, yet, dynamic to allow the adaption to mechanical stress and renew itself effectively in the event of failure (27). Under normal conditions, each year approximately 10 % of the bone matrix is replaced by new tissue (28). This prevents the accumulation of old bone material by continuous mineralization of new connective tissue and the resorption of mineralized bone (29).

Bones can be subdivided by their morphology into long bones (*Ossa longa*), flat bones (*Ossa plana*), compact bones (*Ossa brevia*), pneumatized, i.e. hollow bones (*Ossa pneumatica*) and sesamoid bones (*Ossa sesamoidea*). Long bones can be further divided into three different compartments. The diaphysis (main shaft) and the (proximal and distal) epiphysis are connected by the metaphysis, which contains the growth plate. According to the structure of bone matrix, compact bone (*substantia compacta*; or cortical bone), which forms the cortical area, and spongy bone (*substantia spongiosa*; also spongy or cancellous bone), which is contained in the compact bone, can be distinguished.

Biological function of bone forming cells

Osteoblast and osteoclasts, the so-called bone forming cells, are the main cellular actors in the (re)building process of bone. Osteoclasts are responsible for resorption of the mineralized bone fragments, while osteoblasts synthesize the new bone matrix. The coordinated interaction between osteoclasts and osteoblasts enables a strongly regulated structural remodeling of the intact bone and, also, of the callus during the remodeling phase after fracture, as stated below. Mature osteoblasts synthesize and secrete the bone matrix-forming proteins type I collagen, osteocalcin, osteonectin, glycosaminoglycans, biglycan (proteoglycan-I) and decorin. Collagen type I is the most important structural protein for bone formation. Osteocalcin and osteonectin are then introduced into the collagen-matrix and form the non-mineralized osteoid. Finally, hydroxyapatite, a calcium-containing phosphate mineral, is added to the soft osteoid for hardening (30). The high expression of alkaline phosphatase is decisive for the mineralization process, which is spatially and temporally separated from the matrix formation. The amount of bone volume to be created is determined by the amount of osteoid formed. The stiffness and density of the bone, on the other hand, are defined by the degree of mineralization. During bone formation, the osteoblasts partially close in and then terminally differentiate into osteocytes, which can therefore only be found within the bone matrix. Osteocytes are the most frequent cell type in the bone and form a regular network through small channels (canaliculi) passing through the bone cortex (31). This network is supposed to serve as a communication channel and for nutrient exchange. Osteocytes are regarded as mechanosensory cells that report a need for bone remodeling to osteoblasts and osteoclasts (32).

Osteoclasts are terminally differentiated CD11b+ monocytes and are therefore closely related to macrophages (33). They result from fusion of preosteoclasts. In the bright-field microscope, osteoclasts can be optically identified by their size of 50 to 100 µm, the numerous cell nuclei, the high accumulation of mitochondria, free ribosomes and phosphatase-filled lysosomes (33). For resorption of bone material, they form a sealed area on the surface, which is acidified by proton ATPases to dissolve the mineral components. The protein matrix is subsequently degraded by secreted metalloproteinases and cathepsins (34). Importantly, osteoblast and osteoclast activity can be observed, both, during bone formation and homeostasis, but is in the later balanced to no net production of bone matrix. Nevertheless, the dynamic interaction of these cells is not fully

understood. Especially the lack of technical possibilities for the direct observation of cellular interactions in the native bone marrow of long bones makes a detailed analysis difficult.

Fracture healing

Regeneration of tissues in general is achieved by reorganization, proliferation and differentiation, and requires a high plasticity of the accountable cells (35). Fractures of the bone, which are typically caused by mechanical overload, usually heal completely without leaving a scar. This scarless healing is a unique feature of bone, which, in human, it only shares with the liver. The underlying cellular and mechanobiological processes that influence bone regeneration were nicely reviewed in more detail by Schmidt-Bleek et al. (36). In the following, a brief summary of the common healing cascade is presented.

Depending on the realignment of the bone fragments, two different mechanisms for bone regeneration are described: primary and secondary bone healing. Primary bone healing is achieved when the bone fragments are fixed in a stable position and pressed against each other and, thus, relative movements at the fracture site are prevented. Then, osteoclasts and osteoblast, which are organized in the so-called basic multicellular unit and bridge the bone fragments, directly restore the cortical bone structure (37). If, however, a gap remains, or the bone fragments move relative to each other, secondary bone healing is initiated instead. Under normal conditions, both, primary and secondary bone healing of a fractured bone are very efficient and highly orchestrated processes. Secondary bone healing, however, is a multistage process, meaning the healing process in the bone is characterized by the precise regulation of the initial inflammatory phase and the subsequent structural restoration of the bone matrix (38, 39).

The starting point for secondary fracture healing is the hematoma. With hematoma formation, various cells of the immune system, particularly macrophages, invade the bone marrow at the injury site. The fracture has an effect also on the tissue beyond the fracture site, since the homeostasis within the medullary canal gets disturbed and must adjust itself anew. The early hematoma causes pro-inflammatory signaling, which in turn induces callus formation (38). Nevertheless, subsequent elimination of the inflammation phase is a prerequisite for successful regeneration. Downregulation of the inflammation by anti-inflammatory factors and induction of proangiogenic signaling leads to the formation of granulation tissue by fibroblasts and chondroblasts, that secrete extracellular matrix into

the fracture gap. At the same time, remote from the fracture zone, intramembranous ossification is initiated along with the granulation phase. Here, periosteal osteoprogenitor cells differentiate into osteoblasts, that directly form new woven bone (40, 41). The woven bone grows towards the fracture gap. In parallel, the granulation tissue that fills the fracture gap becomes highly organized cartilage and forms a soft callus. Subsequently, with the onset of osteogenic signaling, the cartilage in the soft callus is calcified and transformed into woven bone - a process called endochondral ossification (42). Hence, primary bone healing is achieved exclusively via intramembranous ossification, whereas during secondary bone healing both mechanisms come into account - although endochondral ossification plays the key role and is responsible for callus formation. To study the progression of these processes, i*n vivo* magnetic resonance imaging (MRI) and micro-computed tomography (µCT) imaging are used to monitor intramembranous bone healing in mice for instance with drill-hole injuries in flat and long bones (43, 44). For endochondral ossification, however, basically, only long bones are used for fracture models, since the fractured bone needs to be stabilized.

During secondary fracture healing vessels need to re-exploit the newly-formed tissue. The onset of osteogenic signaling is accompanied by a peak in proangiogenic signaling and, thus, vessel-sprouting. The callus now has a much larger diameter than the original bone (38, 39). The woven bone in the fracture region together with the woven bone under the periosteum form the so-called hard callus. Already the soft callus provides mechanical stability against torsion and bending and thus minimizes relative movement between the fragments, but only during the final remodeling phase of the hard callus the lamellar structure and outer diameter of the bone is slowly restored and adapted to the mechanical strains (45, 46). In human, this process may take a few months or up to years until also the medullary canal and the original morphology of the bone is restored.

As stated above, the primary inflammatory process, as well as its control and subsequent decay were identified as substantial for the outcome of the bone healing processes (47). Therefore, it is presumed that an adverse alteration in either the pro- or anti-inflammatory signaling impairs the endogenous regeneration capacity by prolonging the inflammation phase or delaying the vascularization, respectively (47, 48). Whereas the release of cytokines by different types of immune cells prevents an uncontrolled inflammatory reaction it also leads to maturation of osteoblasts (38, 49). Especially cell types of the adaptive immune system seem to play a decisive role in the course of bone healing,

whereby it is not possible to generalize if a certain subset is beneficial or detrimental to bone remodeling. For instance, IL-17 secretion by Type 17 T-helper (Th17) cells in bone healing promotes osteoblast maturation and thus fracture repair, whereas it was found in an osteoporosis model to stimulate osteoclastogenesis (49, 50). At the same time, based on observations made in humans, terminally differentiated CD8+ effector memory T (TEMRA) cells seem to have a negative influence on the success of bone healing. These clinical data were reproduced in the mouse model and indicate that TEMRA cells interfere with the regular differentiation of osteoblasts from mesenchymal stroma precursors (51, 52).

It is estimated that 10-20 % of fractures lead to complications that either prolong the healing phase or even end up in a non-union of the bone fragments (53). This problem appears to be pronounced in aged individuals and becomes more relevant for the society due to the demographic changes in the population. With increasing age, the quality of bone tissue decreases dramatically due to diseases such as osteoporosis, especially in women because of the drop of estrogenic level in the menopause. Furthermore, the abilities of the immune system alter with age. This so-called immunosenescence is suspected to favor the reduced regeneration capacity of bones in elderly people.

To investigate adverse effects on bone regeneration, special attention is paid to the migration potential and the presence of inflammatory cells at the fracture site. In addition, the vascular system and the vessel-forming endothelial cells are getting more and more in the focus as they are not only necessary for the nutritional and oxygen supply of the tissue, but also have a direct influence on cellular migration into the fractured zone.

1.2. Mechanics of bone fixation to promote healing

Beside targeting the inflammation cascade, matrix formation, or revascularization, fracture stabilization is an important and probably the first method invented to facilitate bone regeneration. Implants for osteosynthesis are divided in internal and external fixators. External fixators have the advantage, that a fracture can be sufficiently fixed without major additional iatrogenic damage to the soft tissue. Plus, they can be repeatedly accessed for secondary corrections. However, they come with a higher risk of infection over the transcutaneous pins and cannot remain permanently in the patient. Internal fixators, in contrast, do not have to be removed unless complications with the surrounding

tissue occur. Internal fixation systems can be Kirschner wires, intramedullary nails, or plates in combination with screws.

Due to its above mentioned mechanical properties, the skeleton itself is the only organ that supports direct anchoring of implants for a stable fixation in or at the body, although external fixators can also be applied to stabilize soft tissue. In orthopedics and maxillofacial surgery, metallic plates have been used for decades and, more recently, ceramic or polymer-based plates were introduced. Initially, plate osteosynthesis was primarily concerned with aligning the bone fragments as rigidly as possible, so that the inserted plate temporarily undertakes the function of the callus during bridging. The observation that the use of such rigid plate fixators in combination with a lying position of the patient led to a delayed bone healing, brought the field of mechanotransduction into the research focus of bone regeneration. Today, it is known that relative movement between the fragments, and, thus, a certain degree of instability during fixation provides mechanical stimuli required to promote callus formation, although different rates and magnitudes of loading can either favor or prolong ossification (54–56). For instance, at the beginning of the healing phase, a stable fixation promotes cartilage formation and thereby early bridging, whereas at later stages a certain interfragmentary movement is needed to provide physical stimuli for bone formation. The influence of implants on the tissue at the contact zones was also investigated. The bone at the interface to the implant is particularly susceptible to degeneration. The origin is seen in the degeneration of bones due to the reduced supply of nutrients between cortical bone and plate and in the reduction of stress on the bone and the associated transformation of the bones as described by Wolff's law(57, 58). In order to counteract this, synthesis plates have been developed, which, due to their geometry, have only a small contact surface to the bone and thus allow nutrients-supply after implantation - so-called low contact plates for internal fixation (59). These low contact plates are also available for osteotomies in mice (60). Bone degeneration also often occurs at the interfaces to the screws due to micro-vibrations. Radial preloading, however, effectively reduces bone resorption at the interfaces and forestalls loosening over longer periods of time (61). The screws for low contact plates have been adapted accordingly. Mostly, bone screws are inserted bicortically, i.e. they are inserted through the entire bone, which prevents both translation and rotation and thus stabilizes the plate. As the screws are self-tapping, when inserted a pre-tensioning between bone and screw is generated, which has been shown to prevent biological

loosening by bone surface resorption (60, 61). In addition, they lock within the plate by means of an additional conical thread at the head. Thus, the internal fixator can be held in an angle stable position with the bone without compression. Concluding, this system allows an elevated internal fixation, where the plate just bridges the screws without contact to the bone, and has, thus, similarities to external fixators, as it does not require shaping to fit the bone morphology (60, 62).

1.3. Physical background of visualization in the bone

Two-Photon-Excitation Laser-Scanning Microscopy

In theory, the nonlinear process of simultaneous molecular excitation with two photons of lesser energy, but which interact with a sum-frequency similar to the excitation frequency of the molecule, was first described by Maria Göppert-Meyer in 1931 (63). However, only with the practical realization of light amplification by stimulated emission of radiation (LASER) in 1960 this process could be experimentally demonstrated, since the two photons have to interact with the fluorophore nearly simultaneously, i.e. within a few femtoseconds (10^{-16} s) (64). Still, it took until 1990 for multi-photon excitation to be applied in microscopy and to enter the bioscientific and biomedical field (65). Since then the technology has become an indispensable tool for imaging in living tissue sections as well as in living animals, because femtosecond laser sources became commercially available and easy to maintain (66). Today, many techniques are described that use two-photon microscopy (2PM) in optically thick tissue sections or for intravital imaging in animals, e.g. in neurosciences and immunology (67, 68). The reason for the success of the technology relies on the fact that in thick biological samples, nonlinear light scattering and the absorption in the tissue is responsible for the major signal decrease. Scattering scales with λ^{-2} in the case of Rayleigh scattering and with λ^{-4} in the case of Mie scattering (69, 70). Thus, the longer excitation wavelengths, typical for 2PM, are less prone to signal loss due to various tissue scattering effects. Moreover, the so-called "biological window" is described for a wavelength range of approx. 650 to 900 nm, i.e. in the near-infrared (NIR) range, in which the main tissue components (especially hemoglobin) have the lowest absorption. Thus, intravital imaging in the brain could be performed as deep as 1 mm in the tissue (71). In addition, because the rate at which two-photon excitation occurs depends quadratically on the light intensity and, thus, its probability drops rapidly apart from the focal spot. As a consequence, no confocal pinhole aperture is required in two-

photon microscopy to suppress background, which permits more effective detection of all emitted photons (72, 73). Moreover, since effective excitation of the chromophores only takes place in the diffraction limited focal plane, out-of-focus photobleaching is minimized (74). The emission spectra of fluorophores do not differ between one- and two-photon excitation, but especially symmetrical molecules show a clear difference between their one- and two-photon absorption spectra (75). Despite two-photon excited fluorescence, second- and third-harmonic generation (SHG, THG) became applicable to biological nonlinear microscopy by the use of tunable, pulsed (N)IR lasers (76). SHG always occurs at half and THG at one third of the laser wavelength applied and can thereby be tuned. SHG and THG is no fluorescence but a special case of sum frequency generation. In the case of SHG only non-centrosymmetric structures such as collagen generate a second harmonic. SHG, thus, can be used to study tissue structure without additional labelling. THG can be observed at interfaces such as lipid membranes.

The use of optical parametric oscillators (OPO) that operate in the range of 1100 to 1600 nm and the development of redder dyes and proteins allows imaging beyond the reach of the Ti:Sa laser (77). Indeed, both light sources can be run in parallel to simultaneously scan the sample with both foci. Although, care must be taken to properly spatially align the focal spots. Otherwise, the signal produced by one laser is shifted with respect to the other. When both pulsed light sources are also temporally aligned, so-called asymmetric two-photon excitation (ATPE) can be used as a virtual third excitation source to excite an even broader range of fluorophores. In ATPE, also two photons, but now one of each source, interact with the molecules. Still, multiplexing, meaning recording signals from many different fluorescent species (simultaneously), is difficult. The laser sources and PMTs are expensive and not as easy to operate as for conventional laser scanning microscopes. However, by using just a single femtosecond laser light source and frequency conversion, two-photon excitation allows the generation of several fluorescence signals in parallel, that can be detected with a PMT array, but require digital post-processing to spectrally resolve each species.

Longitudinal optical imaging

Histological examinations of tissue (sections) usually take place in the fixed state, so that spatial connections only at one timepoint can be analyzed. Consequently, dynamics can hardly be demonstrated, since only snapshots are evaluated. Intravital microscopic

examinations, which allow time resolved observations, do cover the temporal component very well, but they are limited in the number of parameters that can be detected. Combining spectral multiplexing, specific for histological analysis, with time-resolved detection of cell-cell interactions *in vivo*, still has many technical difficulties, i.e. conservation of the native environmental conditions during observation.

The development of permanent windows for the cerebral cortex or spinal cord solved the challenge of longitudinal imaging, but the limitations on the accessibility of the bone marrow space remain (78, 79). Bone marrow tissue in mammals is always surrounded by a more or less thick, optically highly scattering bone matrix and is, therefore, not readily accessible for conventional light-microscopic techniques. In the mouse model, two methods of intravital multi-photon microscopy in bone marrow are particularly common. On the one hand, cells in the small bone marrow cavities of the calvaria can be imaged relatively easily, since they are covered only by a thin layer of cortical bone and only the scalp needs to be opened to gain access (80). If the scalp is carefully closed again each time after imaging or if it is kept open by a metal ring and the top of the calvaria is sealed with a cover glass, longitudinal studies are also possible (81).

For long bones an intravital imaging technique is well established for the tibia. Since in this case, however, the cortical bone is too thick to microscopically image directly in the bone marrow (also for two-photon excitation), some bone material has to be ablated by surgery (22). This makes the method more invasive and it can only be repeated at a later stage using analgesics because of the high burden for the animals (82). For long-term studies in long bones, a chronic window for the femur was recently presented, which resembles the cranial metal ring with cover glass (83). Again, this is a very invasive method and no data on the animals' reaction or artifacts due to the method within the stated 60-days observation period are presented in this study.

All current methods have in common, whether terminal or longitudinal, that one or more invasive procedures are necessary and either do not provide enough time for regeneration of the tissue, or large tissue areas have to be kept open artificially. In both cases, it is therefore unclear to what extend the observed tissue areas resemble the native biological system. In addition, although two-photon excitation is applied, they only reach areas of the bone marrow near the endosteum. However, it is known that many processes in the bone marrow are long-term processes that can last for weeks. In addition, the marrow of long bone has both radial and axial inhomogeneity in the distribution of cell subsets and

vessels (21). Therefore, we developed a longitudinal method for microendoscopy of the murine bone marrow, which is less invasive, well reproducible in terms of the volume observed, and allows the application of current osteotomy-models for the examination of bone regeneration. We, therefore, oriented ourselves to permanent microendoscopic systems for 2PM, as previously used for imaging the mouse brain (84, 85).

Microendoscopes based on gradient-index optics

Endoscopic systems are usually used in medicine to visualize regions deep within the tissue. Light guiding bundles that are coupled with a camera and a (quite often polychromatic) light source are widely deployed. These are very flexible imaging systems and can be inserted relatively easily into soft tissue. The disadvantages of this method are the strong wavefront distortion of the light and the resulting poor spatial resolution and optical aberrations. Microendoscopes based on gradient index (GRIN) lenses can eliminate these drawbacks, however, they are not flexible. In addition, GRIN lenses can be easily combined with 2PM. Due to their small diameter and stability, these rod-shaped lenses can be implanted for instance into the brain cortex, giving access to deeper layers of the brain for weeks (86, 87).

GRIN systems offer several advantages for endoscopic imaging. Since GRIN lenses are self-focusing lenses without the need for complicated geometries, but only have flat surfaces, they are often used when optical connections between small devices are required, e.g. for fiber coupling or for microendoscopy. The light beam is continuously diffracted in the material, while spherical lenses acquire their lens performance by refracting light twice on the curved surfaces. Focusing in rod-shaped GRIN lens is achieved by a radial refractive index gradient, which is described by a two-dimensional hyperbolic function. The lens performance is, therefore, an intrinsic feature of GRIN lenses. The focal length is almost independent of the refractive index of the surrounding medium and can be achieved by simply varying the length of the lens (88). One way of producing such a gradient profile in a highly-indexed cylindrical glass rod is the ion exchange of silver doping ions with sodium ions, which decrease the refractive index (89). This ion exchange technology in silicate glass requires no toxic substances, so these lenses can be applied in biological and medical research.

Another feature of GRIN lenses, which neither conventional lenses nor fiber optics can offer, is the distortion-free wavefront guidance over a length of up to several centimeters.

The stiffness of GRIN lenses in this case is related to both advantages and disadvantages. On the one hand, deep regions can only be reached without damaging the tissue if they have a straight natural orifice. On the other hand, the mechanical stability enables exact positioning and fixation in tissue. However, since the method described in this work also focuses on a long period of observation and since it is always necessary to have a surgical access for the imaging optics to enter the bone marrow cavity, fixed GRIN endoscopes are a reasonable solution.

1.4. Aims

In this work a new imaging system for multi-photon microscopes is presented that enables longitudinal intravital microscopy in the bone marrow (LIMB) of mice. A microendoscopic method was designed in such a way that examinations can be carried out in the living animals directly, under mild anesthesia repeatedly and exceeding the previously reported timeframes for longitudinal imaging in the bone marrow.

The aims of this work were

- to develop and validate a flexible and minimally invasive, but also highly stable method for long-term observations, so that defined areas close to the endosteum as well as central areas in the bone marrow can be observed over months repeatedly.

- to expand the recorded volume, by improving the endoscope's optic and optimizing it in accordance with the implant design.

- to implement a broader combination of excitation wavelengths and a new unmixing algorithm for post-processing of 4D imaging data, which allows multiplexed time-lapse analysis independent of the biological setting.

1.5. Publications

The results of my work were successfully published in the peer-reviewed journals *Nature Communications* and *Scientific Reports* and are part of this dissertation (section 6). In the following sections the results of both publications are summarized (section 3) and later discussed (section 4). The individual publications are referred to as *Reismann et al.* and *Rakhymzhan et al.*

2. Methods

2.1. Surgical implantation of the LIMB system

For the surgical procedure, the mice were anesthetized with an inhalation anesthesia (1.5 - 2.0 % isoflurane and 97.5 - 98.0 % O2), which was administered via a mask with the aid of an anesthesia device for laboratory rodents (Harvard Apparatus, Cambridge, UK). The depth of anesthesia was regularly monitored during the operation by testing for negative reflex and stimulus perception. To avoid corneal damage, eye ointment containing dexpanthenol (Bayer Vital GmbH, Leverkusen, Germany) was applied to the eyes.

We used a lateral approach to the femoral shaft of the right hind limb. First, a 1.5 cm long incision was made in the shaved and disinfected skin between the right knee and hip joint parallel to the femur. The muscles were then separated along the limiting septum to expose the femoral shaft. A total of three holes must be drilled in the bone cortex. For the 0.65 mm hole, laterally diaphyseal, into which the tube was inserted, we used a dovetail guide and an electric precision drill (both Proxxon GmbH, Wecker, Germany). The implant was then placed parallel to the femoral shaft and fixed with a forceps. The pilot holes (d = 0.31 mm) for the bicortical screws (l = 2 mm) were manually drilled through the holes in the fixator plate with a hand drill (all from RISystem AG, Davos Platz, Switzerland). The screws lock into the fixation plate with a defined torque and prevent movement or rotation of the implant without compressing the bone surface. The wound was washed with sterile NaCl solution and closed with a resorbable suture (Surgicryl Rapid, SMI, St. Vith, Belgium). Finally, the wound was disinfected, and the reference plate attached. LIMB implants were always implanted in the right femur. All surgical instruments used were sterilized appropriately beforehand.

2.2. Intravital microscopy in the bone marrow of mice

For multi-photon microscopy, a laser scanning microscope based on a commercial scanning head (TriMScope II, LaVision BioTec GmbH, Bielefeld, Germany) was used. For the anesthesia, we used an inhalation anesthetic, which was administered via a custom-made mask. The anesthesia was initiated with 2.0 % isoflurane in 98 % oxygen and for imaging reduced to an isoflurane concentration of 1.0-1.5 %. This was sufficient to immobilize the mouse and maintain spontaneous breathing. The anesthetized mouse

was placed on a specially designed table and the implant with the reference plate was mounted to a plastic holder. The plastic holder was fixed in the arm of the table so that the femur and the GRIN lens were fixed in a stable orientation to the objective. The GRIN lens (GRINTech GmbH, Jena, Germany) were aligned parallel to the optical axis of the objective. Additional analgesics were not administered since the entire procedure did not require further surgery and, thus, was painless.

For extended imaging sessions, we used a tempered heat pad to keep the body temperature constant. The entire assembly was positioned on the xy table underneath the 2PM. The 20× air objective (LCPLN20XIR, NA 0.45, Olympus Europa SE & Co. KG, Hamburg, Germany) has a working distance of 8.3 mm and is designed for excitation wavelengths in the NIR range. Before each imaging session, 3-5 µl Qdots 655 (Life Technologies GmbH, Darmstadt, Germany) in 50 µl physiological saline solution were injected via the tail vein to visualize the vascular system.

A titanium-sapphire (Ti:Sa) laser (Coherent, Inc., Dieburg, Germany) was used for excitation in the range of 760nm to 1050 nm and coupled into an optical parametric oscillator (OPO) (APE Angewandte Physik und Elektronik GmbH, Berlin, Germany) for wavelength conversion to 1100nm to 1600 nm. The fluorescence signals were detected with photomultiplier tubes (PMTs) (Hamamatsu Photonics Deutschland GmbH, Herrsching am Ammersee, Germany) in the ranges (466 ± 20) nm, (525 ± 25) nm, (593 ± 20) nm and (655 ± 20) nm.

We recorded 70 µm to 100 µm z-stacks every 30 s (z-stacking step size 6µm) over a total time course of typically 45 min. The same microscope setup was used to visualize the bone marrow in the skull and tibia. In contrast to LIMB, we used a 20× water immersion lens (NA 0.95; Olympus Europa SE & Co. KG, Hamburg, Germany) for this purpose.

2.3. Open-Field behavior

The mice were kept in groups in cages. Only for a certain observation period of 10 to 15 minutes they were placed individually in a cage without hiding places to assess their activity and gait after the operation. Particular attention was paid to ensuring that the animals groom uniformly, that both hind legs are subjected to an even load during running and positioning, and if they gnaw more frequently on the implant.

2.4. Activity measurement

Activity measurements were performed on mice that received either the LIMB implant or a sham treatment (control) and that were subsequently kept in mixed cages. To monitor the activity, all mice were equipped with a subcutaneous RFID chip placed in the abdominal skin in advance so that their movement in the cage could be tracked continuously via sensors below the cage floor (Berlin Mouse Clinic, Berlin, Germany). The average daily activity of each individual in the three days prior to the operation was used to normalize the data.

2.5. Histological analysis of bone marrow sections

Mice were sacrificed by cervical dislocation. The femora were removed and fixed for 4 to 6 hours in 4 % PFA/PBS solution at 4 °C. Femora were then dehydrated in 10 %, 20 % and 30 % sucrose solutions, each for 24 hours, and embedded in SCEM (Section-Lab Co. Ltd., Hiroshima, Japan) and stored at -80 °C. Histological sections with a thickness of 7 µm were made according to the protocol of Kawamoto et al. (90). Movat's pentachrome staining on histological sections was done according to a modified form of the previously published protocol (91). Bright field images were taken on a Biorevo (B-9000, Keyence Deutschland GmbH, Neu-Isenburg, Germany) with a 10× air lens (NA 0.45). For immunofluorescence staining, the sections were blocked with 5 % FCS/PBS for 30 minutes and then incubated with the corresponding primary antibodies for 1-2 hours and secondary antibodies for 1 hour in 5 % FCS/PBS/0.1 % Tween at room temperature. Between the two steps, the sections were washed three times with PBS/0.1 % Tween. Subsequently, the cell nuclei were stained with 1 µg ml^{-1} DAPI (Sigma-Aldrich Chemie GmbH, Taufkichen, Germany) and the sections were embedded with Fluorescent Mounting Medium (Dako Deutschland GmbH, Hamburg, Germany). Images were recorded using a confocal laser scanning microscope (LSM710, Carl Zeiss Microscopy GmbH, Jena, Germany) either with a 10× air lens (NA 0.3) for overview images or a 20× air lens (NA 0.5) for detailed images. Recordings were digitally processed with Zen2011 and Fiji/ImageJ.

2.6. Ex vivo µCT

Femora were removed and fixed as described above. For µCT imaging, the bones were transferred into 20 % to 30 % sucrose solution and measured at room temperature in a

vivaCT 40 (Scanco Medical AG, Brüttisellen, Switzerland) with 70 kVp and an isotropic voxel size of 10.5 µm edge length. The 3D reconstructed images were converted into TIFF stacks for further data analysis. The voxel intensity was determined for bone morphological investigations. Bone thicknesses were approximated fitting a Gauss curve over the intensity distribution, whereby the width of the Gauss curve was considered representative of the bone thickness. The same measurement was performed mirror-inverted on the contralateral bone.

2.7. Determination of reference spectra and unmixing of *in vivo* imaging recordings

The reference spectra were recorded for the fluorescent proteins eCFP, eGFP, mOrange2, mKate2 (Addgene, Cambridge, USA) and eqFP670 (Evrogen, Moscow, Russia) in single-transfected HEK cells. For each individual fluorophore images were recorded with all six channels and, thus, the reference spectrum, including the signature, was recorded. The characteristic ratios between the intensities in the channels were determined by each signature as representative fingerprints. Splenocytes of C57Bl/6 mice were isolated and labelled to determine the representative fingerprints of fluorescent cellular markers (Hoechst, CMTPX Red, Alexa647 (Thermo Fischer Scientific, Berlin, Germany) and Atto680 (Atto-Tec GmbH, Siegen, Germany)).

The SIMI algorithm for unmixing signals works pixel-based. The algorithm determines the best match between an unknown fluorescent signature and that of a known one from the single-color samples by comparing the elements of each channel of the fingerprints, thus, being able to unmix more chromophores than available detection channels. The minimal quadratic deviation between signal and fingerprint is determined by the gradient method. Therefore, the correct assignment of signals requires that each cell is labelled with only one fluorophore. The algorithm was implemented as a plugin for Fiji/ImageJ.

2.8. Mice

All mice were bred on a C57/Bl6J background in the DRFZ breeding facility. All experiments on living mice have been approved by the "Landesamt für Gesundheit und Soziales, Berlin" under license G0070/14, and are in accordance with the institute's internal and state guidelines.

3. Results

Imaging procedures available to date for bone marrow imaging in long bones are only partially suitable for distinguishing between transient and stable tissue states, since they are usually terminal experiments or the recorded time windows are too short. Time-resolved intravital imaging of the bone marrow is an important method for investigating dynamic and static functions of the hematopoietic and immunological system. While for the calvarium of mice, approaches for the imaging of smaller areas of bone marrow have been established for a long time, the imaging in long bones is more complicated, since the cortex is usually covered with muscles and too thick for direct microscopic imaging. Therefore, it is rarely used in longitudinal applications, although significant differences in niche formation for HSCs and bone remodeling are known between both long and flat bones as well as between diaphysis and epiphysis (92).

We have developed a novel approach for longitudinal intravital bone marrow imaging in the femur of mice. A GRIN endoscope was permanently anchored in the bone marrow cavity of the femur by means of an optical access via a titanium implant. First, the design aspects of the implant and its impact on the animals are shown. Then optical and mechanical performance of our method for 2PM are demonstrated. In addition, we compared LIMB with two established intravital methods by following local dynamics of B-cells in the bone marrow with cellular resolution. Moreover, we demonstrated the advantages of the system compared to other methods, by revealing a continuous reorganization of the bone marrow vessels, which was not only observed during bone healing, i.e. due to the injury response after surgery, but also during tissue homeostasis. We were able to rule out the possibility that this was due to an active proliferation of endothelial cells (*Reismann et al.*). Lastly, a novel approach for digital data processing is presented that was introduced to discriminate multiple fluorophores in an underdetermined detection system (*Rakhymzhan et al.*).

In general, LIMB provided results that we expect to have a major influence on the understanding of stem cell niches in bone marrow in particular and in the field of osteoimmunology in more general.

3.1. Design of the implant

Fracture models of long bones are established in, both, the tibia and femur. The microendoscopic implant was developed for permanent optical access to the bone marrow

cavity of the femoral bone, since it is the largest long bone in the skeleton of mice and, thus, also has the largest medullary cavity.

The specifications of the implant, which was designed in cooperation with RISystem AG, Switzerland, are based on the already established principles of low contact plates, which are also used for the internal fixation of fractures in orthopedic surgery (60–62) (*Reismann et al.*, Fig. 1 a-c, Suppl. Fig. 1, Suppl. Movie 1). The principle of low contact plates was already described 25 years ago and aims to avoid devascularization of the soft tissue at the fracture site (93). Together with angle stable screws, the plates can be mounted in an elevated position to avoid surface compression with the periosteum. This principle was successfully applied and further modified to osteosynthesis systems for fracture healing models in mice and other small animals (60, 94). Mice femora have an outer diameter of approx. 1 - 2 mm and an inner diameter of 0.8 - 1.5 mm, depending i.a. on the age and sex of the animals. The oval-shaped medullary cavity in the diaphysis is ~10 mm long. With the lateral approach for the surgery an almost flat area of the femoral shaft was exposed, where the implant could be attached without disrupting any muscles or tendons (*Reismann et al.*, Suppl. Fig. 3).

Due to the radial cutout on the underside of the implant (r = 2 mm), the contact surface to the bone was either very small or no direct contact was detected. This ensured further supply of nutrients and oxygen to the periosteum and, thus, prevented direct necrosis of the periosteum and bone itself (*Reismann et al.*, Fig. 2 a-e). The observed changes in the bone structure over longer periods of 21 days and more can be explained by the active adaptation of the bone matrix to the changing mechanical stress, as the tension is dissipated by the implant during loading of the hind legs (*Reismann et al.*, Fig. 2 f, g).

The microendoscope was based on a self-focusing GRIN lens and is optimized for images taken with a multiphoton microscope, i.e. optimized for transmission in the NIR range (700-1100 nm) (*Reismann et al.*, Fig. 1 d; Suppl. Fig. 2). In order not to occupy too much space in the tissue, a diameter of 350 µm was chosen for the GRIN endoscopes and an outer diameter of 650 µm for a titanium jacket. The overall length of the endoscope tube, which is micro-soldered to the fixator plate, is 3.8 mm. Hence, it bridges the skin and muscle layer above the femur (*Reismann et al.*, Fig. 1 a). The different GRIN endoscopes tested were slightly longer so that they protrude beyond the edge of the titanium tube, thus avoiding reflections. In addition, a titanium rod was micro-soldered parallel to the tube, at which after completing the surgery, the reference plate was attached

extracorporeally. The reference plate was fixed to the rod with a screw and served to position the GRIN endoscope parallel to the objective lens, i.e.to align it along the z-axis (*Reismann et al*., Suppl. Fig 1, 2). It also protected the outer edge from mechanical damage.

We were able to image at different depth within the bone marrow by varying the degree to which the end of the tube protruded into the medullary canal (*Reismann et al*., Fig 1 c). At a length of 500 µm, the endoscope tube ended near the endosteum and with a length of 700 µm it reached the center of the marrow cavity when implanted. To ensure the sterility after surgery, either a sapphire glass was pressed into a recess at the end of the endoscope tube or the GRIN lens was stably glued into the guiding tube to prevent pathogens from entering the medullary space. The system with sapphire window allows using different GRIN endoscopes with different intrinsic magnifications for longitudinal observations in one individual animal. For the systems, with the lens permanently fixed, the optical design of the GRIN endoscope was adapted to the lack of the sapphire glass to maintain the working distance. The main advantage of this system was that the animals could be prepared more quickly for the imaging because cleaning the endoscope tube and insertion of the GRIN lens takes time. In addition, and even more important, the recorded volume between longitudinally taken image-stacks could be reproduced very well and it was, therefore, particularly suitable for long-term studies.

In addition to the standard implant for LIMB in the diaphysis, a shortened version of the implant was designed for metaphyseal application (*Reismann et al*., Suppl. Fig 1 b, right panel). Thus, all areas of the medullary canal could be optically reached. The specifications of the screws were closely matched to those of the internal fixator plate and the biological aspects of fracture regeneration in long bones (60, 61, 93, 95).These were namely the predetermined breaking connection between the shaft and the square drive head, the conical undersurface of the screw head and the self-tapping tip (*Reismann et al*., Suppl. Fig 1 d). The shaft allowed an exact guidance of the screw and the predetermined breaking connection ensured a locking in the fixator plate with an exactly reproducible torque. Below the screw head another conical thread was introduced, which locked with its counterpart in the fixator plate. Thus, both parts formed an angle-stable unit after implantation, independent of compression on the bone surface. Thereby, the implant was fixed in an elevated position by using a defined spacer during the surgery. This ensured that there was no direct contact between the plate and the periosteum and,

as mentioned above for the low contact application, the supply of nutrients to the periosteum was maintained. In addition, it provided another option to vary the penetration depth of the endoscope. The screws, the reference plate and the implant were made of medical grade titanium according to ISO standards, making them fully biocompatible.

3.2. Long-term response – reaching homeostatic conditions after implantation

In order to determine the effects of the surgery and the implantation on mice, we studied parameters such as weight, general appearance, food uptake and natural behavior on a daily basis after surgery. Scores from 0 to a maximum of 3 were assigned for this purpose, whereby a score of 3 describes a very bad condition. The animals achieved a low score on day 3 post-op and within 14 days all parameters were within the normal range again, i.e. have a score of 0 (*Reismann et al.*, Fig 2 h). The correct closure of the wound was also achieved within 14 days after surgery. In addition, animals were observed and filmed in the open-field test on day 2, 6, 9, 13 and 21 after the operation to assess the effects of the operation and the implant on the general behavior and in particular the gait of the animals (*Reismann et al.*, Suppl. Movie 2). Immediately after surgery, the animals were able to load both hind legs evenly. In addition, we did not observe any significant impairment of the gait. Here, the impression that the animals were painless was also confirmed by their activity and curiosity. This impression did not change for trial groups that carried the implant for 60, 90 or even 150 days (data not shown).

To further quantify the effects on the animals' activity, we implanted subcutaneous transponders to record their movements in the cages. The trial group that received the LIMB implant and a control group that only underwent sham surgery were observed before and after the operation. Mice from both groups shared a cage. The normalized, individual daily activities were recorded and a drop in the activity profile was observed directly after the operation (*Reismann et al.*, Fig 2 i). However, from day 3 onward, the values increased and returned to standard values in both groups. Since the control group did not differ significantly from the experimental group, the reduced activity was interpreted as an effect of anesthesia as well as daily monitoring and administration of antibiotics and analgesics. This became particularly evident in the case of a time resolution of 1 hour of the data, in which the circadian rhythm of the animals could be observed (data not shown). Before surgery, the circadian rhythm appeared to be regular,

but got disturbed in the first 3 days after the surgery. Also, the average overall activity decreased. However, from day 4 on, a normal day-night cycle was reestablished.

The endoscope tube and especially the two bicortical screws, which completely penetrated the medullary canal, initially represented a massive intervention in the bone marrow homeostasis. To assess the effects of the LIMB implant on a tissue level regarding postoperative inflammation and bone (re-)formation at the implant site and especially in front of the window, we performed immunofluorescence staining and histochemical analysis on serial histological sections at different time points after surgery. This allowed us to depict the healing process of the bone marrow and the restoration of the vascular structure until completion on day 28 post-op. The most striking changes in the bone marrow of the implant-bearing femora on day 3 post-op were an accumulation of CD45+ cells and increased expression of the extracellular matrix component laminin around the implant (*Reismann et al.*, Fig 3 a, c; Suppl. Fig. 4). Some of the CD45+ cells were also Sca-1+ and, thus, presumably hematopoietic precursor cells. We have also observed elongated, vessel-like CD45- Sca-1+ cell structures surrounded by laminin that grew into the injured area on the site of the endoscope tube and in front of the sapphire glass window. During day 7 to 28 post-op, the inflamed site retracted back, and the tissue structure in the imaging volume of LIMB normalized and appeared comparable to that of the contralateral femur. Cell proliferation, which was depicted by EdU and Ki67 nucleus staining, also showed an equal and comparable distribution between operated and contralateral control bones (*Reismann et al.*, Fig. 7 b; Suppl. Fig 8 b). In summary, the bone marrow of the operated femur on day 28 post-op had a comparable spatial distribution and cell count of hematopoietic, bone-forming and immunological cells as the non-operated bone. Furthermore, the hematopoietic function of both bones was investigated by immunohistological staining of Sca1+ CKit+ cells and flow cytometry of the main hematopoietic cell subsets. Again, we could not find any difference in the frequencies of the different hematopoietic subgroups (*Reismann et al.*, Fig 3 g; Suppl. Fig. 5).

We have also been able to show that likewise the vascular system in the bone marrow adapts and regenerates quickly within this time. Type H endothelium appeared near the implant in the first 2 weeks after surgery. Within 28 days, however, both, morphology and type H endothelial frequency normalized, so that no chronic changes developed in the tissue (*Reismann et al.*, Fig 7 a). Adaptive cell transfer experiments demonstrated that

the bone marrow was uniformly reached and populated by cells and, thus, we concluded that the marrow tissue was continuously supplied by the blood vessels (*Reismann et al.*, Fig 3 e, f).

We further histologically examined the periosteum underneath the implant. On day 7 post surgery, CD31+ Emcn+ vessels appeared below the implant, which were comparable in their distribution to those surrounding the contralateral femur. E*x vivo* μCT images of femora with and without the implant supported this observation. Also, the cortical thickness of the lateral, i.e. where the cortex was covered by the implant, to the medial cortex, as well as from the operated and contralateral femur were compared (*Reismann et al.*, Fig 2 f, g). For these, 21 days after implantation, no significant difference in thickness was observed. However, the adaptation of the bone around the bicortical screws was clearly visible.

With LIMB, we were also able to track the shown regeneration processes *in vivo* longitudinally. In the visible volume directly below the sapphire window, an unstructured vascularization of the granulation layer was observed until day 14 post-op, which was then replaced by normally vascularized tissue until day 21 post-op (*Reismann et al.*, Fig. 1 i).

Taken together, our data show, that in addition to the possibility of investigating bone healing processes with LIMB, the implant is also suitable for longitudinal investigations of cell dynamics under native, homeostatic conditions.

3.3. LIMB reveals permanent vascular dynamics in bone marrow tissue

With the newly developed implant, we were able to record microscopic 3D time-lapse movies of the bone marrow as early as 3 days after surgery (data not shown). For long-term observations, we used 7-day imaging intervals. Short-term effects were observed in smaller intervals of 8 to 12 hours between two sessions. Usually time lapse movies were recorded for about 45 minutes, but series of more than 3 hours were also possible without negative effects on the animals' welfare (*Reismann et al.*, Suppl. Movie 10, 11). Longitudinal images of the blood vessels were possible in individual animals up to 115 days after the operation, even if the animals could in principle carry the implant longer (*Reismann et al.*, Suppl. Movie 12).

To show that LIMB is suitable for imaging natural bone marrow tissue, we directly compared data from LIMB with those acquired with established techniques for intravital microscopy in the tibia and cranial bone (*Reismann et al.*, Fig 4 b-e). The migration of B lymphocytes in the bone marrow of flat and long bones was analyzed in time-lapse movies by digitally reconstructing and tracking the cells' 3D surface (*Reismann et al.*, Suppl. Movie 3-5, 8, 9). The digital tracks of individual B lymphocytes in CD19:tdRFP mice showed different motility and displacement rates, which correlated with the cellular volume. Large B lymphocytes (> 500 µm³), which were probably plasma cells, showed low motility, whereas many of the smaller B lymphocytes (< 500 µm³) were migratory active. When comparing the respective methods, we could not find any statistically significant differences in motility and displacement rates between the two groups in the bone marrows of cranial bone, tibia or femur. This experiment was repeated for LIMB at various time points more than 28 days after surgery. We, therefore, assume that the LIMB system has no considerable influence on the migration behavior of B lymphocytes at time points later than 28 days after surgery. This goes along with the observations stated above for histological, flow cytometric and behavioral analysis.

To demonstrate the stability, i.e. the reproducibility of the depicted volume with LIMB between different time points, we carried out photo-activation experiments in the bone marrow. Thereby, it was ruled out that different tissue areas were investigated at different longitudinal imaging sessions due to mechanical instability. We implanted the LIMB system into mice that ubiquitously express photoactivatable green fluorescent protein (paGFP). Subsequently (>28 days post-op), paGFP expressing cells were photo-activated in a central volume smaller than the imaging volume and recorded repeatedly over a period of three consecutive days (*Reismann et al.*, Fig 5, Suppl. Fig 6). The decrease in the fluorescence signal over time can be explained by the observed exodus of probably hematopoietic cells from the photo-activated volume (*Reismann et al.*, Fig. 7 c, Suppl. Movie 10, 11). In addition, since the half-life of activated paGFP was reported to be about 30 hours in naïve B cells, meaning that the activated paGFP is degraded and replaced by non-activated ones, repeated photo-activation of cells is possible (96). Accordingly, repeatedly photo-labeled cells could be tracked within the bone marrow over longer periods of time with our technique.

Since a stable fixation of the imaging volume was demonstrated, as a consequence, no further reference points are required for orientation between several recordings in the

same individual. Interestingly, when comparing the vessel system between different time points, high plasticity of the vascular structure in the bone marrow of long bones was observed. In particular, small sinusoids (5-10 µm diameter) showed large displacements and thus do not seem to form a static but rather dynamic network within the surrounding tissue (*Reismann et al.*, Fig 5, 6 Suppl. Movie 13). Regeneration mechanisms as the driving force behind these dynamics were ruled out, since longitudinal imaging was done at time points, when no type H vessels or increased rates of proliferation in the endothelial cells as an indication of angiogenesis demonstrated by EdU pulse-chase experiments in combination with staining for Emcn were detected in front of the window (*Reismann et al.*, Fig. 7 a, b). The changes in the vascular network occurred within the range of hours (*Reismann et al.*, Fig. 6). Thus, we suspect that rather a passive displacement of the vessels and the associated stromal structures was behind these dynamics than active vascular remodeling by the corresponding endothelium. However, the complete elucidation of permanent vascular remodeling requires further extensive analyses as discussed later.

3.4. Spectrally multiplexed imaging analysis in living organisms

A challenge for the generation of meaningful intravital microscopic images within bone and bone marrow by LIMB but also in general in the living organs of mammalians is the limitation in parallel detection and identification of multiple cellular and molecular entities. The use of fluorescent markers, each of which has a specific spectral width in both the excitation and emission spectrum, means that clear identification is already biophysically but, above all, technically limited. To overcome these limitations, we developed a new imaging strategy, which, on the one hand, enables a broad excitation spectrum with only one laser light source and, on the other hand, the identification of eight different emitters with an emission range from blue to NIR with a detector array of six PMTs.

The light source used in our optical setup was a pulsed femtosecond laser (Ti:Sa, $\lambda_{ex,1} = 850$ nm). The beam of the Ti:Sa laser was first divided at a beam splitter. One part was coupled directly into the microscope's scan head and the other part was coupled into an OPO for wavelength conversion ($\lambda_{ex,2} = 1230$ nm). The two laser beams were then recombined in the microscope and spatially superimposed (*Rakhymzhan et al.*, Fig. 1 a, c). This enabled an effective two-color excitation. When the laser pulses were also

synchronized in time by a delay-line, it was possible to achieve ATPE (*Rakhymzhan et al.*, Fig. 1 d, e). The exact temporal synchronization was achieved by continuously varying the path length of the OPO beam. Only if the two light pulses of different wavelengths overlap exactly in time and space it was possible that one photon of the OPO together with one photon of the Ti:Sa laser contribute to the ATPE of a fluorophore as shown for mOrange (*Rakhymzhan et al.*, Suppl. Video 2). The effect of the ATPE can, thus, be regarded as a virtual light source with a wavelength of $\lambda_{ex,3} = 1005$ nm. With this excitation system we demonstrated effective synchronous excitation of five fluorescent proteins expressed in HEK cells (CFP, eGFP, mOrange2, mKate2 and eqFP670) or six chromophores (Hoechst, eGFP, Kusabira Orange, CMTPX Red, Alexa 647 and Atto 680) in mouse splenocytes (*Rakhymzhan et al.*, Fig 2). The filters used for detection in front of the PMTs were selected so that the emission maximum of a chromophore lies within the bandwidth of one optical filter. Nevertheless, the spectral width of the emission of each chromophore led to crosstalk in the different channels. By digital post-processing of the image data, however, we were able to decompose or unmix this overlap. The spectral unmixing represents a transformation of the image from the "detection space" to the "fluorophore space" (*Rakhymzhan et al.*, Fig. 3). The applied algorithm was based on reference spectra measured in single color experiments in cells. These were used as fingerprints for each chromophore (*Rakhymzhan et al.*, Suppl. Fig. 3, 4). The similarity of the measured relative distribution of the signal in the individual channels with the reference spectra was then determined pixel by pixel. A gradient method was used to minimize the squared difference between the signal and the reference. Since the spectral signatures of the fluorophores were used as reference, the algorithm allowed simultaneous identification and assignment of more chromophores than the number of PMTs present in the detection setup. This means that the algorithm can solve unmixing even for undetermined systems (*Rakhymzhan et al.*, Fig. 5). The algorithm, therefore, assumes that only one chromophore per pixel was detected during the measurement and must be assigned, which is usually the case in intravital microscopy and what applies here for the whole cell. Theoretically, the number of distinguishable fluorophores was therefore not directly limited, but the quality of discrimination increases with the number of detectors, i.e. with the more precise spectral resolution of the signal, and, thus, the differences in the reference spectra. For instance, we were able to effectively resolve seven color parameters - five fluorescent markers plus frequency doubling (SHG) by collagen fibers and autofluorescence of macrophages - with four channels under *in vivo*

conditions in the lymph nodes of mice (*Rakhymzhan et al.*, Fig. 5 e-g). The different cellular localizations of the chromophores with similar emission maxima were used as controls for the unmixing accuracy. For instance, the nucleus of naïve B cells was stained with Hoechst prior to cell transfer, whereas the CFP expressed by lymphocytes was membrane-bound. CFP and Hoechst have a high spectral overlap and can therefore only be distinguished in the original unmixed data by their different cellular localization. However, digital comparison with the reference spectra made an automated pixel-based separation possible. In a next step, we applied the algorithm successfully to *in vivo* time lapse recordings. This enabled us to determine the dynamic interactions of all central cellular actors during the germinal center reaction in the underdetermined system (*Rakhymzhan et al.*, 6, 7, Suppl. Video 3-5). Hence, we assume that post-processing of the data with SIMI could be easily applied to different biological systems for evaluation of different complex interactions, such as bone regeneration or the formation and maintenance of cellular niches in the bone marrow.

4. Discussion

Non-invasive longitudinal imaging of bone marrow

Due to its compact structure, the bone ensures that the bone marrow effectively evades holistic intravital examination by optical imaging. Other non-invasive imaging techniques such as magnetic resonance imaging (MRI), computed tomography (CT), positron emission tomography (PET) or whole-body bioluminescence imaging (BLI) that physically enable signals to evade from the bone marrow and to be detected *in vivo*. Nevertheless, up to date, these techniques have limitations in the spatial resolution that currently prohibit direct analysis of cell-cell or cell-matrix interactions (97–100). Although promising reporter systems or methods in animal models for the labelling of cells that are subsequently adaptively transferred have now been developed for these techniques, they are hardly capable of distinguishing between two different reporters (except for BLI) and their spatial resolution is limited to the longitudinal localization of cell accumulations in tissue. LIMB, as a microendoscopic approach, instead, provides cellular resolution and permits multi-color experiments in the medullary cavity by optically bypassing the highly scattering bone matrix. In addition to detection of spectrally separated photons by the PMTs in a microscope setup, usage of scanned laser-light as excitation source enables locally precise optical treatment within the tissue. Besides, fluorescent light carries more information than simply the location of the fluorophore, meaning the origin of the photon. Also, polarization and, more interesting in biological settings, the fluorescent lifetime can be read out as in anisotropy or fluorescent lifetime imaging experiments, respectively. This information cannot be gathered by any of the other aforementioned techniques, but still, they can be used as complementary methods to LIMB since they can cover the femoral bone as a whole.

Complementary analysis of cellular migration under *in vivo* conditions

The use of *in vitro* systems, such as transwell migration assays, has provided detailed insights into the chemotaxis of B cells in their various differentiation stages (101). However, since it is known that B lymphocytes react to a large number of chemotactic stimuli present in the tissue, *in vitro* experiments only reflect the *in vivo* situation to a limited extent (102). As a consequence, our knowledge of cell dynamics and interactions in the bone marrow is locally and temporally limited and the *in vivo* analysis is, therefore, complementary to gain deeper understanding of its spatiotemporal organization under

homeostatic and compromised conditions. As stated above, the immune system also plays a decisive role in the initial phase of bone healing, but the interaction between immune cells and the non-hematopoietic compartment has not yet been investigated *in vivo* (38). Due to its complexity, an additional longitudinal analysis of these processes at the cellular level is mandatory.

Beside the above-mentioned tomographic methods, various techniques for intravital microscopy in the bone marrow have already been presented and discussed in the literature (6, 80–83, 103–105). These include recent methods that allow longitudinal microscopy in long bones. However, they have in common that each requires an invasive surgical intervention shortly before imaging and either repeatedly destroy the bone marrow tissue or are only applicable to the pericortical area (83, 105). None of these optical methods have been able to record the center of the bone marrow cavity *in vivo* over extended periods. The method presented here (*Reismann et al.*) enabled longitudinal imaging of the central marrow cavity by use of a microendoscopic system that was implanted into the right femur of mice. With the help of the implanted GRIN microendoscope, we were able to record tissue areas at different depth repeatedly using multi-photon microscopy. The choice of a microendoscopic method is not only due to the optical properties very suitable for longitudinal imaging in the bone marrow of long bones. The optics could be easily and efficiently combined with the established osteosynthesis system for small animals (60). The modifications made to enable the implantation of the GRIN microendoscope in the marrow cavity did not affect properties of the fixator plate such as rigidity, the round undersurface for low contact or the possibility for an elevated fixation. This way, both, the postoperative phases of tissue regeneration and subsequent homeostasis could be monitored in one and the same individual. Interestingly, since the implantation requires a drill hole injury and, thus, shows similarities to the models used for investigating intramembranous ossification, the observations made in the postoperative phase probably display to some extend processes in the marrow tissue as in primary bone healing.

Animal welfare

Beside the reduction of animal numbers, also other ethical factors for the development of LIMB were considered in the technical and surgical approach. So far, no method for long-term analyses was able to follow processes that last for several weeks or month and at the

same time took also the animal's welfare into account. To reduce the burden for the animals, on the one hand, special attention was paid to minimize iatrogenic tissue damage during surgery. For instance, the lateral exposure of the femoral shaft allowed a separation of the muscles by splitting them along the intermuscular septum. Hence, the soft muscle tissue was kept intact. Also, the implant was applied to the femur with high precision by using a stage guided mechanical drill. On the other hand, repeated imaging experiments were non-invasive and were carried out under mild anesthesia only. Based on the normal activity patterns, the regular circadian rhythm already 3 days post-surgery, and the observed natural behavior of the animals carrying the implant, it was demonstrated that the implant itself does not cause any direct or long-term impairment. Accordingly, LIMB is both minimally invasive and biologically compatible over a longer period of time and, consequently, can help to reduce the number of animals required for statistical analyses in a trial group tremendously.

Homeostatic tissue can be imaged from 28 days post-surgery onwards

In addition, the newly developed implant allowed us to exceed the previous time periods for longitudinal imaging in the bone marrow. In the first place, LIMB was dedicated to providing a stable window into the bone marrow to guarantee good reproducibility of the recorded tissue volume. Longitudinal imaging was performed over a period of up to 115 days and, thus, longer than any previously published method. Long-term repeated imaging can be facilitated by placing the end of the endoscope in the marrow cavity without contact to the endosteum. This forestalls bone growth covering the imaging window, since the endosteum is the origin of intramembranous bone formation. On the other hand, this can be deliberately used to study cellular processes during bone formation *in vivo*.

Although, iatrogenic tissue damage during the surgery was minimized, the implantation of the LIMB system, namely the perforation of the bone for insertion of the two screws and the endoscope, first caused a disruption of tissue homeostasis as in drill hole injury models. Histological methods and flow cytometry were used to analyze the course of tissue regeneration and adaption as well as to determine the time point at which these markers again indicate homeostatic conditions. Our results clearly demonstrate that the tissue reaction to the implantation vanishes after a few days to weeks and that the tissue within the imaging volume regains its native state. For instance, the accumulation of

lymphocytes in front of the optics decreased, the extracellular matrix retracts to a thin layer and type H endothelium, which indicates the formation of new vessels (neoangiogenesis), can only be detected until day 21 post surgery. In addition to the histological data, cell transfer and flow cytometry analyses demonstrated that important hematopoietic processes are not permanently disrupted in the presence of the implant and that the vascular system in the entire bone marrow cavity was functional again after 28 days.

LIMB provides a stable but restricted imaging volume

To generate permanent optical access over extended periods of time, as a compromise the spatially limited imaging volume was accepted. Due to the geometry of the microendoscope the imaging volume has cylindrical shape and a diameter of about 150 µm or 280 µm, depending on the lens system applied. We were able to create 3D images of up to 200 µm in z-direction, which were, to our knowledge, not yet published using multiphoton based imaging penetrating through the cortex. Hence, a volume of up to ~12.3 nl, that represents about 0.1 % of the medullary volume of an adult mouse, could be observed. Therefore, the medullary volume was approximated by an oval cylinder with a length $l = 10$ mm and the two radii $r_1 = 0.5$ mm and $r_2 = 0.7$ mm. The volume of the cylinder is then $V = \pi\, h\, r_1\, r_2 \approx 11$ µl. The LIMB time-lapse movies in CD19:tdRFP mice showed that the observed volume is sufficient to follow and evaluate cell migration in a defined region. Even rare cell populations, such as BLIMP1-GFP+ plasma cells, could still be monitored despite their lower cell numbers (data not shown).

To address the heterogeneity of bone marrow tissue of long bones, we have developed different versions of the implant. With these we can position the GRIN lens both diaphyseal and metaphyseal at different depths in the bone marrow. It is known that the cellular composition of these is different and thus they fulfill different physiological functions.

Structural plasticity of blood vessels

Using LIMB, we were able to observe for the first time a structural plasticity of the vessels in the bone marrow not only during the regeneration phase after implantation, but also in homeostasis. Only direct comparison of different sequential recordings made clear that the vascular network in bone marrow appears to continuously change. For other imaging

methods vessel structures are potential reference points among longitudinal images e.g. in the CNS, retina and lymph nodes (87, 106, 107). According to our observations that is not holding true for the bone marrow. Due to the rigid anchoring of our endoscope in the bone matrix, subsequent corrections of the visible volume are not possible, which makes it difficult to reach various tissue regions in one and the same animal. On the other hand, because of the stable anchoring of the microendoscope by the implant, further reference points in the tissue are not necessary. We observed, in particular, smaller vessels to permanently restructure their shape, which seems quite reasonable considering bone marrow biology. The bone marrow is characterized by its high proportion of proliferating cells (6). In addition, the endothelial cells of the vessels in the bone marrow do not form a closed barrier and, thus, support the rapid and continuous exchange of leukocytes between the tissue and the blood circulation (19, 21). For example, memory cells of the immune system are directed into the bone marrow tissue in their niche via chemotactic signals of the stroma cells (108). The observed rearrangement of the vessels is, therefore, presumably not an active process driven by the proliferation of endothelial cells, but rather a passive displacement by other migrating, proliferating or expanding cells. The performed histological analysis of proliferating cells confirmed this so far. By injecting Qdots it was possible to visualize the blood flow and, thus, determine the effective lumen of the vessels *in vivo*. Still, to better judge whether the vessels are pushed or actively move, individual endothelial cells need to be observed over time. Thus, in order to gain a better understanding of the dynamics of vascularization and the interaction with immune and bone cells, further longitudinal investigations are necessary, which particularly address newly sprouting vessels, e.g. by using endothelial cell reporters such as Tie2:GFP mice (109).

Applicability of multiplexed imagining and data analysis to LIMB

In general, our observations expand our understanding of bone marrow survival niches and the complexity of their possible regulation. However, to establish a connection between the individual compartments, these must be marked and differentiated. We demonstrated with our 2PM setup that such multiplex analysis can be done intravitally in the lymph node. To excite a broad panel of fluorophores, both, OPO and Ti:Sa beam paths were focused independently of each other in the microscope and the delay stage allowed adaptation to the optical properties of the imaging objective and the tissue. With the current setup both laser paths could be adjusted accordingly to the GRIN optics in the

LIMB system to use the effect of ATPE with OPO and Ti:Sa also in the bone marrow. Compared to a sequential excitation of a large spectrum of fluorescent molecules, this has the advantage that the higher acquisition rate at simultaneous excitation makes it possible to investigate cellular dynamics (110). In addition, the optimal adjustment of such a system is easier to implement than with three independent laser beam paths (111). Since the palette of fluorescent proteins ranges from blue to NIR, we have deliberately tested those that cover the entire spectrum (112, 113). Indeed, the spectral separation of the individual fluorophores was essential for the subsequent differentiation of different compartments. By matching the recorded data with the previously determined reference spectra in each recorded channel, differences in the overlays had no influence on the result of the unmixing. Whereas linear unmixing strategies are mostly restricted by the number of detectors, which restricts the number of distinguishable signals, the SIMI algorithm, on the other hand, is not directly limited by this.

As previously discussed, bone regeneration is a complex process, encompassing several phases, during which various immune cell subsets and compartments of the bone and bone marrow dynamically interact and finally lead to organ healing. Thus, to understand the underlying mechanisms of these dynamic interactions it is necessary to simultaneously visualize and investigate them *in vivo*. Therefore, combining the here developed multiplexed intravital imaging with longitudinal imaging of the bone marrow by LIMB will provide us with a unique tool to better understand bone regeneration. The lack of appropriate multi-reporter mice and the difficulties to generate those have be overcome, for instance by transferring labeled cells of interest. Although, in simple cell transfer experiments only a small portion of the cells of interest is labeled. Nevertheless, the versatility of multiplexed LIMB will be of great use for better understanding hematopoiesis, immunological memory or various pathologies related to the bone and bone marrow.

Outlook

LIMB is a unique method that enabled us to use intravital multi-photon microscopy to analyze the same tissue areas in the (deep) bone marrow of individual mice longitudinally. We successfully demonstrated a stable imaging volume deep within the marrow cavity for several months, while the animals, after recovery from the surgery, were not impaired.

Hence, LIMB has the great advantage that it is an additional tool for intravital investigation and does not impede further *ex vivo* analyses.

In addition, a method for digital unmixing of fluorescence signals was evolved, which, in principle, is applicable to every fluorescence-based imaging technique. Since the SIMI algorithm works pixel-wise and is thus depending on the filter- and detector-setup, but not on the light-guiding optics, we assume that also multiplexed LIMB recordings can be successfully unmixed. Analogous to the multiplex time-lapse videos taken during the germinal center reaction and the subsequent unmixing of the signals, a dynamic longitudinal analysis of the interaction between stroma cells, the vessel-forming endothelial cells and inactive memory cells with LIMB seems to be possible for the first time. However, it is still necessary to gain a better general understanding of the dynamics of vascularization and the interaction with immune and bone cells and to investigate the effects of the constantly changing vessels on the niche concepts. Further longitudinal investigations are planned, which particularly address newly sprouting vessels, e.g. by using endothelial cell reporters such as Tie2:GFP or Flk1:GFP mice (109, 114). These will allow us to investigate more closely how vascular endothelial cells are reorganized and whether similar dynamic processes also occur in the bone marrow of flat bones, as indicated by the longitudinal recordings in the calvaria (*Reismann et al.*, Fig. 5 b, Suppl. Fig 7).

Furthermore, it is planned to apply the technique to an osteotomy model for direct longitudinal observation of cell migration during all phases of bone regeneration. Minor modifications to the design of the implant might be necessary, depending on the gap-size used for the osteotomy to ensure a certain stability of the fractured bone. Also, the position of the endoscope tubing will be adapted to visualize different zones within or remote from the fracture-gap. On the one hand LIMB in combination with SIMI will allow us to resolve the migratory behavior of cellular actuators, but also the long-term effects of tissue engineered bone constructs or other biomaterials designed to facilitate the natural healing cascade can thus be studied *in vivo*. With scaffolds placed in a fracture-gap and in the imaging volume of the endoscope, a direct effect of the material on cells could be investigated. These scaffolds, in addition, can be enriched in advance with a potent chemoattractant or seeded with previously sorted fluorescent cells as defined potential actuators, that one could than follow with LIMB *in vivo* (115, 116).

LIMB provides the unique feature that the bone marrow can be studied before, during and after osteotomy. We, therefore, contrived a second, minimally invasive surgery to perform the osteotomy at a later time-point after implantation. Our idea is to guide a Gigli saw with a bend hollow needle around the femoral shaft by just puncturing the skin and the surrounding muscles. For the precise positioning of the gap, the reference plate can be used as a guide. Yet, this has not been tested *in vivo*.

To overcome the current limitation of the recorded volume, larger GRIN microendoscopes will be tested. An increase of the GRIN lens' diameter will automatically increase the imaging volume not only in the xy-plane but also in z, since the efficiency with which the emitted photons are collected and guided through the GRIN lens will increase. Still, the diameter of the medullary cavity limits the diameter of the endoscope. We plan to test GRIN lenses with a diameter of 0.6 mm, which are not surrounded by the tubing at the end. Thus, the part reaching into the marrow cavity has similar dimensions as in the described setup.

Still, longitudinal imaging in the calvarium will provide larger overviews as complementary information gained from flat bones. An interesting and promising version of a "crystal skull" - a cover glass adapted to the curvature of the dorsal cranium - was reported recently (117). Although this method was initially developed for intravital imaging of large volumes in the brain, the system could also be adapted for longitudinal microscopy of bone marrow spots in the calvaria to eliminate disturbing effects at the margin that occur with flat cover glasses.

Taken together, our technology opens up new possibilities to examine and characterize, both, long-term processes with slower dynamics and short-term processes characterized by faster cellular dynamics. LIMB can be used to visualize a wide variety of physiological and pathophysiological processes in the bone marrow, including regenerative processes such as bone regeneration after injury, hematopoiesis, but also in the characterization of tumor formation and bone marrow metastasis. Accordingly, various research areas, such as immunology, osteology and hemato(onco)logy, to name just a few, will benefit from this novel imaging method.

5. References

1. Ramasamy, S. K., A. P. Kusumbe, M. Schiller, D. Zeuschner, M. G. Bixel, C. Milia, J. Gamrekelashvili, A. Limbourg, A. Medvinsky, M. M. Santoro, F. P. Limbourg, and R. H. Adams. 2016. Blood flow controls bone vascular function and osteogenesis. *Nat. Commun.* 7: 13601.

2. Murphy, K. P., P. Travers, M. Walport, and C. Janeway. 2008. *Janeway's Immunobiology*,.

3. Nutt, S. L., and D. M. Tarlinton. 2011. Germinal center B and follicular helper T cells: Siblings, cousins or just good friends? *Nat. Immunol.* 12: 472–477.

4. Hargreaves, D. C., P. L. Hyman, T. T. Lu, V. N. Ngo, A. Bidgol, G. Suzuki, Y. R. Zou, D. R. Littman, and J. G. Cyster. 2001. A coordinated change in chemokine responsiveness guides plasma cell movements. *J. Exp. Med.* 194: 45–56.

5. Tokoyoda, K., A. E. Hauser, T. Nakayama, and A. Radbruch. 2010. Organization of immunological memory by bone marrow stroma. *Nat. Rev. Immunol.* 10: 193–200.

6. Zehentmeier, S., K. Roth, Z. Cseresnyes, O. Sercan, K. Horn, R. A. Niesner, H.-D. Chang, A. Radbruch, A. E. Hauser, Ö. Sercan, K. Horn, R. A. Niesner, H.-D. Chang, A. Radbruch, and A. E. Hauser. 2014. Static and dynamic components synergize to form a stable survival niche for bone marrow plasma cells. *Eur. J. Immunol.* 44: 2306–2317.

7. Slifka, M. K., R. Antia, J. K. Whitmire, and R. Ahmed. 1998. Humoral immunity due to long-lived plasma cells. *Immunity* 8: 363–372.

8. Manz, R. A., A. Thiel, and A. Radbruch. 1997. Lifetime of plasma cells in the bone marrow. *Nature* 388: 133–134.

9. Radbruch, A., G. Muehlinghaus, E. O. Luger, A. Inamine, K. G. C. C. Smith, T. Dörner, and F. Hiepe. 2006. Competence and competition: The challenge of becoming a long-lived plasma cell. *Nat. Rev. Immunol.* 6: 741–50.

10. Manz, R. A., M. Löhning, G. Cassese, A. Thiel, and A. Radbruch. 1998. Survival of long-lived plasma cells is independent of antigen. *Int. Immunol.* 10: 1703–11.

11. Tokoyoda, K., S. Zehentmeier, H.-D. Chang, and A. Radbruch. 2009. Organization and maintenance of immunological memory by stroma niches. *Eur. J. Immunol.* 39: 2095–9.

12. DeGrendele, H. C., P. Estess, and M. H. Siegelman. 1997. Requirement for CD44 in activated T cell extravasation into an inflammatory site. *Science (80-.).* 278: 672–675.

13. Tokoyoda, K., S. Zehentmeier, A. N. Hegazy, I. Albrecht, J. R. Grün, M. Löhning, and A. Radbruch. 2009. Professional memory CD4+ T lymphocytes preferentially reside and rest in the bone marrow. *Immunity* 30: 721–30.

14. Shinoda, K., K. Tokoyoda, A. Hanazawa, K. Hayashizaki, S. Zehentmeier, H. Hosokawa, C. Iwamura, H. Koseki, D. J. Tumes, A. Radbruch, and T. Nakayama. 2012. Type II membrane protein CD69 regulates the formation of resting T-helper memory. *Proc. Natl. Acad. Sci.* 109: 7409–7414.

15. Mazo, I. B., M. Honczarenko, H. Leung, L. L. Cavanagh, R. Bonasio, W. Weninger, K. Engelke, L. Xia, R. P. McEver, P. A. Koni, L. E. Silberstein, and U. H. von Andrian. 2005. Bone marrow is a major reservoir and site of recruitment for central memory CD8+T cells. *Immunity* 22: 259–70.

16. Becker, T. C., S. M. Coley, E. J. Wherry, and R. Ahmed. 2005. Bone Marrow Is a Preferred Site for Homeostatic Proliferation of Memory CD8 T Cells. *J. Immunol.* 174: 1269–1273.

17. Tan, J. T., B. Ernst, W. C. Kieper, E. LeRoy, J. Sprent, and C. D. Surh. 2002. Interleukin (IL)-15 and IL-7 jointly regulate homeostatic proliferation of memory phenotype CD8+ cells but are not required for memory phenotype CD4+ cells. *J. Exp. Med.* 195: 1523–32.

18. Edwards, J. R., K. Williams, L. G. Kindblom, J. M. Meis-Kindblom, P. C. W. W. Hogendoorn, D. Hughes, R. G. Forsyth, D. Jackson, and N. A. Athanasou. 2008. Lymphatics and bone. *Hum. Pathol.* 39: 49–55.

19. Beck, T. C., A. C. Gomes, J. G. Cyster, and J. P. Pereira. 2014. CXCR4 and a cell-extrinsic mechanism control immature B lymphocyte egress from bone marrow. *J. Exp. Med.* 211: 2567–81.

20. Travlos, G. S. 2006. Normal structure, function, and histology of the bone marrow. *Toxicol. Pathol.* 34: 548–65.

21. Itkin, T., S. Gur-Cohen, J. A. Spencer, A. Schajnovitz, S. K. Ramasamy, A. P. Kusumbe, G. Ledergor, Y. Jung, I. Milo, M. G. Poulos, A. Kalinkovich, A. Ludin, O. Kollet, G. Shakhar, J. M. Butler, S. Rafii, R. H. Adams, D. T. Scadden, C. P. Lin, and T. Lapidot. 2016. Distinct bone marrow blood vessels differentially regulate haematopoiesis. *Nature* 532: 323–328.

22. Köhler, A., K. De Filippo, M. Hasenberg, C. Van Den Brandt, E. Nye, M. P. Hosking, T. E. Lane, L. Männ, R. M. Ransohoff, A. E. Hauser, O. Winter, B. Schraven, H. Geiger, N. Hogg, and M. Gunzer. 2011. G-CSF-mediated thrombopoietin release triggers neutrophil motility and mobilization from bone marrow via induction of Cxcr2 ligands. *Blood* 117: 4349–4357.

23. Junt, T., H. Schulze, Z. Chen, S. Massberg, T. Goerge, A. Krueger, D. D. Wagner, T. Graf, J. E. Italiano, R. A. Shivdasani, and U. H. von Andrian. 2007. Dynamic Visualization of Thrombopoiesis Within Bone Marrow. *Science (80-.).* 317: 1767–1770.

24. Kusumbe, A. P., S. K. Ramasamy, and R. H. Adams. 2014. Coupling of angiogenesis and osteogenesis by a specific vessel subtype in bone. *Nature* 507: 323–328.

25. Ramasamy, S. K., A. P. Kusumbe, L. Wang, and R. H. Adams. 2014. Endothelial Notch activity promotes angiogenesis and osteogenesis in bone. *Nature* 507: 376–380.

26. Yeni, Y. N., C. U. Brown, Z. Wang, and T. L. Norman. 1997. The influence of bone morphology on fracture toughness of the human femur and tibia. *Bone* 21: 453–459.

27. Datta, H. K., W. F. Ng, J. A. Walker, S. P. Tuck, and S. S. Varanasi. 2008. The cell biology of bone metabolism. *J. Clin. Pathol.* 61: 577–587.

28. Manolagas, S. C. 2000. Birth and death of bone cells: basic regulatory mechanisms and implications for the pathogenesis and treatment of osteoporosis. *Endocr. Rev.* 21: 115–37.

29. Frost, H. M. 1973. Bone Remodeling and Its Relationship to Metabolic Bone Disease. *Charles C. Thomas, Springfield, MA* .

30. Boskey, A. 1996. Matrix proteins and mineralization: an overview. *Connect. Tissue Res.* .

31. Noble, B. S. 2008. The osteocyte lineage. *Arch. Biochem. Biophys.* 473: 106–11.

32. van Bezooijen, R. L., S. E. Papapoulos, N. A. Hamdy, P. ten Dijke, and C. W. Löwik. 2005. Control of bone formation by osteocytes? Lessons from the rare skeletal disorders sclerosteosis and van Buchem disease. *BoneKEy-Osteovision* 2: 33–38.

33. Roodman, G. D. 1996. Advances in bone biology: the osteoclast. *Endocr. Rev.* 17: 308–332.

34. Bossard, M. J., T. A. Tomaszek, S. K. Thompson, B. Y. Amegadzie, C. R. Hanning, C. Jones, J. T. Kurdyla, D. E. McNulty, F. H. Drake, M. Gowen, and M. A. Levy. 1996. Proteolytic activity of human osteoclast cathepsin K. Expression, purification, activation, and substrate identification. *J. Biol. Chem.* 271: 12517–12524.

35. Agata, K., Y. Saito, and E. Nakajima. 2007. Unifying principles of regeneration I: Epimorphosis versus morphallaxis. *Dev. Growth Differ.* 49: 73–78.

36. Schmidt-Bleek, K., A. Petersen, A. Dienelt, C. Schwarz, and G. N. Duda. 2014. Initiation and early control of tissue regeneration - bone healing as a model system for tissue regeneration. *Expert Opin. Biol. Ther.* 14: 247–59.

37. Gerstenfeld, L. C., D. M. Cullinane, G. L. Barnes, D. T. Graves, and T. A. Einhorn. 2003. Fracture healing as a post-natal developmental process: Molecular, spatial, and temporal aspects of its regulation. *J. Cell. Biochem.* 88: 873–884.

38. Kolar, P., K. Schmidt-Bleek, H. Schell, T. Gaber, D. Toben, G. Schmidmaier, C. Perka, F. Buttgereit, and G. N. Duda. 2010. The early fracture hematoma and its potential role in fracture healing. *Tissue Eng. Part B. Rev.* 16: 427–34.

39. Petersen, A., P. Joly, C. Bergmann, G. Korus, and G. N. Duda. 2012. The impact of substrate stiffness and mechanical loading on fibroblast-induced scaffold remodeling. *Tissue Eng. Part A* 18: 1804–17.

40. Park, D., J. A. Spencer, B. I. Koh, T. Kobayashi, J. Fujisaki, T. L. Clemens, C. P. Lin, H. M. Kronenberg, and D. T. Scadden. 2012. Endogenous bone marrow MSCs are dynamic, fate-restricted participants in bone maintenance and regeneration. *Cell Stem Cell* 10: 259–272.

41. Colnot, C. 2009. Skeletal cell fate decisions within periosteum and bone marrow during bone regeneration. *J. Bone Miner. Res.* 24: 274–82.

42. Liu, Y., I. Manjubala, H. Schell, D. R. Epari, P. Roschger, G. N. Duda, and P. Fratzl. 2010. Size and habit of mineral particles in bone and mineralized callus during bone healing in sheep. *J. Bone Miner. Res.* 25: 2029–2038.

43. Taha, M. A., S. L. Manske, E. Kristensen, J. T. Taiani, R. Krawetz, Y. Wu, D. Ponjevic, J. R. Matyas, S. K. Boyd, D. E. Rancourt, and J. F. Dunn. 2013. Assessment of the efficacy of MRI for detection of changes in bone morphology in a mouse model of bone injury. *J. Magn. Reson. Imaging* 38: 231–237.

44. Ono, T., K. Okamoto, T. Nakashima, T. Nitta, S. Hori, Y. Iwakura, and H. Takayanagi. 2016. IL-17-producing γδ T cells enhance bone regeneration. *Nat. Commun.* 7: 10928.

45. Gerstenfeld, L. C., Y. M. Alkhiary, E. A. Krall, F. H. Nicholls, S. N. Stapleton, J. L. Fitch, M. Bauer, R. Kayal, D. T. Graves, K. J. Jepsen, and T. A. Einhorn. 2006. Three-dimensional Reconstruction of Fracture Callus Morphogenesis. *J. Histochem. Cytochem.* 54: 1215–1228.

46. Frost, H. M. 1983. A determinant of bone architecture. The minimum effective strain. *Clin. Orthop. Relat. Res.* 286–292.

47. Schmidt-Bleek, K., H. Schell, J. Lienau, N. Schulz, P. Hoff, M. Pfaff, G. Schmidt, C. Martin, C. Perka, F. Buttgereit, H. Volk, and G. Duda. 2012. Initial immune reaction and angiogenesis in bone healing. *J Tissue Eng Regen Med* 8: 120–130.

48. Schmidt-Bleek, K., H. Schell, N. Schulz, P. Hoff, C. Perka, F. Buttgereit, H.-D. Volk, J. Lienau, and G. N. Duda. 2012. Inflammatory phase of bone healing initiates the regenerative healing cascade. *Cell Tissue Res.* 347: 567–573.

49. Nam, D., E. Mau, Y. Wang, D. Wright, D. Silkstone, H. Whetstone, C. Whyne, and B. Alman. 2012. T-lymphocytes enable osteoblast maturation via IL-17F during the early phase of fracture repair. *PLoS One* 7: e40044.

50. Yuan, F.-L., X. Li, W.-G. Lu, Y.-Q. Zhao, C.-W. Li, J.-P. Li, J.-M. Sun, and R.-S. Xu. 2012. Type 17 T-helper cells might be a promising therapeutic target for osteoporosis. *Mol. Biol. Rep.* 39: 771–774.

51. Reinke, S., S. Geissler, W. R. Taylor, K. Schmidt-Bleek, K. Juelke, V. Schwachmeyer, M. Dahne, T. Hartwig, L. Akyüz, C. Meisel, N. Unterwalder, N. B. Singh, P. Reinke, N. P. Haas, H.-D. Volk, and G. N. Duda. 2013. Terminally differentiated CD8$^+$ T cells negatively affect bone regeneration in humans. *Sci. Transl. Med.* 5: 177ra36.

52. Triffitt, J. 1996. The stem cell of the osteoblast. *Princ. bone Biol.* 39–50.

53. Hernandez, R. K., T. P. Do, C. W. Critchlow, R. E. Dent, and S. S. Jick. 2012. Patient-related risk factors for fracture-healing complications in the United Kingdom General Practice Research Database. *Acta Orthop.* 83: 653–660.

54. Steck, R., M. Ueno, L. Gregory, N. Rijken, M. E. Wullschleger, M. Itoman, and M. A. Schuetz. 2011. Influence of internal fixator flexibility on murine fracture healing as characterized by mechanical testing and microCT imaging. *J. Orthop. Res.* 29: 1245–50.

55. Epari, D. R., H. Schell, H. J. Bail, and G. N. Duda. 2006. Instability prolongs the chondral phase during bone healing in sheep. *Bone* 38: 864–70.

56. Morgan, E. F., R. E. Gleason, L. N. M. Hayward, P. L. Leong, and K. T. S. Palomares. 2008. Mechanotransduction and fracture repair. *J. Bone Joint Surg. Am.* 90 Suppl 1: 25–30.

57. Klaue, K., I. Fengels, and S. M. Perren. 2000. Long-term effects of plate osteosynthesis: comparison of four different plates. *Injury* 31 Suppl 2: S-B51-62.

58. Turner, C. H., and F. M. Pavalko. 1998. Mechanotransduction and functional response of the skeleton to physical stress: the mechanisms and mechanics of bone adaptation. *J. Orthop. Sci.* 3: 346–55.

59. Perren, S. M. 2002. Evolution of the internal fixation of long bone fractures. The scientific basis of biological internal fixation: choosing a new balance between stability and biology. *J. Bone Joint Surg. Br.* 84: 1093–110.

60. Matthys, R., and S. M. Perren. 2009. Internal fixator for use in the mouse. *Injury* 40 Suppl 4: S103-9.

61. Hyldahl, C., S. Pearson, S. Tepic, and S. M. Perren. 1991. Induction and prevention of pin loosening in external fixation: an in vivo study on sheep tibiae. *J. Orthop. Trauma* 5: 485–92.

62. Perren, S. M. 2002. Evolution of the internal fixation of long bone fractures. *J. Bone Jt. Surg.* 84: 1093–1110.

63. Göppert-Mayer, M. 1931. Über Elementarakte mit zwei Quantensprüngen. *Ann. Phys.* 401: 273–294.

64. Maiman, T. H. 1960. Stimulated Optical Radiation in Ruby. *Nature* 187: 493–494.

65. Denk, W., J. H. Strickler, and W. W. Webb. 1990. Two-photon laser scanning fluorescence microscopy. *Science (80-.).* 248: 73–76.

66. Zipfel, W. R., R. M. Williams, and W. W. Webb. 2003. Nonlinear magic: multiphoton microscopy in the biosciences. *Nat. Biotechnol.* 21: 1369–1377.

67. Niesner, R., V. Siffrin, and F. Zipp. 2013. Two-photon imaging of immune cells in neural tissue. *Cold Spring Harb. Protoc.* 2013.

68. Herz, J., M. Paterka, R. A. Niesner, A. U. Brandt, V. Siffrin, T. Leuenberger, J. Birkenstock, A. Mossakowski, R. Glumm, F. Zipp, and H. Radbruch. 2011. In vivo imaging of lymphocytes in the CNS reveals different behaviour of naïve T cells in health and autoimmunity. *J. Neuroinflammation* 8: 131.

69. Herz, J., V. Siffrin, A. E. Hauser, A. U. Brandt, T. Leuenberger, H. Radbruch, F. Zipp, and R. A. Niesner. 2010. Expanding two-photon intravital microscopy to the infrared by means of optical parametric oscillator. *Biophys. J.* 98: 715–23.

70. Niesner, R., V. Andresen, J. Neumann, H. Spiecker, and M. Gunzer. 2007. The power of single and multibeam two-photon microscopy for high-resolution and high-speed deep tissue and intravital imaging. *Biophys. J.* 93: 2519–29.

71. Theer, P., M. T. Hasan, and W. Denk. 2003. Two-photon imaging to a depth of 1000 µm in living brains by use of a Ti:Al2O3 regenerative amplifier. *Opt. Lett.* 28: 1022.

72. Denk, W., and K. Svoboda. 1997. Photon upmanship: why multiphoton imaging is more than a gimmick. *Neuron* 18: 351–7.

73. Sheppard, C. J. R., and M. Gu. 1990. Image formation in two-photon fluorescence microscopy. *Optik (Stuttg).* 86: 104–106.

74. Jung, J. C., and M. J. Schnitzer. 2003. Multiphoton endoscopy. *Opt. Lett.* 28: 902–4.

75. Xu, C., and W. W. Webb. 1996. Measurement of two-photon excitation cross sections of molecular fluorophores with data from 690 to 1050 nm. *J. Opt. Soc. Am. B* 13: 481.

76. Freund, I., and M. Deutsch. 1986. Second-harmonic microscopy of biological tissue. *Opt. Lett.* 11: 94.

77. Baloban, M., D. M. Shcherbakova, S. Pletnev, V. Z. Pletnev, J. C. Lagarias, and V. V Verkhusha. 2017. Designing brighter near-infrared fluorescent proteins: insights from structural and biochemical studies. *Chem. Sci.* 8: 4546–4557.

78. Trachtenberg, J. T., B. E. Chen, G. W. Knott, G. Feng, J. R. Sanes, E. Welker, and K. Svoboda. 2002. Long-term in vivo imaging of experience-dependent synaptic plasticity in adult cortex. *Nature* 420: 788–794.

79. Farrar, M. J., F. W. Wise, J. R. Fetcho, and C. B. Schaffer. 2011. In vivo imaging of myelin in the vertebrate central nervous system using third harmonic generation microscopy. *Biophys. J.* 100: 1362–1371.

80. Mazo, I. B., and U. H. von Andrian. 1999. Adhesion and homing of blood-borne cells in bone marrow microvessels. *J. Leukoc. Biol.* 66: 25–32.

81. Hawkins, E. D., D. Duarte, O. Akinduro, R. A. Khorshed, D. Passaro, M. Nowicka, L. Straszkowski, M. K. Scott, S. Rothery, N. Ruivo, K. Foster, M. Waibel, R. W. Johnstone, S. J. Harrison, D. A. Westerman, H. Quach, J. Gribben, M. D. Robinson, L. E. Purton, D. Bonnet, and C. Lo Celso. 2016. T-cell acute leukaemia exhibits dynamic interactions with bone marrow microenvironments. *Nature* 538: 518–522.

82. Kim, S., L. Lin, G. A. J. Brown, K. Hosaka, and E. W. Scott. 2017. Extended time-lapse in vivo imaging of tibia bone marrow to visualize dynamic hematopoietic stem cell engraftment. *Leukemia* 31: 1582–1592.

83. Chen, Y., A. Maeda, J. Bu, and R. DaCosta. 2016. Femur Window Chamber Model for In Vivo Cell Tracking in the Murine Bone Marrow. *J. Vis. Exp.* .

84. Flusberg, B. A., J. C. Jung, E. D. Cocker, E. P. Anderson, and M. J. Schnitzer. 2005. In vivo brain imaging using a portable 3.9 gram two-photon fluorescence microendoscope. *Opt. Lett.* 30: 2272.

85. Piyawattanametha, W., E. D. Cocker, L. D. Burns, R. P. Barretto, J. C. Jung, H. Ra, O. Solgaard, and

M. J. Schnitzer. 2009. In vivo brain imaging using a portable 2.9 g two-photon microscope based on a microelectromechanical systems scanning mirror. *Opt. Lett.* 34: 2309–11.

86. Barretto, R. P. J., B. Messerschmidt, and M. J. Schnitzer. 2009. In vivo fluorescence imaging with high-resolution microlenses. *Nat. Methods* 6: 511–2.

87. Barretto, R. P. J., T. H. Ko, J. C. Jung, T. J. Wang, G. Capps, A. C. Waters, Y. Ziv, A. Attardo, L. Recht, and M. J. Schnitzer. 2011. Time-lapse imaging of disease progression in deep brain areas using fluorescence microendoscopy. *Nat. Med.* 17: 223–8.

88. Messerschmidt, B. 2011. Gradient Index (GRIN) Lenses. *www.grintech.de* 1.

89. Inman, J. M., S. N. Houde-Walter, B. L. McIntyre, Z. M. Liao, R. S. Parker, and V. Simmons. 1996. Chemical structure and the mixed mobile ion effect in silver-for-sodium ion exchange in silicate glasses. *J. Non. Cryst. Solids* 194: 85–92.

90. Kawamoto, T. 2003. Use of a new adhesive film for the preparation of multi-purpose fresh-frozen sections from hard tissues, whole-animals, insects and plants. *Arch. Histol. Cytol.* 66: 123–143.

91. Movat, H. Z. 1955. Demonstration of all connective tissue elements in a single section; pentachrome stains. *AMA. Arch. Pathol.* 60: 289–95.

92. Lassailly, F., K. Foster, L. Lopez-Onieva, E. Currie, and D. Bonnet. 2013. Multimodal imaging reveals structural and functional heterogeneity in different bone marrow compartments: functional implications on hematopoietic stem cells. *Blood* 122: 1730–40.

93. Gerber, C., J. W. Mast, and R. Ganz. 1990. Biological internal fixation of fractures. *Arch. Orthop. Trauma Surg.* 109: 295–303.

94. Histing, T., M. Klein, A. Stieger, D. Stenger, R. Steck, R. Matthys, J. H. Holstein, P. Garcia, T. Pohlemann, and M. D. Menger. 2012. A new model to analyze metaphyseal bone healing in mice. *J. Surg. Res.* 178: 715–21.

95. Gautier, E., J. Cordey, R. Mathys, B. Rahn, and S. Perren. 1984. Porosity and remodeling of plated bone after internal fixation: Result of stress shielding or vascular damage. In *Biomaterials and biomechanics.* Elsevier, Amsterdam. 195–200.

96. Victora, G. D., T. A. Schwickert, D. R. Fooksman, A. O. Kamphorst, M. Meyer-Hermann, M. L. Dustin, and M. C. Nussenzweig. 2010. Germinal Center Dynamics Revealed by Multiphoton Microscopy with a Photoactivatable Fluorescent Reporter. *Cell* 143: 592–605.

97. Mayer-Kuckuk, P., T. P. F. Gade, I. M. Buchanan, M. Doubrovin, L. Ageyeva, J. R. Bertino, A. L. Boskey, R. G. Blasberg, J. A. Koutcher, and D. Banerjee. 2005. High-Resolution Imaging of Bone Precursor Cells Within the Intact Bone Marrow Cavity of Living Mice. *Mol. Ther.* 12: 33–41.

98. Kim, J., P. Chhour, J. Hsu, H. I. Litt, V. A. Ferrari, R. Popovtzer, and D. P. Cormode. 2017. Use of Nanoparticle Contrast Agents for Cell Tracking with Computed Tomography. *Bioconjug. Chem.* 28: 1581–1597.

99. Thunemann, M., B. F. Schörg, S. Feil, Y. Lin, J. Voelkl, M. Golla, A. Vachaviolos, U. Kohlhofer, L. Quintanilla-Martinez, M. Olbrich, W. Ehrlichmann, G. Reischl, C. M. Griessinger, H. F. Langer, M. Gawaz, F. Lang, M. Schäfers, M. Kneilling, B. J. Pichler, and R. Feil. 2017. Cre/lox-assisted non-invasive in vivo tracking of specific cell populations by positron emission tomography. *Nat. Commun.* 8: 444.

100. Edinger, M., Y.-A. Cao, M. R. Verneris, M. H. Bachmann, C. H. Contag, R. S. Negrin, M. Heim, and W. Wilmanns. 2003. Revealing lymphoma growth and the efficacy of immune cell therapies using in vivo bioluminescence imaging. *Blood* 101: 640–8.

101. Hauser, A. E., G. F. Debes, S. Arce, G. Cassese, A. Hamann, A. Radbruch, and R. a Manz. 2002. Chemotactic responsiveness toward ligands for CXCR3 and CXCR4 is regulated on plasma blasts during the time course of a memory immune response. *J. Immunol.* 169: 1277–82.

102. Reif, K., E. H. Ekland, L. Ohl, H. Nakano, M. Lipp, R. Förster, and J. G. Cyster. 2002. Balanced responsiveness to chemoattractants from adjacent zones determines B-cell position. *Nature* 416: 94–99.

103. Lo Celso, C., C. P. Lin, and D. T. Scadden. 2011. In vivo imaging of transplanted hematopoietic stem and progenitor cells in mouse calvarium bone marrow. *Nat. Protoc.* 6: 1–14.

104. Wu, J. W., J. M. Runnels, and C. P. Lin. 2014. Intravital imaging of hematopoietic stem cells in the mouse skull. *Methods Mol. Biol.* 1185: 247–265.

105. Lewandowski, D., V. Barroca, F. Ducongé, J. Bayer, J. T. Van Nhieu, C. Pestourie, P. Fouchet, B. Tavitian, and P.-H. H. Roméo. 2010. In vivo cellular imaging pinpoints the role of reactive oxygen species in the early steps of adult hematopoietic reconstitution. *Blood* 115: 443–452.

106. Bremer, D., F. Pache, R. Günther, J. Hornow, V. Andresen, R. Leben, R. Mothes, H. Zimmermann, A. U. Brandt, F. Paul, A. E. Hauser, H. Radbruch, and R. Niesner. 2016. Longitudinal intravital imaging of the retina reveals long-term dynamics of immune infiltration and its effects on the glial network in experimental autoimmune uveoretinitis, without evident signs of neuronal dysfunction in the ganglion cell layer. *Front. Immunol.* 7.

107. Gibson, V. B., R. A. Benson, K. J. Bryson, I. B. McInnes, C. M. Rush, G. Grassia, P. Maffia, E. J. Jenkinson, A. J. White, G. Anderson, J. M. Brewer, and P. Garside. 2012. A novel method to allow noninvasive, longitudinal imaging of the murine immune system in vivo. *Blood* 119: 2545–2551.

108. Tokoyoda, K., T. Egawa, T. Sugiyama, B.-I. Il Choi, and T. Nagasawa. 2004. Cellular niches controlling B lymphocyte behavior within bone marrow during development. *Immunity* 20: 707–18.

109. Motoike, T., S. Loughna, E. Perens, B. L. Roman, W. Liao, T. C. Chau, C. D. Richardson, T. Kawate, J. Kuno, B. M. Weinstein, D. Y. Stainier, and T. N. Sato. 2000. Universal GFP reporter for the study of vascular development. *Genesis* 28: 75–81.

110. Ricard, C., and F. C. Debarbieux. 2014. Six-color intravital two-photon imaging of brain tumors and their dynamic microenvironment. *Front. Cell. Neurosci.* 8.

111. Entenberg, D., J. Wyckoff, B. Gligorijevic, E. T. Roussos, V. V Verkhusha, J. W. Pollard, and J. Condeelis. 2011. Setup and use of a two-laser multiphoton microscope for multichannel intravital fluorescence imaging. *Nat. Protoc.* 6: 1500–1520.

112. Rodriguez, E. A., R. E. Campbell, J. Y. Lin, M. Z. Lin, A. Miyawaki, A. E. Palmer, X. Shu, J. Zhang, and R. Y. Tsien. 2017. The Growing and Glowing Toolbox of Fluorescent and Photoactive Proteins. *Trends Biochem. Sci.* 42: 111–129.

113. Day, R. N., and M. W. Davidson. 2009. The fluorescent protein palette: tools for cellular imaging. *Chem. Soc. Rev.* 38: 2887.

114. Bixel, M. G., A. P. Kusumbe, S. K. Ramasamy, K. K. Sivaraj, S. Butz, D. Vestweber, and R. H. Adams. 2017. Flow Dynamics and HSPC Homing in Bone Marrow Microvessels. *Cell Rep.* 18: 1804–1816.

115. Cipitria, A., K. Boettcher, S. Schoenhals, D. S. Garske, K. Schmidt-Bleek, A. Ellinghaus, A. Dienelt, A. Peters, M. Mehta, C. M. Madl, N. Huebsch, D. J. Mooney, and G. N. Duda. 2017. In-situ tissue regeneration through SDF-1α driven cell recruitment and stiffness-mediated bone regeneration in a critical-sized segmental femoral defect. *Acta Biomater.* 60: 50–63.

116. Mehta, M., K. Schmidt-Bleek, G. N. Duda, and D. J. Mooney. 2012. Biomaterial delivery of morphogens to mimic the natural healing cascade in bone. *Adv. Drug Deliv. Rev.* 64: 1257–76.

117. Kim, T. H., Y. Zhang, J. Lecoq, J. C. Jung, J. Li, H. Zeng, C. M. Niell, and M. J. Schnitzer. 2016. Long-Term Optical Access to an Estimated One Million Neurons in the Live Mouse Cortex. *Cell Rep.* 17: 3385–3394.

6. Printed versions of the selected publications

Reismann et al.

Please also refer to the following link to digitally access the supplementary movies:

https://doi.org/10.1038/s41467-017-01538-9

ARTICLE

# Longitudinal intravital imaging of the femoral bone marrow reveals plasticity within marrow vasculature

David Reismann[1], Jonathan Stefanowski[1,2], Robert Günther[1], Asylkhan Rakhymzhan[1], Romano Matthys [3], Reto Nützi[3], Sandra Zehentmeier[1,2,6], Katharina Schmidt-Bleek [4], Georg Petkau[1], Hyun-Dong Chang[1], Sandra Naundorf[1], York Winter[5], Fritz Melchers[1], Georg Duda[4], Anja E. Hauser[1,2] & Raluca A. Niesner[1]

The bone marrow is a central organ of the immune system, which hosts complex interactions of bone and immune compartments critical for hematopoiesis, immunological memory, and bone regeneration. Although these processes take place over months, most existing imaging techniques allow us to follow snapshots of only a few hours, at subcellular resolution. Here, we develop a microendoscopic multi-photon imaging approach called LIMB (longitudinal intravital imaging of the bone marrow) to analyze cellular dynamics within the deep marrow. The approach consists of a biocompatible plate surgically fixated to the mouse femur containing a gradient refractive index lens. This microendoscope allows highly resolved imaging, repeatedly at the same regions within marrow tissue, over months. LIMB reveals extensive vascular plasticity during bone healing and steady-state homeostasis. To our knowledge, this vascular plasticity is unique among mammalian tissues, and we expect this insight will decisively change our understanding of essential phenomena occurring within the bone marrow.

[1] Deutsches Rheuma-Forschungszentrum, A Leibniz Institute, Charitéplatz 1, 10117 Berlin, Germany. [2] Immune Dynamics, Charité—Universitätsmedizin, Charitéplatz 1, 10117 Berlin, Germany. [3] RISystem AG, Talstraße 2A, 7270 Davos Platz, Switzerland. [4] Julius Wolff Institute, Charité—Universitätsmedizin, Augustenburger Platz 1, 13353 Berlin, Germany. [5] Humboldt-Universität zu Berlin, Unter den Linden 6, 10099 Berlin, Germany. [6] Present address: Department of Immunobiology, Yale University School of Medicine, New Haven, CT 06519, USA. David Reismann and Jonathan Stefanowski contributed equally to this work. Anja E. Hauser and Raluca A. Niesner jointly supervised this work. Correspondence and requests for materials should be addressed to A.E.H. (email: hauser@drfz.de) or to R.A.N. (email: niesner@drfz.de)

ARTICLE

The bone marrow is the birthplace of hematopoietic cells in adult mammals. As such, it is a highly dynamic environment, where new blood cells are constantly generated from proliferating hematopoietic precursors and exit the bone marrow into the circulation[1]. At the same time, the bone marrow serves as a harbor for memory cells of the immune system, which reside in the various subtly different microenvironments that support specific immune cell types[2]. These microenvironments are characterized by specialized stromal cell populations, which compose stable components of the niches[3] and provide essential signals for the differentiation and survival of the hematopoietic cells that occupy these niches.

ARTICLE
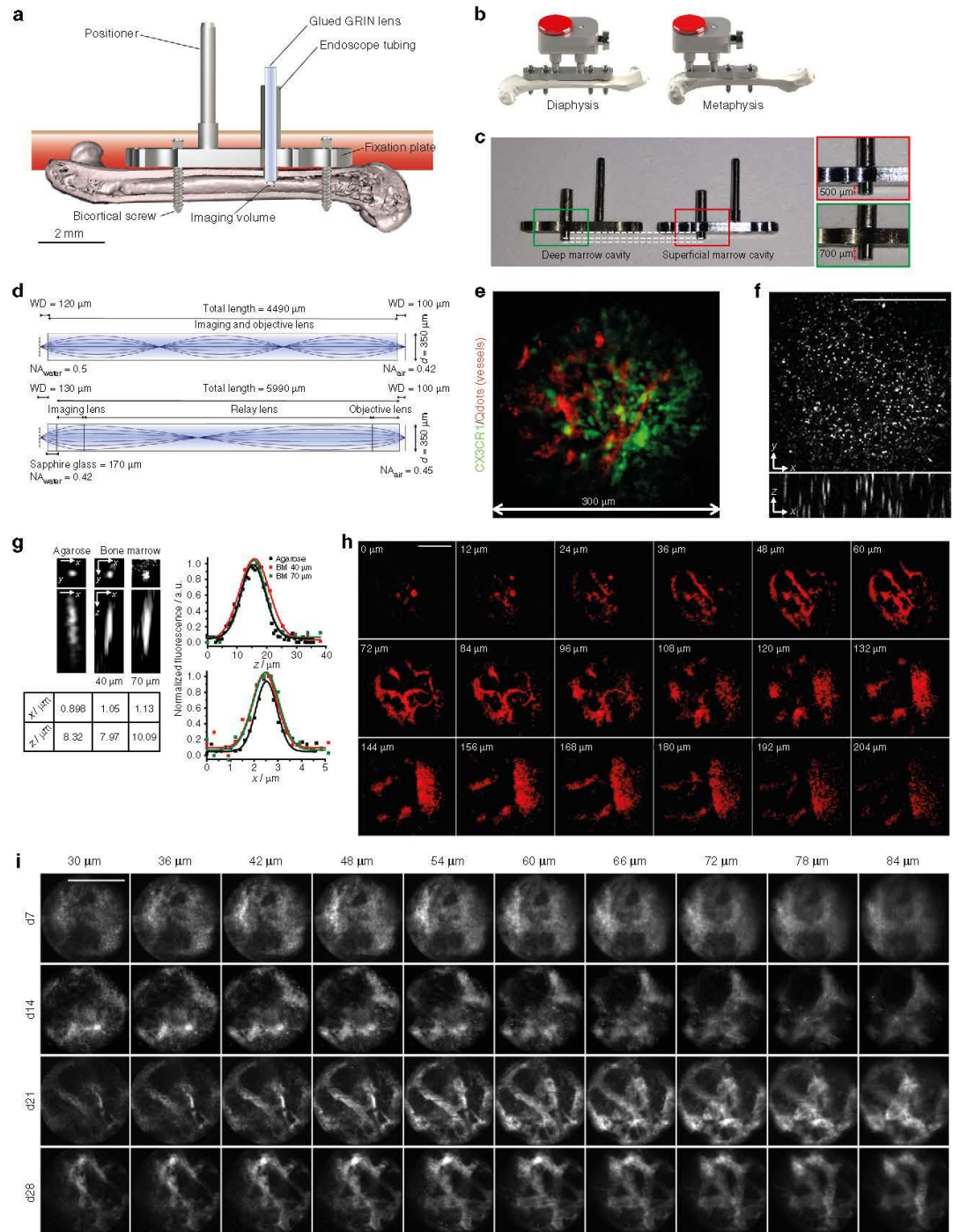
In order to fulfill these functions, the bone marrow tissue is traversed by a dense system of blood vessels comprising arteries, distal arterioles, and sinusoids. These are responsible for transporting cells entering and exiting the bone marrow[4, 5], and also for delivering oxygen, nutrients, and growth factors[1]. The marrow vasculature plays a key role in the regulation of hematopoiesis[6], and hematopoietic stem cell niches are located perivascularly. Recently, a strong link between angiogenesis and osteogenesis, mediated by a defined vessel subtype, characterized by $CD31^{hi}Emcn^{hi}$ (type H) endothelium has been described in the bone marrow. This finding revealed a previously unknown heterogeneity among blood vessels in the bone marrow, supporting the notion of tight functional interactions between marrow and bone[7].

In the recent decade, intravital two-photon microscopy has significantly advanced our understanding of dynamic processes within the immune system. Within the bone marrow, intravital microscopy has helped to elucidate mechanisms of hematopoiesis[8], mobilization of hematopoietic cells[5, 9], and the maintenance of immunological memory[3, 10]. In mice, intravital imaging of bone marrow in areas close to the bone cortex has been performed either in the calvarium[11–13], in the tibia[3, 14], or in the femur[15, 16]. The calvarial preparation takes advantage of the thin sheet of flat bone covering the marrow in this area. Imaging the bone marrow of long bones is more invasive, as it requires the surgical ablation of cortical bone. Both methods have been used mainly as terminal procedures, although imaging at multiple time points has been used for intravital microscopy of both calvarium[17, 18] and long bones (femur and tibia) for imaging durations of hours, over a maximum of 40 days[15, 16]. Nevertheless, up to now there is no available method enabling longitudinal intravital microscopy of the deeper marrow regions in long bones, at subcellular resolution, over the time course of several weeks or even months, i.e., both during bone healing and during homeostasis. In order to understand the cellular dynamics occurring in those marrow regions over longer periods of time, an intravital imaging approach allowing longitudinal observation of a fixed region within the bone marrow in one and the same subject is needed.

The development of permanent windows for the brain cortex[19] or of the spinal cord[20] solved the challenge of longitudinal imaging, but limitations regarding the accessibility of deep tissue areas still remained. An elegant solution for this problem was provided by the lab of Marc Schnitzer[21], who used gradient refractive index (GRIN) endoscopic lenses implanted into the brain cortex in order to image deep cortical layers over several weeks. An endoscopic approach was also used previously for single-photon imaging in the femur, by introducing a fiber-optic probe into the femoral cavity through the knee area. This method

was used for imaging within a single-plane circular field of view of 300 μm diameter and at a lateral resolution of 3.3 μm. The imaged tissue areas were located at 10–15 μm distance from the endoscope tip[22].

Here, we present a novel method called longitudinal intravital imaging of the bone marrow (LIMB), which allows repeated imaging of the same tissue region in the bone marrow of living mice over the time course of up to 115 days. The approach enables sub-cellular resolution multi-photon imaging of cylindrical tissue volumes ($300 \times 300 \times 200 \ \mu m^3$) and is based on the use of a GRIN endoscopic lens mounted on a specialized holder that is surgically fixated to the femur of the mouse. By 28 days postsurgery, reactive processes of the organism to the implant completely cease, and the tissue reaches equilibrium. Using our technique, we are able to demonstrate a high degree of structural plasticity of deep bone marrow vessels not only during bone healing following lens implantation, but also in steady-state homeostasis, with implications for the concepts of microenvironmental stability and niche formation.

Results

Characterization and optical performance of the LIMB implant. In order to understand tissue and cellular dynamics in the bone marrow on a longer time scale, we developed a biocompatible implant—the LIMB implant, which allows microendoscopic imaging of the femoral bone marrow.

The implant is based on a fixation plate originally developed to stabilize the mouse femur after osteotomy[23]. Based on the principles of low contact plates developed for fracture healing[23–27], stability is achieved via two angle-stable bi-cortical screws (Fig. 1a, Supplementary Fig. 1d), which fix the plate in a "bridging" position above the bone, to avoid direct contact to the bone surface. This prevents any compression of the bone.

In order to allow repeated intravital imaging deep within the femoral bone marrow, a titanium alloy tube of 600 μm outer diameter and 450 μm inner diameter is mounted onto the fixation plate (Fig. 1a; Supplementary Fig. 1). To account for tissue heterogeneity and to visualize the different bone marrow areas of the femur, two types of implants were designed, allowing us to access either diaphyseal or metaphyseal regions (Fig. 1b). By varying the length of the endoscopic tubing in the marrow cavity (e.g., 500 vs. 700 μm, Fig. 1c), we can image pericortical tissue areas or areas deep in the marrow. For instance, by using a long microendoscopic tubing, we can visualize the endosteum on the opposite side of the bone cortex, in a contact-free manner.

A GRIN lens (Fig. 1d) is positioned in the endoscope tubing and used as a lens for imaging. We use two GRIN lens designs,

Fig. 1 LIMB allows murine long bone imaging in various locations with high resolution. **a** Design and positioning of LIMB implant for longitudinal bone marrow imaging. The LIMB implant is fixed onto the femur using bi-cortical angle-stable screws. GRIN lens systems are placed within the endoscope tubing for imaging and sealed to ensure sterility. The positioner allows adjustment and alignment of GRIN and microscope optical axes. **b** In order to account for tissue heterogeneity, i.e., metaphyseal vs. diaphyseal regions, alternative LIMB designs have been developed. LIMB fixation with four screws allows higher bone stability after osteotomies. **c** Tubing lengths of 500 and 700 μm, respectively, allow access to either peri-cortical or deep marrow regions. **d** Two GRIN lens systems are used for imaging. The single GRIN lens (upper panel) combines the imaging and objective lens function and is glued into the endoscope tubing. The symmetric triple GRIN lens (lower panel) is exchangeable and a sapphire window seals the endoscope tubing. **e** 3D fluorescence image of the bone marrow of a CX_3CR1:GFP mouse using the single GRIN lens (myeloid CX_3CR1^+ cells - green; vasculature labeled by Qdots - red). The maximum field of view is circular, with 280 μm diameter. **f** The PSF was measured on 100 nm beads ($\lambda_{em} = 605$ nm, $\lambda_{exc} = 850$ nm) in agarose, using the single GRIN lens. No significant wave-front distortions affecting the PSF are observed. **g** Qdots are used to estimate PSF in marrow tissue. They reveal slight resolution deterioration with increasing imaging depth. **h** 2D fluorescence images of Qdots-labeled femoral vasculature, 35 days post-surgery, at various z-positions between the surface of the single GRIN lens and 204 μm tissue depth. They reveal fine vascularization in the upper layers and a large blood vessel (~100 μm diameter) with emerging branches in the deep marrow. **i** 2D fluorescence images of femoral vasculature acquired at various depths and time points post-surgery, using the triplet GRIN lens. The tissue at the contact surface with the window is characterized by de novo micro-vascularization, i.e., granulation tissue. Its thickness varies between individuals and decreases over time after implantation. Scale bars = 100 μm

both with a diameter of 350 μm. The first design (Fig. 1d, upper panel) consists of one single GRIN lens of 4.49 mm in length, a numerical aperture (NA) of 0.5 at the object side and a field of view of 280 μm in diameter (Fig. 1e). The lens is permanently and stably glued into the tubing, thereby sealing it to maintain sterility within the marrow cavity and ensuring fixed positioning of the optical path. The second design (Fig. 1d, lower panel) consists of a system of three GRIN lenses with NA 0.42 at the object side,

5.99 mm in length and a field of view of 150 μm diameter. This GRIN system requires a 170 μm thick sapphire window for optimal optical performance, which is attached to the tubing and seals the implant. Thus, this design allows flexible replacement of the GRIN lens system for applications requiring different optical properties. A 45° prism can be glued at the end of the GRIN lens to achieve a side view of the marrow tissue and access additional tissue areas.
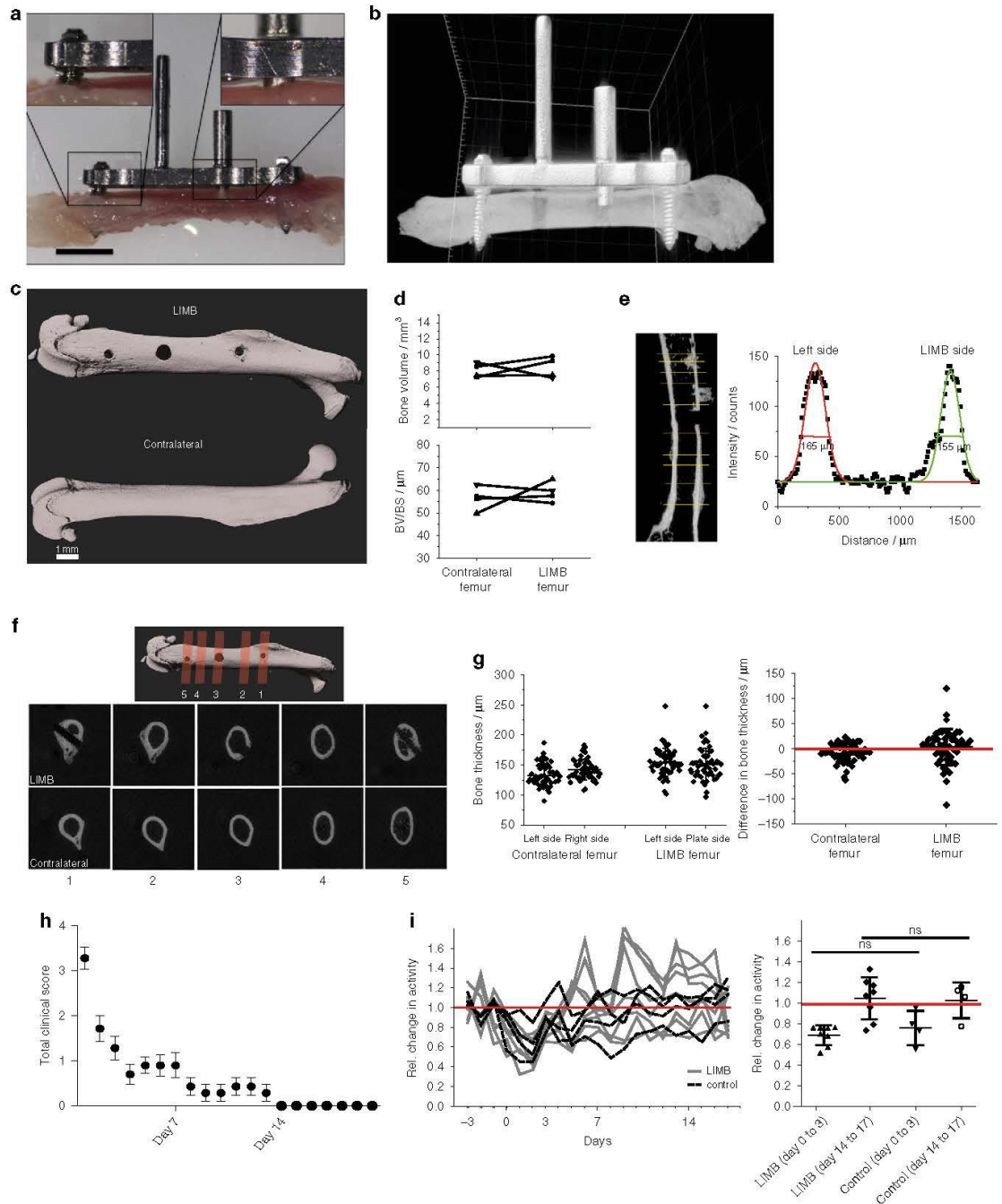
The LIMB implant is surgically fixated onto the right femur of mice (Supplementary Figs. 2b, 3) to intravitally visualize tissue dynamics by multi-photon microscopy. The use of multi-photon excitation permits imaging deep into tissue. The implant is completed by a titanium-alloy reference plate (Fig. 1b, Supplementary Figs. 1, 2a) mounted onto the positioner and the endoscope tubing, which allows stable, reproducible positioning of the mice under the microscope. This reference plate couples with a custom-built adapter used to align the optical axes of the microscope objective lens (20×, NA 0.45) and of the GRIN lens, thereby transferring the focus from the microscope objective through the GRIN lens into the marrow tissue (Supplementary Figs. 2b, 3h).

To characterize the optical properties of LIMB, we first determined the point spread function (PSF) of the GRIN lens systems using 100 nm fluorescent beads (emission at 605 nm, excitation at 850 nm) in agarose. Using the one-lens GRIN design, the spatial resolution was 0.8 ± 0.1 µm (s.d.) laterally and 5.2 ± 0.5 µm axially, corresponding to theoretical values for NA 0.5 ($n = 23$ beads). The three-dimensional PSF was not distorted by optical aberrations over the entire field of view (Fig. 1f). Using the three-lens GRIN system with the sapphire glass window, we measured a spatial resolution of 0.9 ± 0.2 µm laterally and 8.0 ± 1.1 µm axially (Fig. 1g), also corresponding to the theoretical values for NA 0.42 ($n = 18$ beads).

Within the bone marrow, the spatial resolution was evaluated using quantum dots 655 (Qdots). While most of these nanoparticles remained within the blood vessels, some Qdots entered the parenchyma due to the fenestrated sinusoids of the bone marrow and were observed as single fluorescent spheres of sub-resolution sizes. Typically, resolution values of 1.0 ± 0.1 µm laterally and 7.4 ± 1.6 µm axially were achieved within the imaging volume between 40 and 70 µm distance from the surface of the GRIN lens (at each depth, $n = 8$ Qdots).

The maximum extent of the imaging volume within the bone marrow using the one-lens GRIN system started from the endoscope surface at 0 µm and reached down to 204 µm within the bone marrow (Fig. 1h). It included regions with superficial small sinusoids and arterioles, as well as deeper-laying large blood vessels including the central sinus. We reliably achieved a signal-to-noise ratio of at least 5, independent of inter-individual variance and of the imaging time point after surgery.

At early time points post-surgery, we typically visualized granulation tissue, characterized by a tight network of small blood vessels within a large area in the imaging volume (~30–85 µm in depth). Over time, this granulation tissue retracted to the area next to the GRIN optics and was replaced by normal-appearing bone marrow vasculature, resembling the vasculature as observed by calvarial and tibial imaging preparations. At late time points post-surgery, from 28 days onwards, we observed complete resolution of this granulation layer (Fig. 1i).

Local and overall tissue recovery after implantation. First, we determined to what extent the surgical procedure and the presence of the implant itself affected the mice and impacted on bone physiology. As shown in Fig. 2a, b and Supplementary Movie 1, we confirmed that the low contact plate design does not compress the bone, instead, a gap of at least 100 µm remained between bone surface and plate. After removal of the plate (day 7 post-implantation), reconstructed µCT images of the bone surface appeared smooth in the area where the plate had been, comparable to the surface of contralateral bones (Fig. 2c). Furthermore, no differences in bone volume, ratio of bone volume to bone surface (BV/BS), bone shape or thickness were found between the LIMB-implanted and contralateral femurs (Fig. 2d–g). In order to determine the impact of the surgery on the mice, we clinically scored the animals immediately after LIMB implantation, taking parameters such as weight, general appearance, and vitality into account. The data recorded from 79 mice indicate that the animals reached a low level of burden (as reflected in a score of 1) by post-surgical day 3, and normal values for all parameters were reached within 14 days after surgery (Fig. 2h). In addition, the general activity of mice that received the LIMB implant was recorded, starting 3 days pre-surgery until 18 days post-surgery (Fig. 2i, left panel). By transponder-based tracking, we recorded the movement of each mouse, thereby generating individual motility profiles of LIMB-implanted and co-housed mice, which had undergone sham treatment (without implantation). The mean activity levels dropped to a similar extent in both implanted and sham-treated groups within 3 days post-surgery, when compared to pre-surgical levels. By day 14 after surgery, at a time point when clinical scores were normal again (Fig. 2h), the activity of the mice in both groups also returned to pre-surgical levels (Fig. 2i, right panel). Interestingly, at both early and late time points post-surgery, there were no significant differences between sham-treated and LIMB-implanted mice. In order to analyze the effects of the surgical intervention and of the implant on the gait of the animals, the open-field behavior of the mice was recorded (Supplementary Movie 2) at day 2, 6, 9, 13, and 21 post-surgery. No severe gait abnormalities were observed at any time ($n = 79$).

In order to assess the effects of the LIMB implant on the bone with respect to post-surgical inflammation and bone formation adjacent to the LIMB microendoscope, we performed immunofluorescence and histochemical analysis (Fig. 3a–c). The most striking changes within the marrow of the implant-bearing

Fig. 2 Effect of LIMB implantation on bone tissue, general health, and activity of the mice. **a** Picture of an explanted femur including the LIMB implant shows the fixation plate bridging between the angle-stable screws, thereby preventing direct contact to the bone surface/periosteum. Scale bar = 2 mm. **b** 3D reconstructed µCT images of a femur bearing the LIMB implant confirm no direct contact between bone and fixation plate. Shadows below the positioner are beam hardening artifacts of the high attenuation titanium alloy. **c** 3D reconstructed µCT images of an intact femur (lower panel) and a femur after removal of the LIMB implant (upper panel). Bone surface under the fixation plate 7 days after implantation appears similar to the bone surface of the intact femur. Bone growth is observed only around the bicortical screws. **d** Total bone volume (upper panel) and BV/BS (lower panel) of LIMB and contralateral femur, respectively ($n = 4$ mice). **e** Longitudinal cross-section through a µCT reconstruction of a femur after implant removal (left panel). Yellow lines represent the positions chosen to measure the bone thickness. For each position, the intensity profile was approximated with two Gaussian curves as indicated in the left graph. **f** 3D reconstruction of µCT data showing the planes of transverse cross-sections displayed in the lower two panels. At day 21 after implantation, calcified bone forms around the bicortical screws, but not around the endoscope tubing. Cross-section µCT images at the sites of the screws show enough space for the bone marrow tissue to connect the diaphysis with the metaphysis. **g** No differences in bone thickness between contralateral and LIMB femurs are measured ($n = 5$ mice). **h** Total clinical score over 3 weeks post-surgery based on behavior and appearance of the individual mice ($n = 79$ mice). **i** Physical activity of LIMB implanted mice, pre-surgery and post-surgery, and of co-housed control mice. The LIMB-implanted mice reach their pre-surgical activity level within the same time as sham-treated controls (right graph) (two independent experiments; $n = 8$

ARTICLE

femurs were an accumulation of CD45$^+$ cells, and enhanced expression of the extracellular matrix (ECM) component laminin in tissue regions around the implant, peaking at day 3 post-surgery. Some of the cells with hematopoietic morphology were Sca-1$^+$ckit$^+$ and may represent progenitors (Supplementary Fig. 4a). We also detected CD45$^-$Sca-1$^+$ cells in elongated structures surrounded by laminin, likely representing arterioles

sprouting into the injured area (Supplementary Fig. 4b). These changes occurred around the sides of the implanted tube and in front of the sapphire glass window, reaching a depth of up to 400 μm. By day 7, the inflamed area as indicated by laminin, Sca-1 and CD45 shrunk to a thickness of ~100 μm. The tissue structure further normalized at day 14 and by day 28, the area in front of the imaging window typically consisted of laminin$^+$ vessels

58

ARTICLE
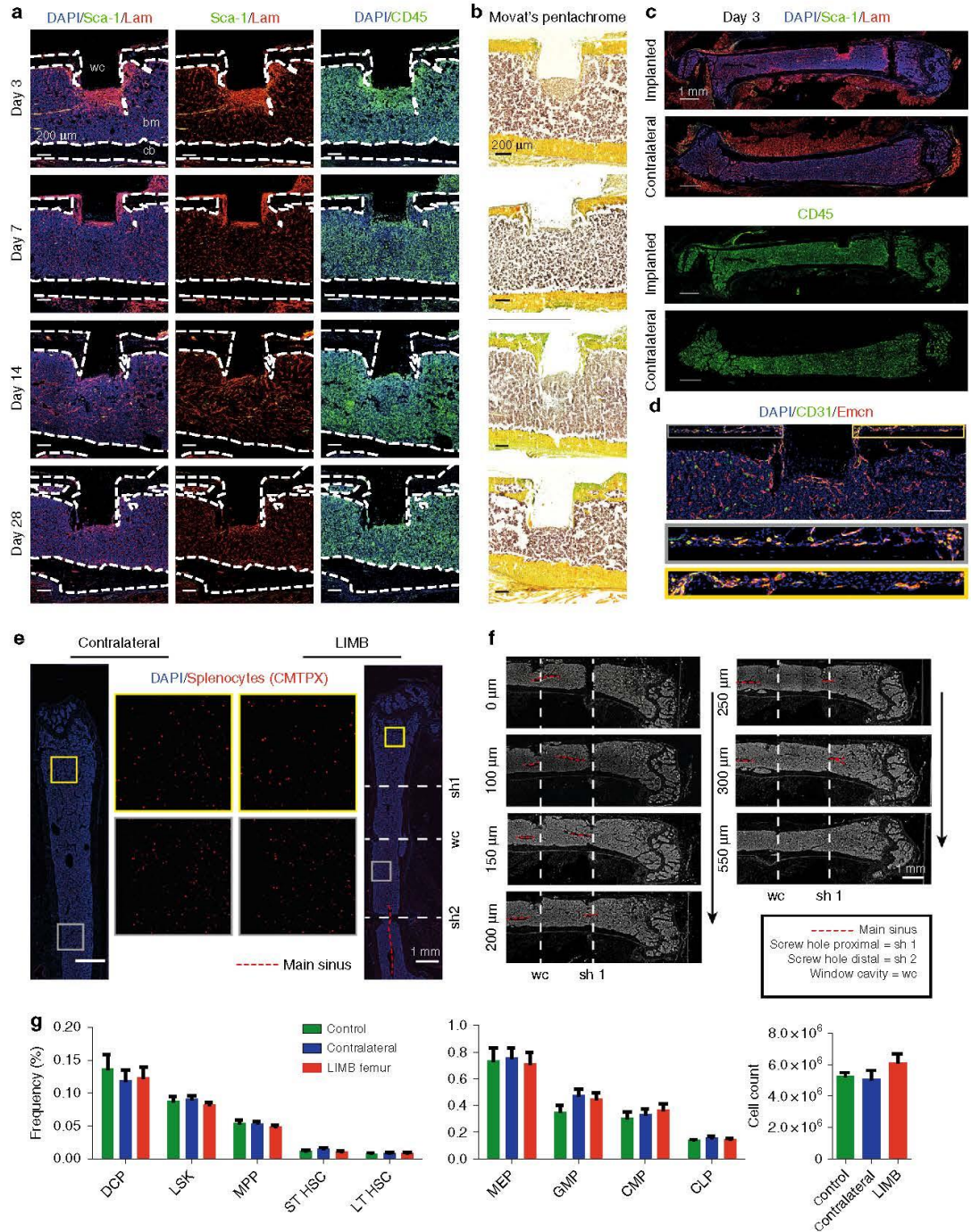
surrounded by CD45^{+} hematopoietic parenchyma, in a pattern resembling the other regions of the bone marrow and the contralateral (non-implant-bearing) femur. Movat's pentachrome staining showed that, although in some mice bone formation occurred lateral to the implanted tube emanating from the cortex, no new bone formed in front of the imaging window. Besides these changes in the tissue occurring adjacent to the implant and screws, the overall structure of the bone marrow was unaltered with respect to the overall distribution of leukocytes, ECM components, and vessels when compared to the contralateral bone (Fig. 3c). At the site of the periosteum, vascularization was detected (Fig. 3d). In order to test whether the implant impairs blood flow throughout the bone, we adoptively transferred CMTPX-labeled splenocytes via the tail vein, harvested the bones 4 h later and analyzed the distribution of CMTPX^{+} cells by fluorescence histology. In histological sections, CMTPX^{+} cells were distributed throughout the marrow in both the contralateral and the LIMB-implanted femurs (Fig. 3e). Importantly, engraftment occurred on both sides of the bicortical screws. Consistent with this observation, longitudinal serial sections showed clearly that the bicortical screw did not completely separate the bone marrow and did not impair the blood flow in any part of the marrow. Additionally, we performed μCT of implanted bones, which also showed clearly that the bone marrow was not completely separated by the bicortical screws (Fig. 3f and Supplementary Movie 1). In order to verify whether hematopoiesis within the bone marrow was altered, we performed flow cytometry on bone marrow cells of LIMB-implanted mice, and quantified the major hematopoietic progenitor populations. No significant differences in the frequencies or total cell counts of the analyzed populations were observed compared to bone marrow from contralateral femurs or bone marrow from non-treated mice (Fig. 3g and Supplementary Fig. 5).

B lymphocyte motility in femur, calvarium, and tibia. In order to observe the dynamics of B-lineage cells within the femoral marrow, we chose *CD19:tdRFP* mice as recipients of the LIMB implant. In these mice, Cre recombinase activity in CD19-expressing cells leads to the removal of a STOP cassette and expression of tdRFP in the B cell lineage, starting in the late pro-B cell stage. The vasculature was labeled using Qdots. Mice were imaged starting at day 7 (Fig. 4a; Supplementary Movies 3, 5–7), up to maximally day 115 post-surgery (Supplementary Movie 12).

Using LIMB in *CD19:tdRFP* mice, under homeostatic conditions, i.e., at day 60 or 90 post-surgery, we found that tdRFP^{+} cells of various volumes displayed different motility patterns. We distinguished the subtypes of B lymphocytes based on their size,

and tracked them to assess their velocity and displacement rate. A maximum diameter of 10 μm corresponds to a spherical volume of ~500 μm[3], therefore these cells presumably represent B cells, displaying a high degree of directed motility, in line with previous reports[5]. Larger tdRFP^{+} cells in this system represent rather static plasma cells, consistent with the concept of their residence in bone marrow niches (Fig. 3c) and with our previous work[3]. In order to compare the motility of B-lineage cells in the femur to other bone marrow compartments, we performed intravital imaging of calvaria and tibia of *CD19:tdRFP* mice. Notably, we found no significant differences in the motility of bone marrow B and plasma cells when comparing femur (LIMB), calvarium, and tibia (Supplementary Movies 4, 8, 9; Fig. 4b–e).

Long-term stability of the LIMB implant. In order to test the positional stability of the LIMB implant, the microendoscope was implanted in mice ubiquitously expressing photoactivatable green fluorescent protein (paGFP). Prior to photoactivation, paGFP is non-fluorescent upon 940 nm illumination. Photoactivation at 840 nm leads to 100-fold increase in green fluorescence upon excitation at 940 nm[28]. PaGFP mice were injected with Qdots to label the vasculature and were imaged before and after photoactivation (Fig. 5a, two upper rows). The photoactivation area was either 75 × 75 or 100 × 100 μm[3] positioned within the center of the field of view (Supplementary Fig. 6). We analyzed paGFP fluorescence by repeated imaging every 6–12 h (Fig. 5a, third to last row) and detected paGFP fluorescence at the same area at least 36 h after photoactivation. Thus, we confirmed the high positioning stability of the LIMB implant with respect to the implantation/imaging site in the bone. The fluorescence signal of paGFP decreases over the time span of hours/days due to the emigration of hematopoietic cells out of the photoactivated region (Supplementary Movies 9, 10) and due to protein turnover, causing fluorescent paGFP to be replaced by newly synthesized, non-fluorescent paGFP. The imaging data acquired in *paGFP* mice reveal that while the field of view labeled by photoactivation remains stable, morphological changes of the vascular system do not cease after day 28 post-surgery and seem to depend on the vessel diameter (Fig. 5a). In order to exclude that such changes are caused by the LIMB implant itself, we performed longitudinal imaging in the calvarium of *paGFP* mice, over a volume of 500 × 500 × 66 μm[3]. We were able to repeatedly detect paGFP fluorescent areas in the calvarial marrow islets for up to 72 h after photoactivation, and observed paGFP cells leaving this area. Similarly to LIMB, we also detected drastic changes in the marrow vasculature, most prominent in smaller vessels (Fig. 5b; Supplementary Fig. 7).

Fig. 3 The bone marrow within the imaging volume reaches steady-state comparable to homeostasis 28 days after LIMB implantation. **a** Immunofluorescence analysis of bone sections after removal of the LIMB implant over the time course of 4 weeks. ECM formation was identified by the marker Laminin (Lam). Stem-cell antigen 1 (Sca-1) is highly expressed in arterioles. The leukocyte marker CD45 indicates localization of inflammatory cells adjacent to the window cavity (wc). Lam is highly expressed around the implant during the first week and completely normalizes after 2–4 weeks. CD45^{+} cell accumulations are found during the first weeks in proximity to the wc. **b** Movat's pentachrome stain detects connective tissues and reveals remodeling of bone primarily on the periosteal interface near the fixation plate. **a, b** Images are representative for 3–5 mice per time point post-surgery. **c** Overview immunofluorescence images of the femoral bones from an individual mouse 3 days post-surgery. Note the specific reaction to the implant-bone marrow interfaces indicated by accumulations of CD45^{+} cells, and Lam^{+} and Sca1^{+} arteries (yellow). bm bone marrow, cb cortical bone. **d** Immunofluorescence image of the region around the endoscope tubing in a LIMB-implanted femur 7 days post-surgery, including the bone cortex and periosteum under the plate. The presence of various blood vessel subsets indicated by CD31 and Emcn demonstrates intact blood supply to the periosteum and to the bone. Scale bar = 100 μm. **e** Blood supply is intact throughout the marrow cavity, indicated by CMTPX-labeled splenocytes, which localize in the bone marrow 4 h after transplantation in both contralateral and LIMB-implanted femurs at 42 days post-surgery (n = 3 mice). **f** Histological DAPI stain (gray) shows intact tissue structure, with no separation of the bone marrow and the vasculature by the screws or endoscope tubing. **g** Flow cytometry analysis of femurs with the LIMB implant, their contralateral femurs and femurs of control mice. Similar frequencies and cell counts of various cell populations shows no effect of the LIMB implant on bone marrow cell composition (n = 8 LIMB-implanted mice, n = 8 controls, two independent experiments). Error bars represent s.e.m. values. Statistical analysis was performed using *t*-test

Vascular plasticity during healing phase and homeostasis. Using LIMB, we observed drastic changes in the vascular morphology within the femoral marrow after implantation, both during the healing phase and after reaching steady-state. These changes were not caused by instability of the microendoscope or by inaccuracy during repeated selection of the imaging volume, as demonstrated by the results of our photoactivation experiments.
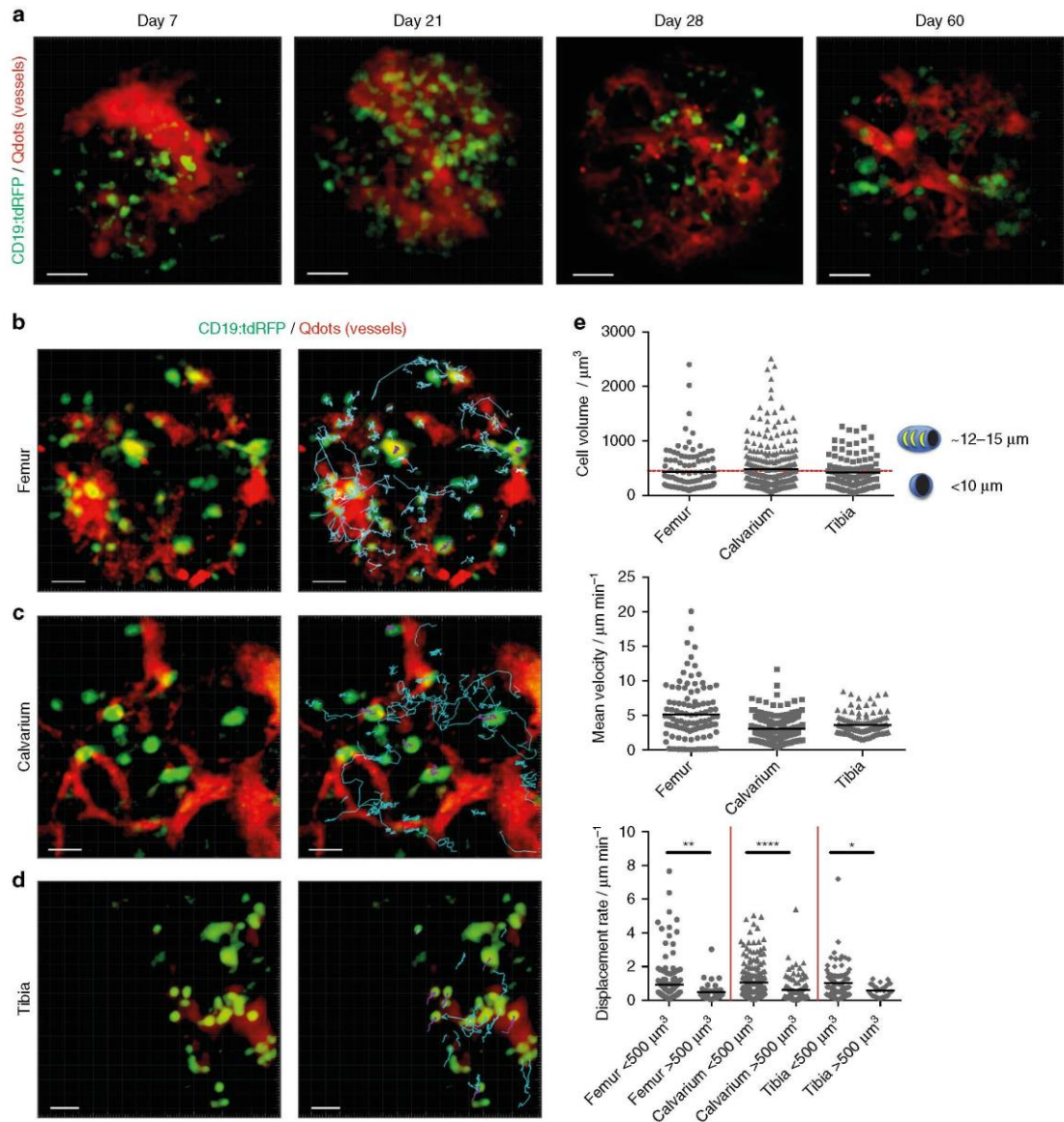

Fig. 4 Immune cell dynamics in different bone types show comparable motility patterns. **a** 3D fluorescence images acquired by LIMB in the femoral marrow of a *CD19:tdRFP* mouse at day 7, day 14, day 28, and day 60 after surgery. Mature B lymphocytes express tdRFP and are displayed in green, whereas the vasculature was labeled with Qdots and is displayed in red. Scale bar = 50 μm. All images are snapshots of 45 min movies, with images acquired every 30 s. The movies are provided as Supplementary Material. **b** Time-lapse 3D fluorescence image acquired by LIMB in the bone marrow of a *CD19:tdRFP* mouse at day 90 post-surgery. The tracks of the B lymphocytes smaller than 500 μm³ (defined as B cells with a maximum diameter of 10 μm) are shown in cyan, whereas those with a volume larger than 500 μm³ (defined as plasma cells) are shown in violet. Scale bar = 30 μm. **c** Similar to **b**, time lapse 3D image of the bone marrow of a *CD19:tdRFP* mouse with corresponding tracks of B and plasma cells in the calvarium and **d** the tibia. Scale bar = 30 μm. Representative movies with cell motility tracks for LIMB, calvarial, and tibial imaging are provided as Supplementary Material. **e** Quantification of cell volumes, mean velocities, and displacement rates of B lymphocytes from movies acquired by LIMB ($n = 4$ mice), within the calvarial bone ($n = 3$ mice), and the tibia ($n = 2$ mice). Similar cell subset frequencies and mean velocities of B lymphocytes were measured by LIMB in the femoral bone marrow, by calvarial imaging as well as by tibial imaging. We statistically analyzed the data in **e** using *t*-test (*$p < 0.05$; **$p < 0.01$; ***$p < 0.001$)

As expected, we observed dynamic blood vessel re-organization between day 7 and 21 post-surgery. Interestingly, even between day 27 and 60, a time span in which the tissue composition in front of the microendoscope is comparable to non-implanted bone marrow (Figs. 2, 3), the vasculature continued to change massively (Fig. 6a). Starting from day 27 post-surgery, with a time
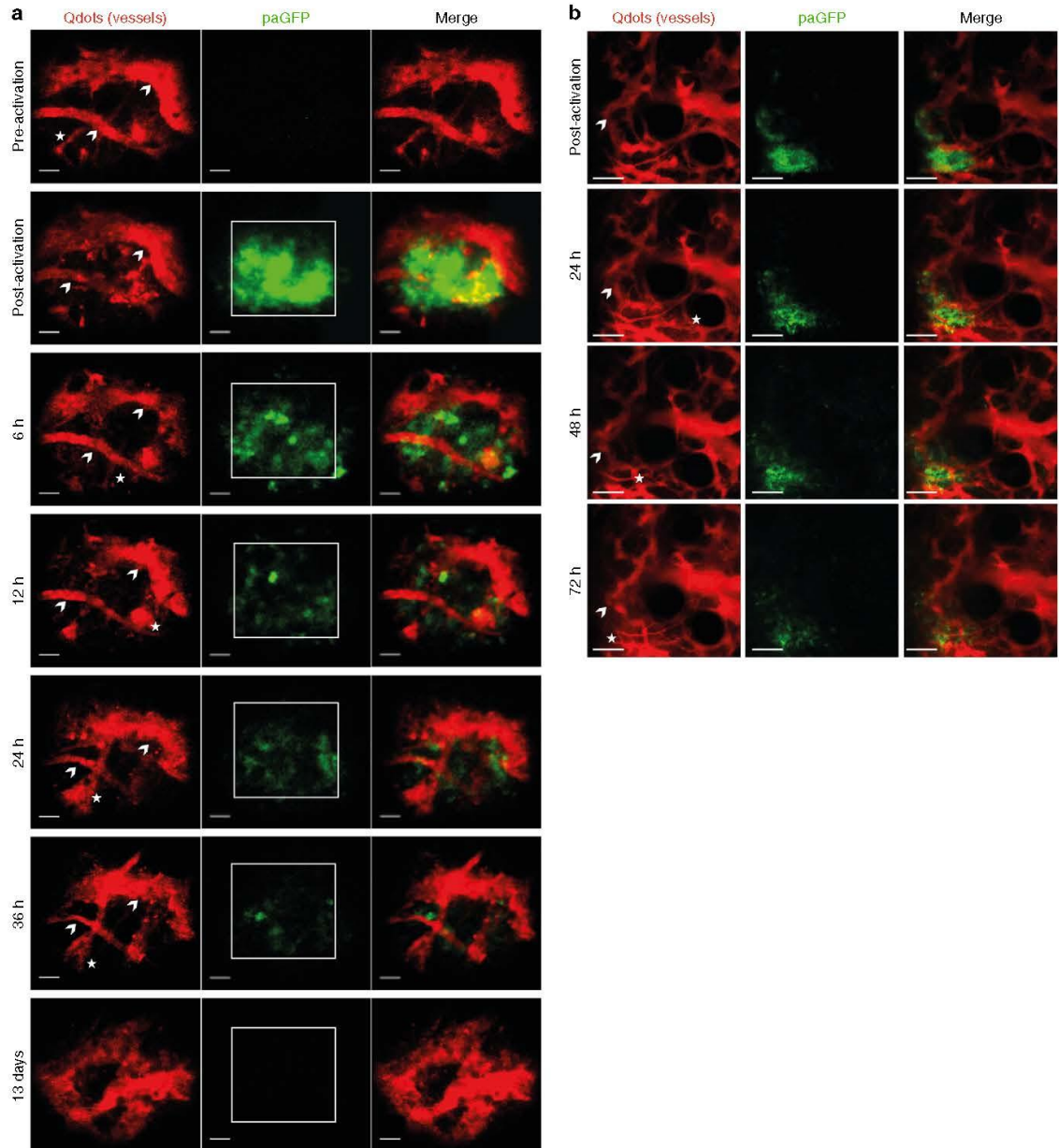

Fig. 5 Imaging of locally activated paGFP in murine deep femoral marrow reveals high positioning stability of the LIMB implant. **a** paGFP mice were implanted with a LIMB microendoscope ($n = 3$ mice). After 35 days, the mice were injected intravenously with Qdots to label the vasculature. Photoactivation of paGFP was performed at a wavelength of 840 nm in a $75 \times 75 \times 30\,\mu m^3$ square area in the center of the field of view. Additional injections of Qdots were given before each recording. We performed the described photoactivation experiments repeatedly, up to three times in the same animal at day 27, 35, and 56 post-surgery, during homeostasis with similar results. Blood vessels which could be observed over the whole period of 36 h are indicated by arrowheads, whereas those that appear or disappear within this time period are labeled by asterisks. Scale bar = 30 μm. **b** Similarly to **a**, photoactivation of a $150 \times 150 \times 9\,\mu m^3$ region within the $500 \times 500 \times 66\,\mu m^3$ field of view in a paGFP mouse with a permanent calvarial imaging window let us easily identify the photoactivated area. The paGFP fluorescence could be visualized over several imaging sessions. Scale bar = 100 μm. During these time windows we observed changes of the vasculature in both, the deep femoral marrow and bone marrow islets of the calvarium

resolution of 7 days between imaging sessions, the pattern of large blood vessels (>50 μm) changed between consecutive time points, making their use as tissue landmarks impossible (Fig. 6b). Only by further increasing the time resolution in LIMB, during the homeostatic phase, i.e., shortening the interval between imaging sessions to every 6–24 h (Fig. 6c), were the vessels stable enough

to be used for orientation. We found that blood vessels with diameters in the range of 5–15 μm had the highest degree of volume change within the time span of 24 h (Fig. 6d, Supplementary Movie 13). Within the same period, large blood vessels (>35 μm) changed rather slowly, whereas middle-sized blood vessels with a diameter between 15–35 μm displayed an

ARTICLE
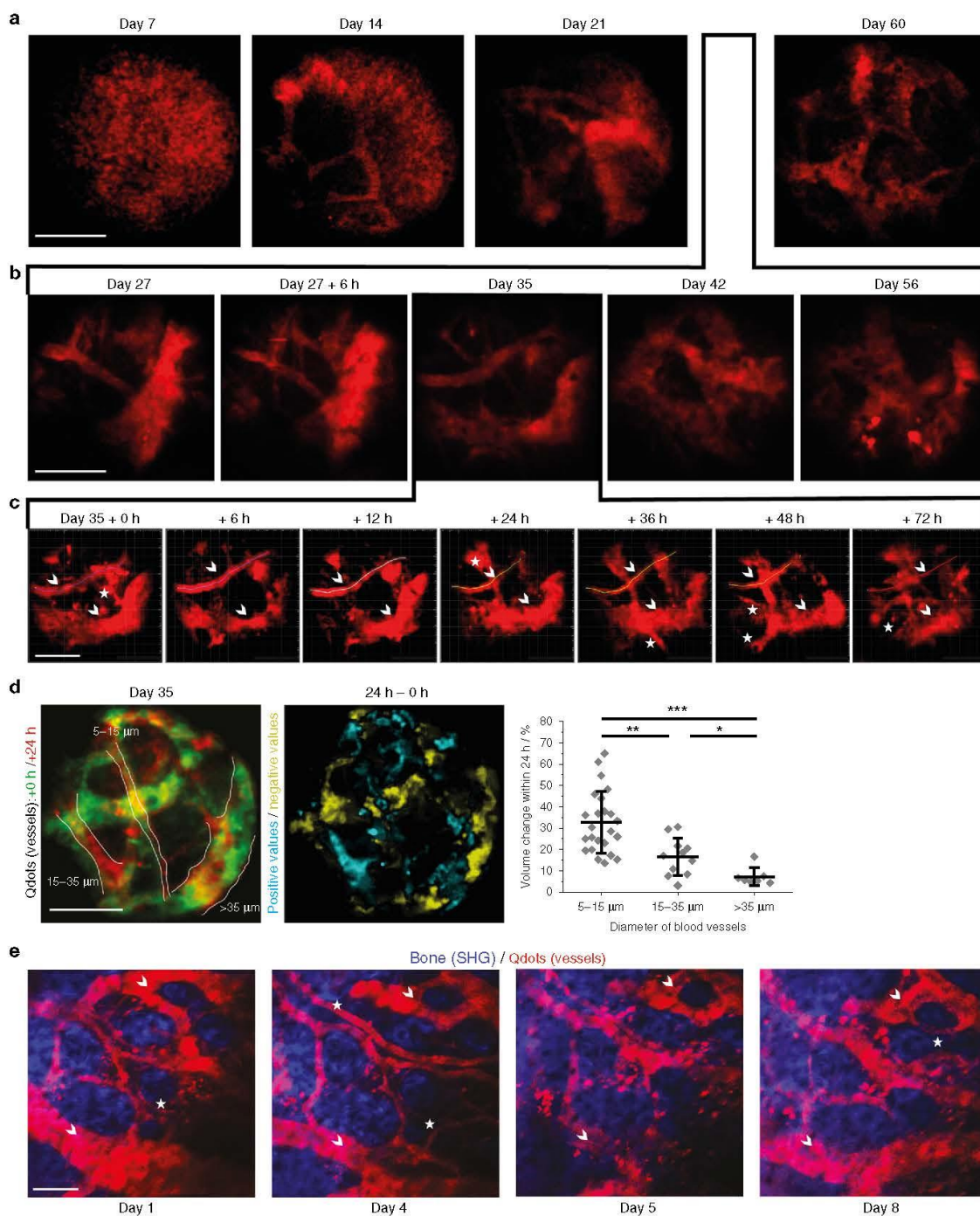
intermediate degree of remodeling. Notably, we observed a comparable remodeling in the vascular compartment of the marrow islets of the calvarium, over a time course of 8 days (Fig. 6e). As the surgery for longitudinal calvarial imaging does not disrupt the integrity of the bone, we can rule out that the vascular plasticity was an effect caused by the femoral implant and confirm the physiological nature of this vascular remodeling. However, due to the fact that calvarial marrow islets are rather small as compared to the cortical bone areas, the dramatic vascular plasticity remained underestimated until now. Only by using LIMB, we were able to observe and quantify these changes.

Possible mechanisms of femoral vascular plasticity. In order to investigate whether vascular remodeling was the result of active angiogenesis related to de novo bone formation, we performed immunofluorescence analysis of bone sections (Fig. 7). A recent publication described CD31^{hi} Endomucin (Emcn)[hi] (type H) bone marrow endothelium to be involved in osteogenesis-related angiogenesis in the bone marrow[7]. In line with previous reports[29], we found type H vessels to be abundant at the growth plate of young mice, but only few type H vessels were present in aged mice (Supplementary Fig. 8a). In contrast, type H vessels close to the bone cortex were found at all ages (Supplementary Fig. 8a), consistent with age-independent bone remodeling at this site. We examined the bone marrow for the presence of type H vessels following implantation (Fig. 7a) and detected them during the early healing phase (days 3–14) in tissue areas next to the microendoscope. At day 28 post-surgery, only few type H vessels were found in proximity of the microendoscope and their shape and abundance were comparable to the vessels present at bone–bone marrow interfaces. Together, this indicates a state of homeostasis, consistent with the previously observed time course of regeneration (Fig. 3).

In line with the vascular remodeling within the bone marrow, we observed marked changes in the stromal network in *Prx-1:YFP* mice (Supplementary Fig. 9). During homeostasis, the stromal network remodeling continues, similar to the vascular reorganization. Repeated imaging experiments in *paGFP* mice every 6–12 h after photoactivation, over a total time of 36 h (Fig. 5), revealed fluorescent cells, presumably stromal cells, persisting over the whole time span of 36 h, as well as highly motile fluorescent cells, presumably hematopoietic cells, leaving the photoactivated volume. Over the course of these 36 h the vasculature continuously changed its shape. In order to assess whether the remodeling process involves proliferation of the endothelial cells, we administered the thymidine analog EdU to label newly synthesized DNA[3] to mice that had received a LIMB implant either 3 or 42 days earlier. EdU labeled a similar fraction and

comparable pattern of hematopoietic cells distributed over the whole bone marrow in both cohorts ($n = 3$ mice in each cohort). We did not detect an overt proliferation of endothelial cells in the tissue surrounding the implant (Fig. 7b). Similarly, staining for the proliferation marker Ki67 did not show any accumulation of proliferating endothelial cells at the implant site, at any time point (Supplementary Fig. 8b). Taken together, these data support the hypothesis that the observed dynamics are the result of passive displacement of the vessels, probably caused by dynamics and cell proliferation in the surrounding tissue (Fig. 7c; Supplementary Movies 10, 11), rather than active proliferation in the vascular compartment. The exact kinetics and mechanisms of the vascular and stromal remodeling during the steady-state will be subject of further studies, as they impact on many processes taking place in the bone marrow.

Discussion

While intravital imaging of the bone marrow has previously been performed[3, 11–18, 22], longitudinal multi-photon imaging in the deep marrow of long bones over the time course of months was not feasible. Longitudinal microscopic and microendoscopic imaging of the CNS[20, 21], retina[30], or lymph nodes transplanted into the ear of mice[31] has been reported, and blood vessels have been used as anatomical reference points, allowing the recognition and imaging of the same regions within the tissue.

The bone marrow contains quiescent and activated hematopoietic stem cells in dedicated perivascular tissue niches[6, 29], and is the tissue in which most leukocytes complete their development. The bone marrow actively participates in immune reactions[32, 33] and is an important site for the maintenance of immunological memory[3, 10, 34, 35]. The interaction of hematopoietic cells with stromal cells plays a crucial role in these processes: subtypes of vascular cells provide niches for the maintenance of hematopoietic stem cell quiescence[6], and stromal cells in the bone marrow provide cytokines, which support the survival and differentiation of developing hematopoietic cells. Endothelial cells mediate leukocyte trafficking between the circulation and the bone marrow parenchyma[6], guiding immune memory cells back into the bone marrow together with stromal cells, which provide chemotactic cues and anchor the memory cells in their niches[36]. Moreover, the role of the immune, vascular and bone compartments during distinct phases of bone regeneration still remain elusive. Hence, there is a clear need for longitudinal imaging technologies to allow the investigation of dynamic processes at the cellular and sub-cellular level in this organ.

The GRIN lens microendoscopic implant presented in this work allows for the first time imaging of dynamic cellular

Fig. 6 LIMB approach reveals kinetics of vascular remodeling during bone healing and homeostasis on time scales from hours to months. C57/B6J mice received the LIMB implant and were injected intravenously with Qdots (red) prior to each LIMB imaging session to label the vasculature. Vessels were three-dimensionally imaged at increasing time resolution over the course of **a** weeks **b** days and **c** several hours. In line with our previous observations, we noted prominent changes in the vasculature, which continued over the whole monitoring time period, even after homeostasis is reached ($n = 5$ mice, two independent experiments, scale bar $= 50\,\mu m$). Small vessels continuously appear and disappear, larger vessels change their position and shape. The trace of such a larger vessel is displayed at all time points as a line in **c**. Blood vessels which can be used as landmarks are labeled by arrowheads and those that completely disappear within days are labeled by asterisks. **d** Overlap of the 3D projections of blood vessels in a mouse 35 days post-surgery (+0 h, green) and 24 h later (+24 h, red). A differential image between the two 3D images was generated. Blood vessel volume change was calculated by dividing the fraction of the volume difference between +24 h and 0 h (cyan areas in the middle panel indicate positive values, i.e., appearance of blood vessels; yellow areas indicate negative values, i.e., disappearance of blood vessels) by the total volume of the blood vessel at +24 h (delineated by white lines in the left panel) to obtain a normalized parameter of vessel volume change. The normalized volume changes (right panel) are dependent on the blood vessel diameter, with small vessels remodeling more rapidly than large vessels ($n = 6$ mice, scale bar $= 100\,\mu m$). **e** Similar to the observations in the deep femoral marrow, repeated imaging of blood vessels in calvarial bone and bone marrow also showed remodeling of the vasculature ($n = 3$ mice, two independent experiments). Scale bar $= 100\,\mu m$. Error bars represent s.d. values. Statistical analysis in **d** was performed using an ANOVA test (*$p < 0.05$; **$p < 0.01$; ***$p < 0.001$)

processes in the deep femoral marrow, repeatedly, over a time period of up to several months. The central marrow represents an area, which has been inaccessible to intravital multi-photon

imaging until now; our technique permits imaging of this tissue for the unprecedented duration of 4 months within the same bone marrow region. Importantly, this time period covers not
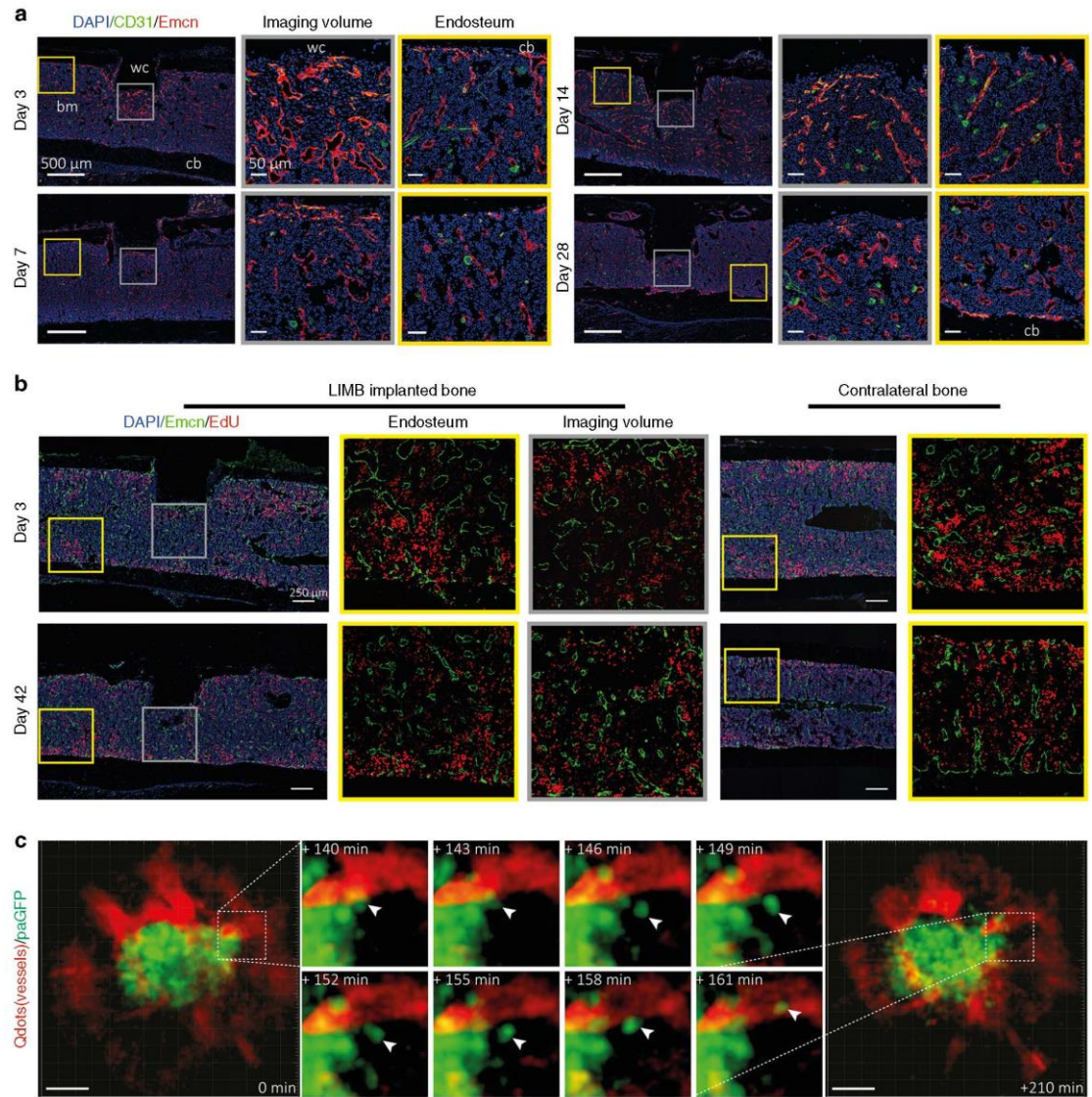

Fig. 7 LIMB and immunofluorescence analysis indicate possible mechanisms of vascular morphological changes deep in the femoral bone marrow, during regeneration, and in steady-state homeostasis. **a** Immunofluorescence analysis shows that type H vessels, characterized by $CD31^{hi}Emcn^{hi}$-expressing endothelial cells, are induced and present around the implant at day 3 after LIMB implantation. Their presence may vary individually but normalizes within 28 days post-surgery. Sinusoidal and type H vessel morphology adjacent to the wc is irregular in the first week and completely reorganizes to an appearance comparable to vessels found at endosteal areas distant from the injury site ($n = 3$ mice). bm bone marrow, cb cortical bone. Scale bar = 500 μm (left panels). **b** Immunofluorescence analysis after EdU pulse-chase experiments indicates similar EdU-uptake in the bone marrow of LIMB-implanted femurs and contralateral bones. Proliferating endothelial cells were rarely present at late time points after implantation. This result also supports the conclusion that 28 days after LIMB implantation both the bone and the bone marrow reach homeostasis ($n = 3$ mice in each cohort). **c** 3D fluorescence image ($300 \times 300 \times 66$ μm^3, left and right panel) acquired by LIMB 26 days post-surgery, in a *paGFP* mouse with the vasculature labeled by Qdots. Photoactivation was performed within a volume of $100 \times 100 \times 9$ μm^3 in the center of the image. The fluorescence image was acquired 2 h post activation. Scale bar = 50 μm. The middle panel shows time-lapse 3D images of the inset from the left panel, indicating that paGFP fluorescent cells outside the initial photoactivation volume are present 3 h after photoactivation and that they fluctuate in number and position within the tissue. Passive displacement of the relatively immobile stromal and vascular compartments by continuous proliferation and movement of hematopoietic cells is a possible mechanism of tissue and vascular re-localization during homeostasis (see Supplementary Movies 10, 11)

64

ARTICLE

only the bone healing phase, but also allows imaging during post-operative steady-state homeostasis, as demonstrated in this work.

As a microendoscopic approach, LIMB allows imaging of areas between 100 and 500 µm deep within bone marrow tissue, which are not accessible to existing intravital microscopy preparations. Whereas the maximum field of view of 280 µm in diameter and the spatial resolution are comparable to those achieved by the established longitudinal conventional intravital multi-photon microscopy, the imaging volume is fixed. This represents both a benefit, since the implant itself functions as a landmark for orientation in tissue, but also a limitation, since covering the relevant tissue areas can be more challenging than with other imaging methods.

Along that line, as we and others have previously shown[3], the deep bone marrow in diaphyseal regions does not show a supra-cellular compartmentalization, in contrast to secondary lymphoid organs, which are divided into zones that primarily host certain immune cell subtypes. In order to address tissue heterogeneity in the bone marrow, we developed various designs of our implant that allow positioning of the GRIN lens at various locations within the bone marrow, based on known anatomical compart-mentalization. Hence, LIMB allows the imaging of diaphyseal or metaphyseal areas as well as peri-cortical vs. deep-marrow regions, which are known to differ in their cellular composition. As we demonstrated by imaging sessile plasma cells (which are present in the bone marrow in frequencies of less than 1% of all hematopoietic cells), LIMB is suitable for the analysis of rare cells, despite the rather small field of view. This kind of analysis is crucial to improve our understanding of both hematopoiesis and immunological memory.

Upon fluorescently marking the lumina of blood vessels as a way to identify the same tissue regions in different imaging sessions[21, 31], we unexpectedly found the vasculature to be markedly dynamic during steady-state homeostasis. As compared to other tissues, the bone marrow is characterized by a much higher frequency of proliferating cells[3], and an additional level of dynamics is added by the motility of hematopoietic cells. There is a constant egress of cells[5], but cells can also enter the marrow tissue, as in the case of memory T cells or plasma blasts[34, 37]. Currently, our experiments using different strategies in order to label proliferating cells indicate that dynamics occurring in the non-vascular compartment may affect the positioning of the vessels rather than proliferation of the endothelial cells. Future studies based on LIMB analysis will show whether the observed dynamics are solely caused by a passive displacement of the vessels induced by proliferation or motility of bone marrow cells, or whether they are the result of an active process such as neovascularization, especially in light of recently published findings, which indicate that angiogenesis in the bone marrow mechanistically differs from other organs[38]. In any case, we expect that our results will have implications on our understanding of bone marrow microenvironment organization. They add complexity to the concept of how various tissue niches within the bone marrow are regulated. In the future we will investigate the impact of stromal network dynamics on the niches, since stromal cells may also contribute to the stability of those niches by acting as a scaffold in the tissue.

Concluding, LIMB is a unique method, which enables us to longitudinally analyze the same tissue areas in the deep bone marrow of individual mice by intravital multi-photon micro-scopy. Our technique will open up new ways for analyzing both long-term processes occurring with slow dynamics as well as short-term processes, characterized by fast cellular dynamics. LIMB can be applied to image any process occurring in the bone marrow, including regenerative processes, such as bone formation

in adaptation or after injury, as well as tumor formation and bone marrow metastasis, to name only a few examples.

Methods

Two-photon laser-scanning microscopy. Multi-photon fluorescence imaging experiments were performed using a specialized laser-scanning microscope based on a commercial scan head (TriMScope II, LaVision BioTec GmbH, Bielefeld, Germany). We used a 20× objective lens (IR-coating, NA 0.45, Olympus, Hamburg, Germany) combined with GRIN lenses (Fig. 1, GRINTech GmbH, Jena, Germany) to focus the excitation laser radiation into the sample and to collect the emitted fluorescence. Detection of the fluorescence signals was accomplished with photomultiplier tubes in the ranges of (466 ± 20) nm, (525 ± 25) nm, (593 ± 20) nm, and (655 ± 20) nm. paGPP was photoactivated at 840 nm. Both, activated paGPP and GPP were excited at 940 nm and detected at (525 ± 25) nm. eYPP (Prx-1:YFP mice) was excited at 940 nm and detected at (525 ± 20) nm and (593 ± 20) nm, while tdRPP was excited at 1100 nm and detected at (593 ± 20) nm. Blood vessels were labeled with Qdots excited at 940 or 1100 nm and detected at (593 ± 20) nm. In all imaging experiments we used an average maximum laser power of 10 mW to avoid photodamage, at a typical pixel dwell time of 2 µs. The maximum peak photon flux was 10^{29} photons cm^{-2} s^{-1}, in accordance to the values measured using conventional two-photon microscopy. The acquisition time for an image with a field of view of 150×150 µm^2 and a digital resolution of 497×497 pixel was 800 ms, as well as for a field of view of 350×350 µm^2 and a digital resolution of 507×507 pixel. We acquired 70 µm z-stacks (z-step size 6 µm) each 30 s over a total time course of typically 45 min. Calvarial and tibial imaging were performed using the same microscope setup. In contrast to LIMB, we used a 20× water-immersion objective for focusing (IR coated, NA 0.95, Olympus, Hamburg, Germany).

Data analysis. Image segmentation and tracking of all cells was performed using segmentation, object-recognition, and tracking plugins in Imaris (Bitplane AG, Zurich, Switzerland). Cell tracks that were present in the field of view for more than 10 recorded time points (i.e., 5 min) were included in the analysis. Statistical analysis of the data was performed using Prism (Graph Pad Software Inc., San Diego, USA).

Mice. All mice used were on a C57/Bl6J background. C19:tdRFP fate mapping mice were generated in our lab by crossing CD19:Cre[28] onto ROSA26:tdRFP[29] mice. Prx-1:Cre mice[30] were crossed onto ROSA26:eYFP mice (Prx-1:YFP). Photoactivatable GPP (paGFP) mice, which ubiquitously express paGPP[18], were kindly provided by Prof. M. Nussenzweig. CX₃CR1:GFP mice express EGPP in monocytes, dendritic cells, NK cells, and brain microglia under control of the endogenous cx3cr1 locus[39]. All mice were bred in the animal facility of the DRFZ. All animal experiments were approved by Landesamt für Gesundheit und Soziales, Berlin, Germany, in accordance with institutional, state, and federal guidelines.

Surgical preparation for longitudinal intravital imaging. We used a lateral approach to expose the femoral shaft of the right hind limb of mice anaesthetized with 1.5–2.0% isoflurane. Initially, an incision of ~1.5 cm was made into the shaved and disinfected skin between the knee and hip joint, parallel to the femur. The underlying muscles were dissected and retracted along the delimiting fascia. Then, a 0.65 mm pilot hole in the distal half of the diaphysis was drilled through the cortex using an electric precision drill (FBS 240/E Proxxon GmbH, Foehren, Germany) mounted on a stand to ensure minimal damage to the underlying bone marrow tissue. Ring forceps were applied to fix the bone in position. We placed the TiCP grade 4 implant parallel onto the femoral shaft and drilled the other two pilot holes (0.31 mm) for the bicortical screws manually through the complete shaft. Here, the holes in the implant act as drill templates. When fully inserted, the bone screws lock in the fixation plate, and thus prevent any movement or rotation. The wound was frequently washed during surgery with sterile NaCl solution and sewed with an absorbable surgical thread (Surgicryl Rapid PGA, USP 6-0, SMI, St. Vith, Belgium). Finally, we attached the reference plate. All animals were kept on a temperature-controlled heating device throughout the surgery (Supplementary Fig. 2). For longitudinal calvarial imaging we used a permanent window glued with bone cement onto the calvarial bone, leaving a circular window freely accessible[40]. The window glass was supported by a customized metal ring kindly provided by Dr. Rinnenthal, J.-L. (Charite—Universitätsmedizin, Berlin, Germany).

Clinical scoring system. Total clinical scoring post-surgery was based on behavior and appearance of the individual mice. The total clinical score represents the sum of eight factors (physical appearance, state of mucosae, motoric ability, wound healing, body weight loss, food and water consumption, response to provocation) rated on a scale of 0–3. No animal was scored to a total clinical score higher than 4.

Histochemistry. Femurs were fixed in 4% paraformaldehyde and transferred to 10–30% sucrose/PBS for cryoprotection. Fixed bone sample and implant were covered with Kawamoto's medium (SCEM, Section-Lab Co. Ltd., Hiroshima, Japan) in order to avoid air bubbles during separation. Bones were frozen and cryo-

ARTICLE

sectioned using Kawamoto's film method[41]. Movat's pentachrome stainings were performed on 7 μm sections[42]. Brightfield images were generated by three-dimensional tile scanning on a Biorevo (BZ-9000, Keyence GmbH, Neu Isenburg, Germany) using the BZ-II Viewer with a 10×, NA 0.45 (air) objective lens. Images were stitched using BZ-II Analyzer and processed with Fiji software.

Fluorescence microscopy. Bones were fixed and sectioned as described above. Sections of 7 μm were blocked with 5% PCS/PBS for 30 min and stained with antibodies in 5% PCS/PBS/0.1% Tween for 1–2 h at room temperature: CD45 (1:100, ThermoFisher eBioscience, Frankfurt, Germany, 30-F11), Sca-1-APC (1:200, eBioscience, 17-5981-82), Laminin (1:200, Sigma-Aldrich, Taufkirchen, Germany, L9393), c-kit-PE (1:100, 130-102-542, Miltenyi, Bergisch Gladbach, Germany), Ki-67-bio (1:100, eBioscience, 14-5698-82), Endomucin (1:100, Santa Cruz, sc-65495), CD31-A488 (1:100, R&D Systems, FAB3628G). Sections were washed with PBS/0.1% Tween three times and incubated with secondary Abs (LifeSciences-Sigma-Aldrich, Taufkirchen, Germany) for 1 h at room temperature. Nuclei were stained with 1 μg ml^{-1} DAPI (Sigma-Aldrich) in PBS and mounted with Fluorescent Mounting Medium (DAKO, Hamburg, Germany). Overview images were generated by three-dimensional tile scanning on a LSM710 (Carl Zeiss MicroImaging, Jena, Germany) using Zen 2011 software, with either a 10×, NA 0.3 (air) objective lens for complete femoral bone marrow sections, or a 20×, NA 0.5 (air) objective lens for partial scans (implant area, distal bone). Maximum intensity projection images and stitched overviews were created using Zen 2011 and processed with Fiji. For tracking of CMTPX-labeled transferred cells, splenocytes were isolated and incubated with CellTracker Red CMTPX, according to the manufacturer's protocol (ThermoFisher, Frankfurt, Germany). 1×10^6 splenocytes were transferred to recipient mice. Bones were harvested 4 h after transplantation and femurs were processed as described in the immunofluorescence method section. Sections were stained with DAPI and fluorescent images were generated by three-dimensional tile scanning on a Biorevo (BZ-9000, Keyence GmbH, Neu Isenburg, Germany) using BZ-II Viewer with a 10×, NA 0.45 (dry) objective lens. Images were stitched using BZ-II Analyzer and processed with Fiji software.

EdU labeling and staining. Proliferating cells were labeled using EdU at 1.6 mg kg^{-1} mouse weight injected in PBS intraperitoneally 2 h before sacrifice[7]. Femoral bone sections were stained using the Click-iT EdU Alexa Fluor 647 kit (LifeSciences-Sigma-Aldrich, Taufkirchen, Germany), according to the manufacturer's protocol.

Flow cytometry. Diaphyseal ends including growth plate and secondary ossification centers of femurs were cut off and discarded. An 18 gauge needle was inserted into the distal end of the long bone and the bone marrow was thoroughly flushed out with 5 ml of cold (4°C) MACS buffer (0.5% BSA, 2 mM EDTA in PBS). LIMB implants were removed after flushing. Cells were re-suspended, filtered with a 50 μm cell strainer, spun down 6 min at 75 × g, and re-suspended in an erythrocyte lysis buffer. After washing, FcR were blocked using antibodies against CD16/32 (DRPZ in house clone 2.4G2, 5 μg ml^{-1}) and stained with antibodies on ice for 40 min. After washing the cells were acquired with a FACSymphony (BD Bioscience, Heidelberg, Germany) system and populations analyzed in FlowJo10. Cell counts were performed on $n = 6$ individuals. Live lymphocytes were divided into the following populations: progenitors: LSK cell (lin$^-$sca1$^+$ckit$^+$), long-term hematopoietic stem cell (LT HSC, lin-sca1$^+$ckit$^+$CD150$^+$CD48$^-$), short-term HSC (ST HSC, lin$^-$sca1$^+$ckit$^+$CD150$^+$CD48$^+$), multi-potent progenitor (MPP, lin$^-$sca1$^+$ckit $^+$CD150$^-$CD48$^+$), common lymphoid progenitor (CLP, LSK$^-$IL7R$^+$Flk2$^+$), common myeloid progenitor (CMP, lin$^-$sca1$^-$ckit$^+$CD34$^+$CD16/32$^-$), megakaryocyte-erythroid progenitor (MEP, lin$^-$sca1$^-$ckit$^+$ CD34$^-$CD16/32$^-$) and granulocyte-macrophage progenitor (GMP, lin$^-$sca1$^-$ckit$^+$CD34$^+$CD16/32$^+$), dendritic cell progenitor (DCP, lin$^-$sca1$^-$Flk2$^+$IL7R$^+$) B cells: propreB (B220$^+$CD19$^-$ckit$^+$Flk2$^+$), preBI (B220$^+$CD19$^+$ckit$^+$), preBII (B220$^+$CD19$^+$ckit$^-$IgM$^-$CD25$^+$), immature B cells (B220$^+$CD19$^+$ckit$^-$IgM$^+$IgD$^-$), mature B cells (B220$^+$CD19$^+$ckit$^+$IgM$^+$IgD$^+$), plasma cells (CD138high) T cells CD4 T cells (CD3$^+$CD4$^+$), CD8 T cells (CD3 $^+$CD8$^+$) innate immune cells: natural killer cells (NK cells, NK1.1$^+$), granulocytes (CD11b$^+$Gr1$^+$), monocytes/macrophages (CD11b$^+$Gr1$^-$), dendritic cells (DCs, CD11c$^+$). Antibodies used: CD19-FITC (1:800, BioLegend, Pell, Germany, 115506), B220-FITC (1:800, BioLegend 103206), Gr1-FITC (1:800, BioLegend 108406), CD3-FITC (1:800, BioLegend 100204), CD11b-FITC (1:800, BioLegend 101206), Ter119-FITC (1:800, BioLegend 116206), IL7R-Pe-Cy7 (1:100, BioLegend 135014), B220-BV510 (1:400, BioLegend 103247), CD34-A647 (1:200, eBioscience 51-0341-82), CD16/32-A450 (1:800, eBioscience 48-0161-82), sca1-APC-Cy7 (1:400, BioLegend 108126), Plk2-Pe (1:100, BioLegend 135306), CD19-BV650 (1:400, BioLegend 115541), ckit-A700 (1:200, eBioscience 56-1172-82), c-fms-APC (1:200, eBioscience 17-1152-82), ckit-APC (1:200, BioLegend 135108), CD150-Pe (1:800, BioLegend 115904), CD48-Pe-Cy7 (1:800, BioLegend 560731), sca1-A700 (1:200, eBioscience 56-5981-82), CD138-BV421 (1:800, BioLegend 142508), IgM-APC (1:400, BioLegend 406509), CD25-APC-Cy7 (1:400, BioLegend 102026), IgD-A488 (0.7 μg ml^{-1}, in house, clone 11.26c), CD4-Pe-Cy7 (1:800, eBioscience 25-0042-82), CD8-APC (1:800, BioLegend 100712), CD3-APC-Cy7 (1:200, eBioscience 47-0031-82), CD11c-FITC (1:800, BioLegend 117306), NK1.1-Pe (1:800, BioLegend

108707), Gr1-PB (1:800, BioLegend 108429), CD11b-A700 (1:800, eBioscience 56-0112-82).

Mouse activity analysis. Analysis of mouse activity and motility was performed using radio-frequency identification (RFID) technology to identify and track individual mice within a cage. Animals were subcutaneously tagged with bio-compatible glass-encapsulated RFID transponders (EURO I.D., Frechen, Germany) and were detected by a 2 × 4 sensor plate system (Phenosys, Berlin, Germany) underneath the cage. The frequency of crossed sensors serves as an approximate activity measure. Physical activity was normalized to the mean value of activity measured over 3 days before surgery. Before that, mice had been placed in the cage for at least 2 days. The relative change in activity for each mouse is displayed. For sham treatment, animals were put under anesthesia.

Ex vivo μCT. Femoral bones were harvested and fixed as described above. Fixed bones were measured in 20–30% sucrose solution using the vivaCT 40 (Scanco Medical AG, Bruettisellen, Switzerland). Scans were performed with 70 kVp and an isotropic voxel size of 10.5 μm. Reconstructed scans were converted into tiff-stacks for further data analysis. Bone morphological measurements from μCT 3D reconstructions were performed using the intensity. For bone thickness under the fixation plate and on the opposite site of the bone, areas were chosen as shown in Fig. 2e. For each position, the intensity profile was approximated with two Gaussian curves. The width of each Gaussian curve was considered to represent bone thickness at the respective position. For intact contralateral femurs, we performed the same measurements choosing a mirrored position of the bone to account for the fact that the LIMB femurs are always right femurs and the contralateral bones are left femurs.

Data availability. All relevant data are saved on the institutional servers. The data that support the findings of this study are available from the corresponding authors upon reasonable request.

References

1. Ramasamy, S. K. et al. Regulation of hematopoiesis and osteogenesis by blood vessel-derived signals. *Annu. Rev. Cell Dev. Biol.* **32**, 649–675 (2016).
2. Tokoyoda, K., Hauser, A. E., Nakayama, T. & Radbruch, A. Organization of immunological memory by bone marrow stroma. *Nat. Rev. Immunol.* **10**, 193–200 (2010).
3. Zehentmeier, S. et al. Static and dynamic components synergize to form a stable survival niche for bone marrow plasma cells. *Eur. J. Immunol.* **44**, 2306–2317 (2014).
4. Roth, K. et al. Tracking plasma cell differentiation and survival. *Cytometry A* **85**, 15–24 (2014).
5. Beck, T. C., Gomes, A. C., Cyster, J. G. & Pereira, J. P. CXCR4 and a cell-extrinsic mechanism control immature B lymphocyte egress from bone marrow. *J. Exp. Med.* **211**, 2567–2581 (2014).
6. Itkin, T. et al. Distinct bone marrow blood vessels differentially regulate haematopoiesis. *Nature* **532**, 323–328 (2016).
7. Kusumbe, A. P., Ramasamy, S. K. & Adams, R. H. Coupling of angiogenesis and osteogenesis by a specific vessel subtype in bone. *Nature* **507**, 323–328 (2014).
8. Junt, T. et al. Dynamic visualization of thrombopoiesis within bone marrow. *Science* **317**, 1767–1770 (2007).
9. Kohler, A. et al. G-CSF-mediated thrombopoietin release triggers neutrophil motility and mobilization from bone marrow via induction of Cxcr2 ligands. *Blood* **117**, 4349–4357 (2011).
10. Mazo, I. B. et al. Bone marrow is a major reservoir and site of recruitment for central memory CD8+ T cells. *Immunity* **22**, 259–270 (2005).
11. Mazo, I. B. & von Andrian, U. H. Adhesion and homing of blood-borne cells in bone marrow microvessels. *J. Leukoc. Biol.* **66**, 25–32 (1999).
12. Lo Celso, C., Lin, C. P. & Scadden, D. T. In vivo imaging of transplanted hematopoietic stem and progenitor cells in mouse calvarium bone marrow. *Nat. Protoc.* **6**, 1–14 (2011).
13. Wu, J. W., Runnels, J. M. & Lin, C. P. Intravital imaging of hematopoietic stem cells in the mouse skull. *Methods Mol. Biol.* **1185**, 247–265 (2014).
14. Kohler, A. et al. Altered cellular dynamics and endosteal location of aged early hematopoietic progenitor cells revealed by time-lapse intravital imaging in long bones. *Blood* **114**, 290–298 (2009).
15. Chen, Y., Maeda, A., Bu, J. & DaCosta, R. Femur window chamber model for in vivo cell tracking in the murine bone marrow. *J. Vis. Exp.* **113**, e54205 (2016).

ARTICLE

16. Kim, S., Lin, L., Brown, G. A., Hosaka, K. & Scott, E. W. Extended time-lapse in vivo imaging of tibia bone marrow to visualize dynamic hematopoietic stem cell engraftment. *Leukemia* **31**, 1582-1592 (2017).
17. Park, D. et al. Endogenous bone marrow MSCs are dynamic, fate-restricted participants in bone maintenance and regeneration. *Cell Stem Cell* **10**, 259–272 (2012).
18. Hawkins, E. D. et al. T-cell acute leukaemia exhibits dynamic interactions with bone marrow microenvironments. *Nature* **538**, 518–522 (2016).
19. Trachtenberg, J. T. et al. Long-term in vivo imaging of experience-dependent synaptic plasticity in adult cortex. *Nature* **420**, 788–794 (2002).
20. Farrar, M. J., Wise, F. W., Fetcho, J. R. & Schaffer, C. B. In vivo imaging of myelin in the vertebrate central nervous system using third harmonic generation microscopy. *Biophys. J.* **100**, 1362–1371 (2011).
21. Barretto, R. P. et al. Time-lapse imaging of disease progression in deep brain areas using fluorescence microendoscopy. *Nat. Med.* **17**, 223–228 (2011).
22. Lewandowski, D. et al. In vivo cellular imaging pinpoints the role of reactive oxygen species in the early steps of adult hematopoietic reconstitution. *Blood* **115**, 443–452 (2010).
23. Matthys, R. & Perren, S. M. Internal fixator for use in the mouse. *Injury* **40**, S103–S109 (2009).
24. Perren, S. M. Evolution of the internal fixation of long bone fractures. The scientific basis of biological internal fixation: choosing a new balance between stability and biology. *J. Bone Joint Surg. Br.* **84**, 1093–1110 (2002).
25. Gerber, C., Mast, J. W. & Ganz, R. Biological internal fixation of fractures. *Arch. Orthop. Trauma Surg.* **109**, 295–303 (1990).
26. Perren S. M., Cordey J., Rahn B. A., Gautier E. & Schneider E. Early temporary porosis of bone induced by internal fixation implants. A reaction to necrosis, not to stress protection? *Clin. Orthop. Relat. Res.* **232**, 139–151 (1988).
27. Hyldahl, C., Pearson, S., Tepic, S. & Perren, S. M. Induction and prevention of pin loosening in external fixation: an in vivo study on sheep tibiae. *J. Orthop. Trauma* **5**, 485–492 (1991).
28. Victora, G. D. et al. Germinal center dynamics revealed by multiphoton microscopy with a photoactivatable fluorescent reporter. *Cell* **143**, 592–605 (2010).
29. Kusumbe, A. P. et al. Age-dependent modulation of vascular niches for haematopoietic stem cells. *Nature* **532**, 380–384 (2016).
30. Bremer, D. et al. Longitudinal intravital imaging of the retina reveals long-term dynamics of immune infiltration and its effects on the glial network in experimental autoimmune uveoretinitis, without evident signs of neuronal dysfunction in the ganglion cell layer. *Front. Immunol.* **7**, 642 (2016).
31. Gibson, V. B. et al. A novel method to allow noninvasive, longitudinal imaging of the murine immune system in vivo. *Blood* **119**, 2545–2551 (2012).
32. Sapoznikov, A. et al. Perivascular clusters of dendritic cells provide critical survival signals to B cells in bone marrow niches. *Nat. Immunol.* **9**, 388–395 (2008).
33. Cariappa, A. et al. Perisinusoidal B cells in the bone marrow participate in T-independent responses to blood-borne microbes. *Immunity* **23**, 397–407 (2005).
34. Tokoyoda, K. et al. Professional memory CD4+ T lymphocytes preferentially reside and rest in the bone marrow. *Immunity* **30**, 721–730 (2009).
35. Sercan Alp, O. et al. Memory CD8(+) T cells colocalize with IL-7(+) stromal cells in bone marrow and rest in terms of proliferation and transcription. *Eur. J. Immunol.* **45**, 975–987 (2015).
36. Tokoyoda, K., Egawa, T., Sugiyama, T., Choi, B. I. & Nagasawa, T. Cellular niches controlling B lymphocyte behavior within bone marrow during development. *Immunity* **20**, 707–718 (2004).
37. Hauser, A. E. et al. Chemotactic responsiveness toward ligands for CXCR3 and CXCR4 is regulated on plasma blasts during the time course of a memory immune response. *J. Immunol.* **169**, 1277–1282 (2002).
38. Ramasamy, S. K., Kusumbe, A. P., Wang, L. & Adams, R. H. Endothelial Notch activity promotes angiogenesis and osteogenesis in bone. *Nature* **507**, 376–380 (2014).
39. Jung, S. et al. Analysis of fractalkine receptor CX(3)CR1 function by targeted deletion and green fluorescent protein reporter gene insertion. *Mol. Cell Biol.* **20**, 4106–4114 (2000).
40. Fuhrmann, M., Mitteregger, G., Kretzschmar, H. & Herms, J. Dendritic pathology in prion disease starts at the synaptic spine. *J. Neurosci.* **27**, 6224–6233 (2007).
41. Kawamoto, T. Use of a new adhesive film for the preparation of multi-purpose fresh-frozen sections from hard tissues, whole-animals, insects and plants. *Arch. Histol. Cytol.* **66**, 123–143 (2003).
42. Movat, H. Z. Demonstration of all connective tissue elements in a single section; pentachrome stains. *AMA Arch. Pathol.* **60**, 289–295 (1955).

Author contributions
R.A.N., A.E.H., D.R. and J.S. designed the study, analyzed data and interpreted results. R.A.N., A.E.H., D.R., J.S., R.G., G.P., A.R. and S.Z. performed experiments. R.M., R.N., K.S.-B. and G.D. provided expertise for the implant design, surgery and Movat's pentachrome histochemical staining. F.M. provided expertise in the analysis of HSCs subsets frequencies and interpretation of these data with respect to the characterization of post-surgical homeostasis. Y.W., H.-D.C. and S.N. helped with mouse activity analysis. R.A.N. and A.E.H. wrote the manuscript.

Additional information
Supplementary Information accompanies this paper at https://doi.org/10.1038/s41467-017-01538-9.

Competing interests: R.M. and R.N. (RISystem AG, Davos, Switzerland) declare competing financial interests. The implant for longitudinal imaging will be commercialized by RISystem AG, Davos, Switzerland. The remaining authors declare no competing financial interests.
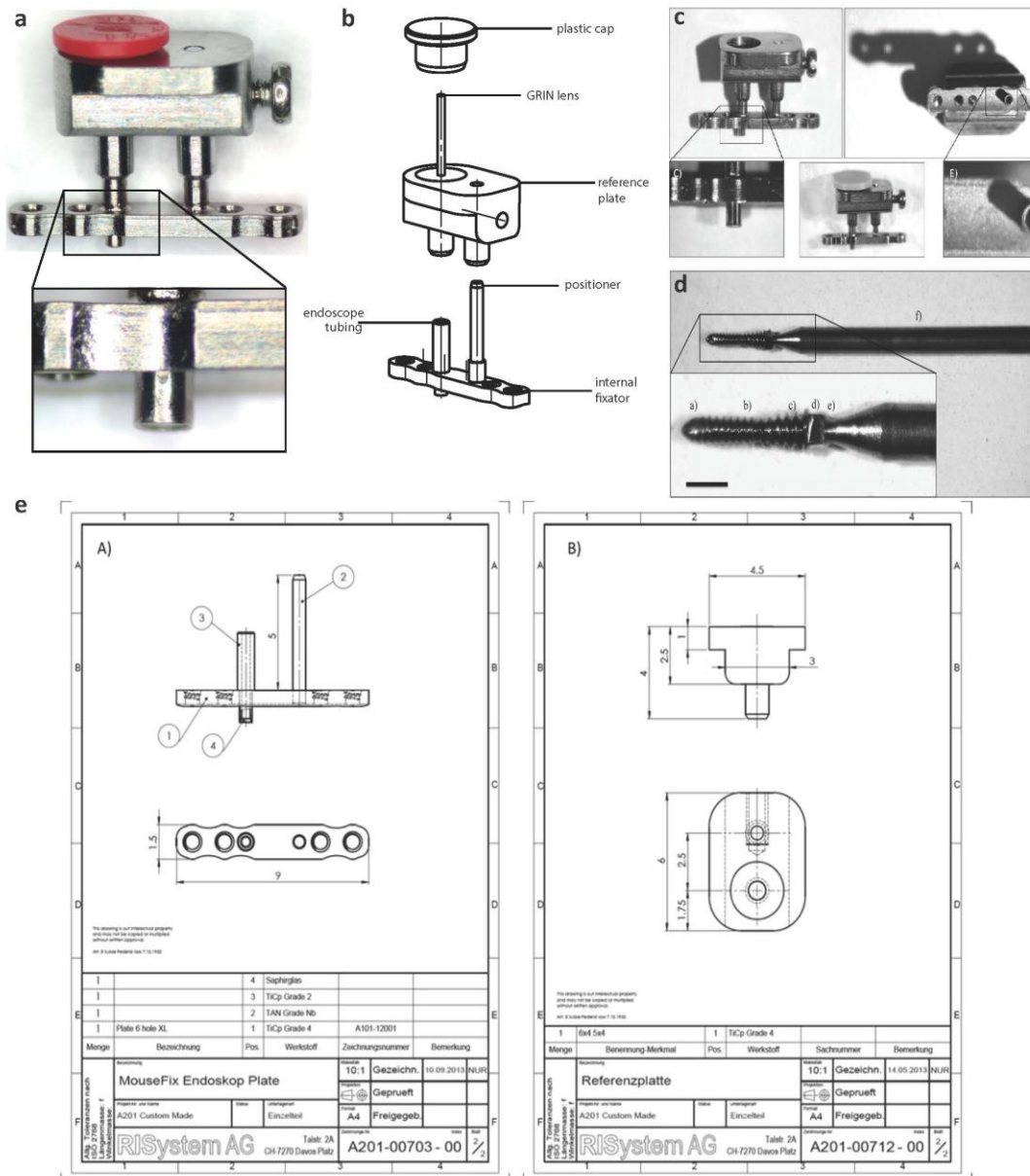
Reprints and permission information is available online at http://npg.nature.com/reprintsandpermissions/

Publisher's note: Springer Nature remains neutral with regard to jurisdictional claims in published maps and institutional affiliations.

**Supplementary Figure 1 |** Assembly and technical specifications of the LIMB microendoscope implant. (**a**) The titanium alloy (medical grade) implant consists of two parts that are assembled at the end of the surgery. The extracorporeal reference plate is attached to the positioner and the endoscope tubing and fixed with a screw (M1x2). (**b**) Exploded assembly drawing of the LIMB setup. The plastic cap prevents the endoscope from dust and smaller particles of the cage bedding. The GRIN lens is fit into the endoscope tubing. The endoscope tubing has an inner diameter of 450 µm and an outer diameter of 650 µm. Both, endoscope tubing and positioner, are micro-welded to the internal fixator. (**c**) The sapphire window (d = 500 µm), which seals the tubing at the intramedullary end, is pressed into a recess (right inset). The outer tip ends in the conical recess of the reference plate (left inset) and can be accessed by the microscope objective, when the plastic cap is removed. The reference plate is used for the alignment of the GRIN lens with respect to the microscope objective. It holds the implant and the femur in a stable position under a customized imaging stage (Supplementary Figure 2). (**d**) The bicortical screw (RISystem, Davos, Switzerland) has two different threads b) and c), whereas b) locks into the bone and c) into the fixator plate. d) is the square box wrench for removal of the screw and e) the predetermined breaking point to shear off the shaft f) from the screw at a defined torque. All implanted materials can be autoclaved and are resistant to organic solvents. (**e**) Technical drawings of both parts with relevant dimensioning.
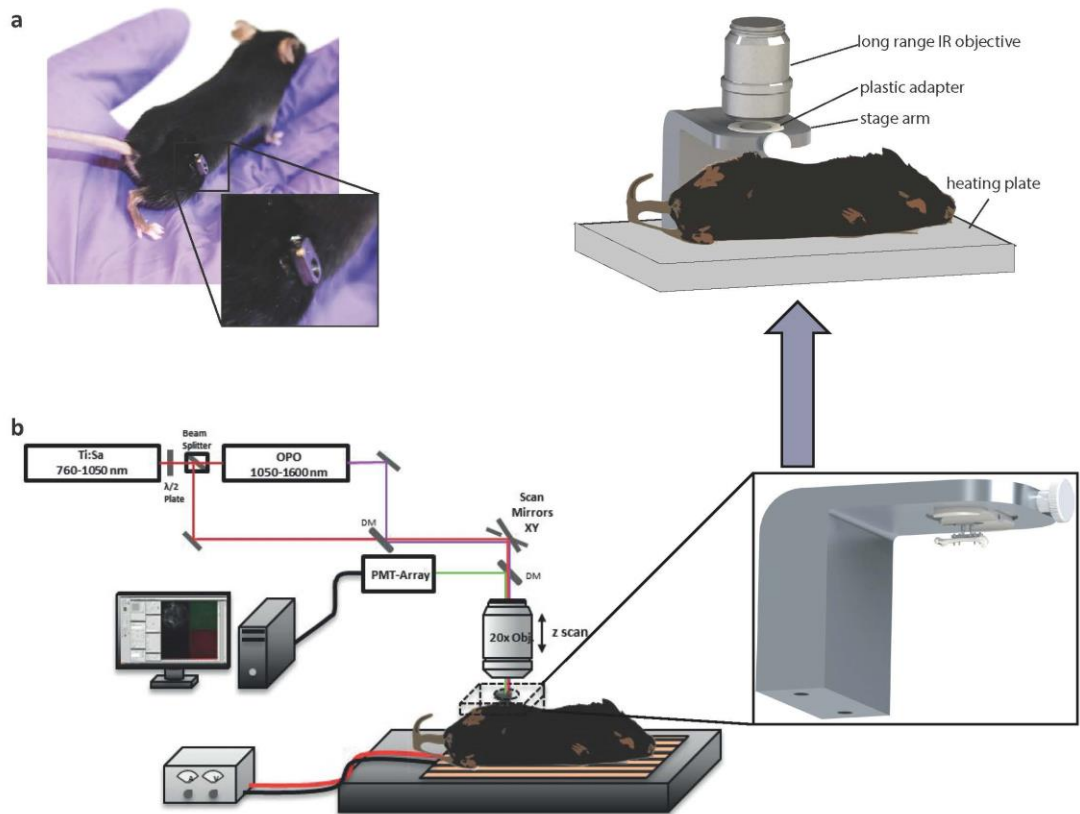
Supplementary Figure 2 | Microscope setup for longitudinal intravital imaging of the bone marrow in mice. (**a**) Photograph of a mouse carrying the LIMB implant 28 days post-surgery. Externally, only the reference plate is visible (inset). (**b**) The mouse is positioned under the two-photon microscope using a customized plastic adapter and stage, so that the GRIN lens is aligned parallel to the optical axis of the microscope objective lens for optimal illumination of the bone marrow tissue. During time lapse image acquisition the animals lay on a controlled heating plate to maintain a constant body temperature.
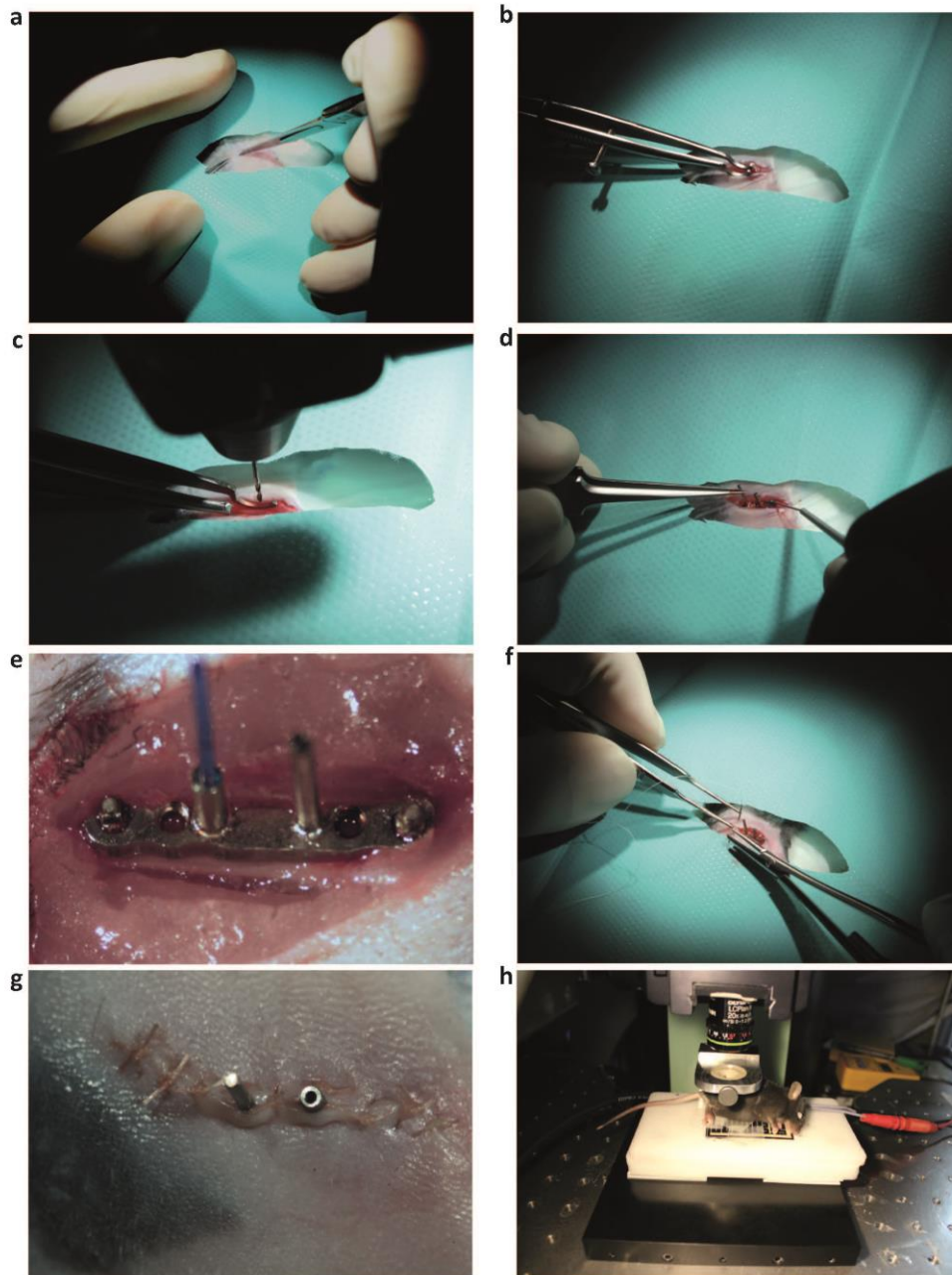
Supplementary Figure 3 | Surgical procedure for implantation of the LIMB-implant. (**a**) A surgical incision is placed into the shaved and disinfected skin between the knee and hip joint, parallel to the femur in order to expose the femoral shaft of the right hind limb. (**b**) A ring forceps is used to fixate the bone. (**c**) For drilling of the pilot hole in the distal half of the diaphysis an electric precision drill and a stand is used. (**d**) The LIMB implant system is placed parallel onto the femur and (**e**) bicortical screws are inserted to complete the fixation. (**f**) The wound was closed with a absorbable surgical thread. In (**g**) the implant after wound closure and before attachment of the reference plate is shown. (**h**) Anesthetized mouse under the two-photon microscope.
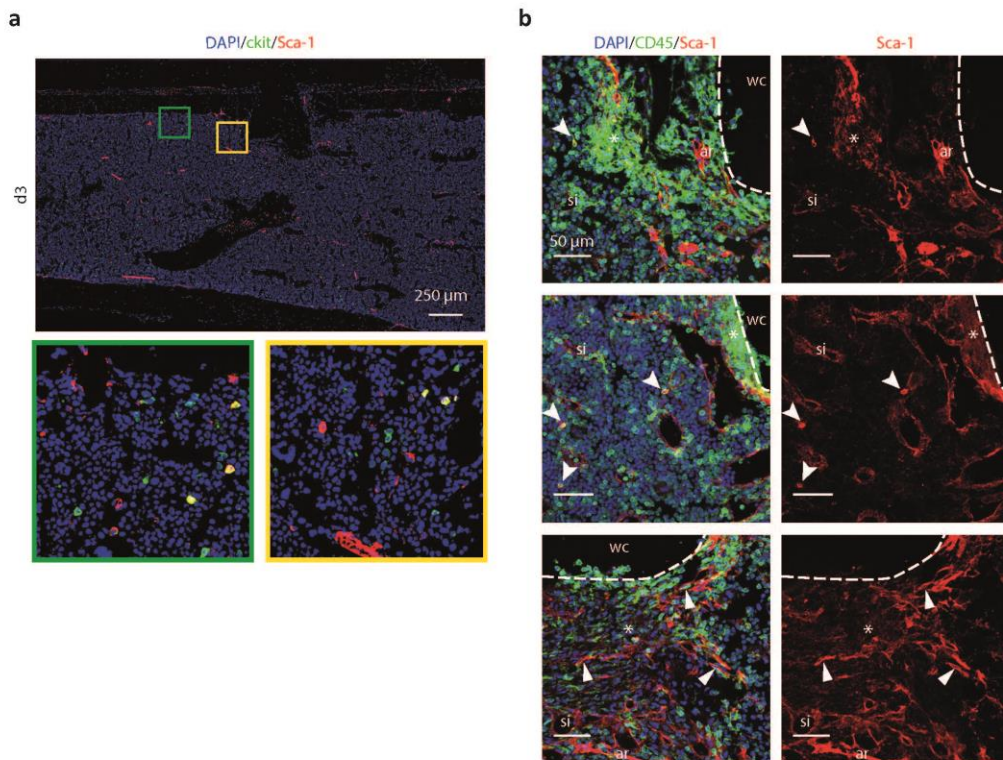
Supplementary Figure 4 | Immunofluorescence analysis early post-surgery. (**a**) Immunofluorescence staining for ckit+sca1+ cells (yellow) shows presence of this HSPC enriched population in endosteal areas and adjacent to the implant window as early as 3 days post-surgery indicating the maintenance of hematopoietic precursor retention in the presence of the LIMB implant (**b**) The tissue adjacent to the window cavity (wc) after removal of the implant displays CD45+ cell (green) accumulations 3 days post-surgery with predominantly rounded nuclei and areas of dim Sca-1 expression (asterisks). Sca-1hi arteriolar endothelial cells with elongated nuclei (triangles) spread into the damaged tissue indicating vascularization. Some cells are Sca1+CD45+ (arrow heads), and might represent hematopoietic precursors. Sinusoids, si; arterioles, ar.
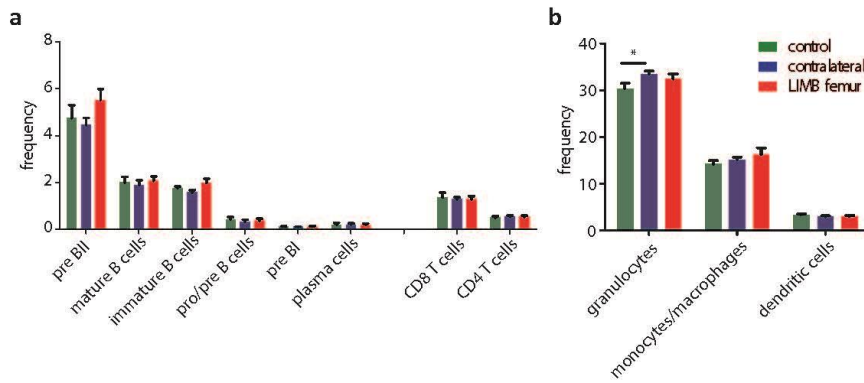
Supplementary Figure 5 | Flow cytometric analysis demonstrates that LIMB has no effect on bone marrow cell populations. Flow cytometry analysis of femurs with the LIMB implant, their contralateral femurs and femurs of control mice. Similar frequencies and cell counts of various leukocyte populations indicate no effect of the presence of the LIMB implant on bone marrow cell composition for (**a**) B and T cell populations and (**b**) innate immune cells. (error bars represent s.e.m., statistical analysis: t-test, * - p = 0.0318, n = 8 LIMB-implanted mice, n = 8 control mice, two independent experiments).
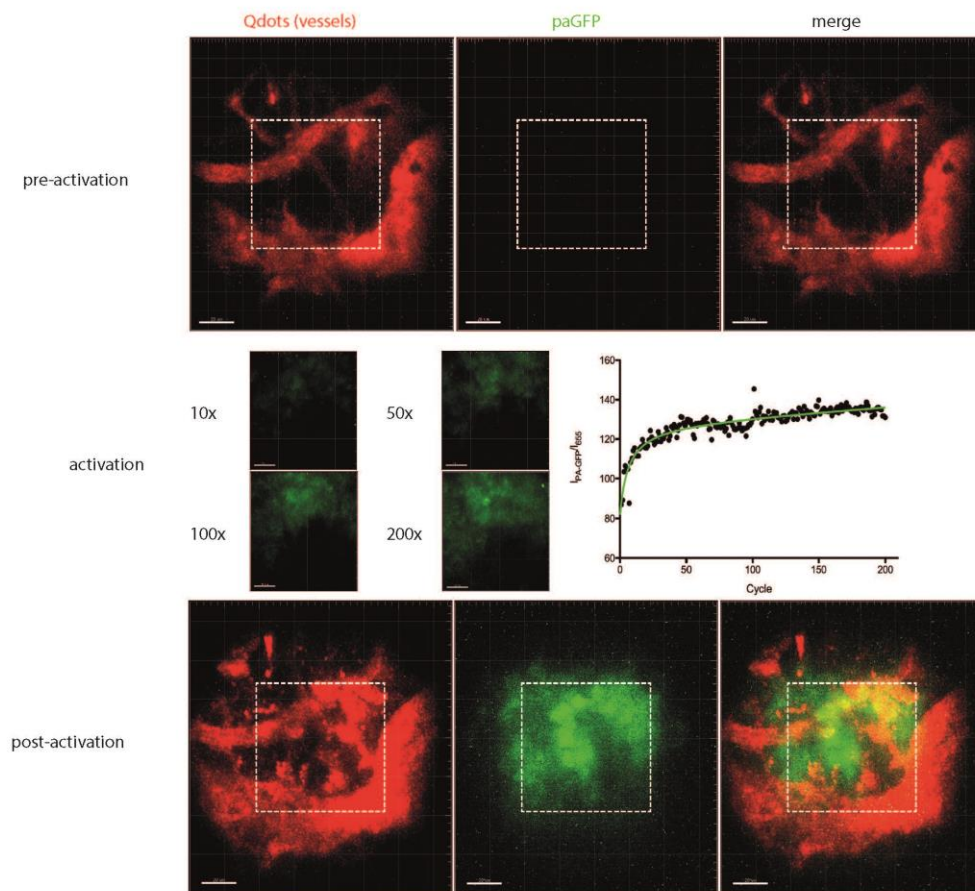
Supplementary Figure 6 | Photoactivation in the bone marrow of paGFP mice using LIMB. Mice ubiquitously expressing paGFP received the LIMB implant and were injected prior to the imaging session with Qdots to label the vasculature. In the course of a photoactivation experiment, first, the pre-activation state of the tissue in the volume-of-view was recorded (upper panel). The vessels were clearly visible but no signal above background was recorded in the paGFP-channel at an excitation wavelength of 940 nm. For photoactivation, the excitation wavelength was tuned to 840 nm and the scanning volume (x, y, z) was reduced from 150x150x30 μm³ to 75x75x30 μm³ (step size 3 μm each) or from 300x300x70 μm³ to 100x100x9 μm³ (step size 3 μm each). During the 200 activation cycles over the time course of 40 min, we recorded the fluorescence signals from the Qdots (vessels) and paGFP as shown in the middle panel. The increase in fluorescence intensity of paGFP (I_{PA-GFP}) normalized to the fluorescence intensity of the vessels (I_{655}) over the number of activation cycles is given in the graph. For multi-photon image acquisition post-activation the excitation wavelength was tuned back to 940 nm and the volume-of-view increased. The same channels were used to record again a 150x150x30 μm³ volume, which clearly shows the activated paGFP inside the cells (lower panel). Scale bar = 20 μm in the upper and lower panel, scale bar = 15 μm in the middle panel.
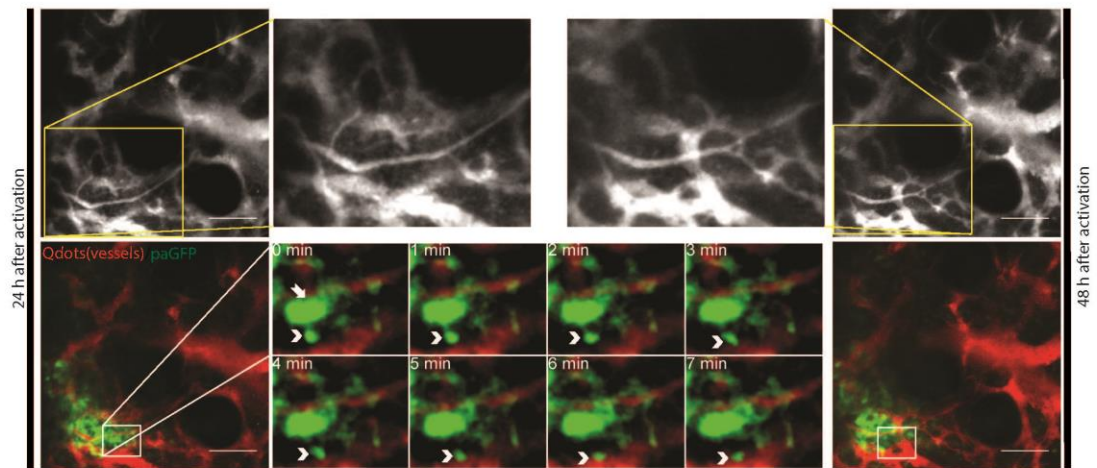
Supplementary Figure 7 | Similar motility patterns of hematopoietic cells in the calvarial bone marrow after photoactivation as compared to the femoral bone marrow. The photoactivation was performed within a volume of a 150x150x9 μm³ region within the 500x500x66 μm³ field of view. The fluorescence images were longitudinally acquired 24 h and 48 h after activation. The upper panel shows the vessel network in the calvarial bone and bone marrow (gray) 24 h after activation and 48 h after activation with enlarged inserts demonstrating changes in the vasculature within one day. The lower panel shows vessels in red and activated paGFP in green. The lower middle panel shows time-lapse 3D images of the inset in the left panel, indicating paGFP fluorescent cells migrate out of the initial photoactivation volume 24 h after photoactivation. They are fluctuating in number and position within the tissue within short periods of time (7 min). Scale bars = 100 μm.
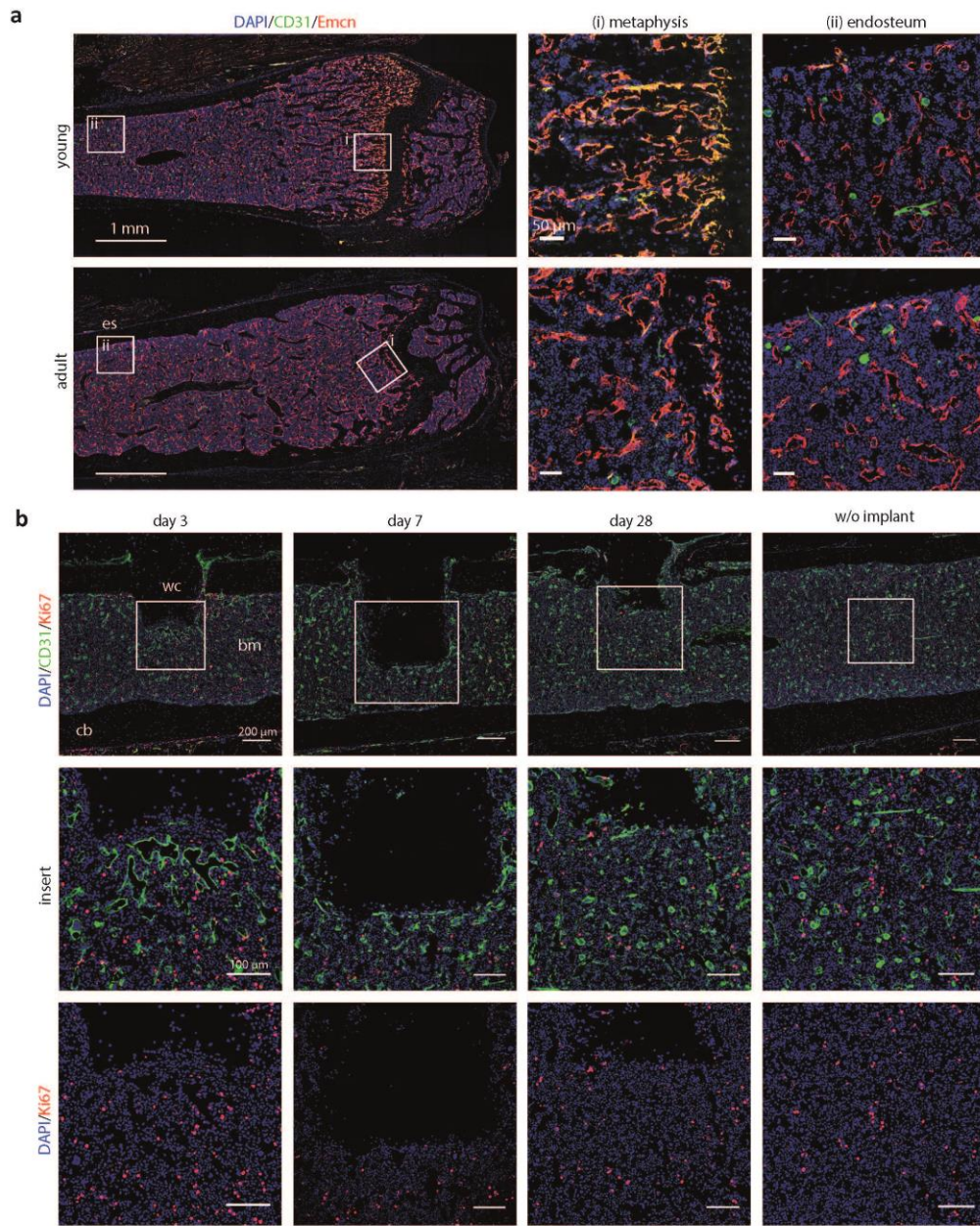
Supplementary Figure 8 | Presence of type H vessels in the bone marrow in different age cohorts and proliferation of bone marrow cells assessed by KI-67 staining. (**a**) Immunofluorescence analysis shows that type H vessels (EmcnhiCD31hi) are more abundant at the femoral growth plate of young mice (4 weeks old) as compared to old mice (18 weeks old). (**b**) Immunofluorescence analysis of nuclear Ki67 hardly stains for endothelial cells. Proliferation was heterogeneously distributed at different times, similar to bones without (w/o) implant.
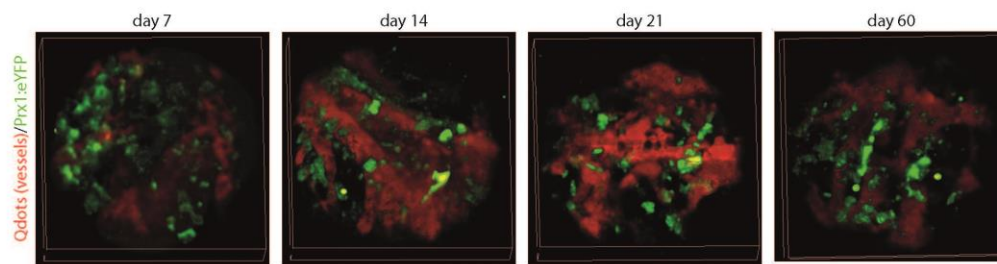
Supplementary Figure 9 | LIMB analysis in Prx1:YFP mice reveals continuous remodeling of the stroma compartment in the mouse femur over months. Prx1:YFP mice, which express eYFP in stromal and endothelial cells, received the LIMB implant and were injected prior to each imaging session with Qdots to label the vasculature. During the bone healing phase, at day 7, 14 and 21 post-surgery, a strong reshaping of the stromal network becomes evident from 3D fluorescence imaging in the same individual. The changes continue also at day 60 post-surgery under homeostatic conditions. Imaging volume 150x150x66 μm³.

myeloid CX₃CR1+ eGFP cells blood vessels SHG (bone/collagen)

d3   d7   d21   d31
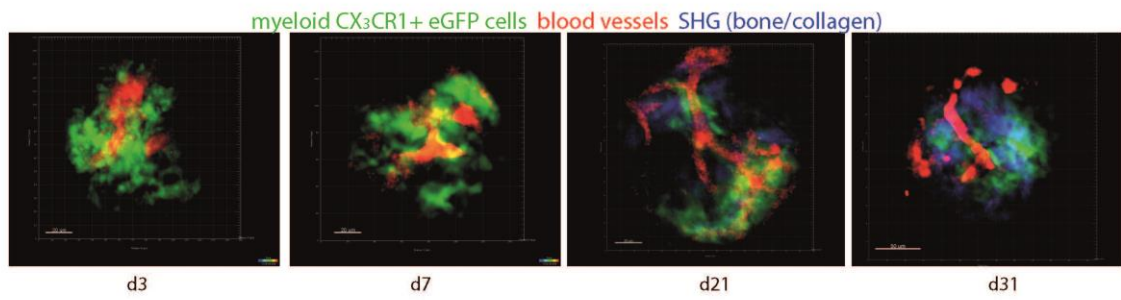
Supplementary Figure 10 | Repeated LIMB imaging using a short (500 μm long) endoscope tubing in a CX3CR1 eGFP mouse. 3D reconstructions of fluorescence images at day 3, 7, 21 and 31 post-surgery are depicted. Myeloid CX3CR1+ cells are depicted in green, blood vessels labeled by Qdots in red and second harmonic generation (SHG) originating from collagen and bone in blue. This time course reveal the initial inflammatory phase, followed by vascular remodeling and finally by soft tissue and bone growth, after drill hole injury. Hence, after 31 days we observe in front of the LIMB microendoscope a situation similar to that expected in endosteal regions.

Rakhymzhan et al.

Please also refer to the following link to digitally access the supplementary movies:

https://doi.org/10.1038/s41598-017-07165-0

SCIENTIFIC REP⚙RTS

OPEN

Synergistic Strategy for Multicolor Two-photon Microscopy: Application to the Analysis of Germinal Center Reactions In Vivo

Asylkhan Rakhymzhan[1], Ruth Leben[1], Hanna Zimmermann[1,4], Robert Günther[1], Peggy Mex[1], David Reismann[1], Carolin Ulbricht[1,3], Andreas Acs[2], Alexander U. Brandt[4], Randall L. Lindquist [1], Thomas H. Winkler[2], Anja E. Hauser[1,3] & Raluca A. Niesner[1]

Simultaneous detection of multiple cellular and molecular players in their native environment, one of the keys to a full understanding of immune processes, remains challenging for *in vivo* microscopy. Here, we present a synergistic strategy for spectrally multiplexed *in vivo* imaging composed of (i) triple two-photon excitation using spatiotemporal synchronization of two femtosecond lasers, (ii) a broad set of fluorophores with emission ranging from blue to near infrared, (iii) an effective spectral unmixing algorithm. Using our approach, we simultaneously excite and detect seven fluorophores expressed in distinct cellular and tissue compartments, plus second harmonics generation from collagen fibers in lymph nodes. This enables us to visualize the dynamic interplay of all the central cellular players during germinal center reactions. While current *in vivo* imaging typically enables recording the dynamics of 4 tissue components at a time, our strategy allows a more comprehensive analysis of cellular dynamics involving 8 single-labeled compartments. It enables to investigate the orchestration of multiple cellular subsets determining tissue function, thus, opening the way for a mechanistic understanding of complex pathophysiologic processes *in vivo*. In the future, the design of transgenic mice combining a larger spectrum of fluorescent proteins will reveal the full potential of our method.

Multiplex fluorescent imaging as well as non-imaging techniques are widely used to follow immune responses in space and time. Most *ex vivo* studies are performed on fixed, static samples, making repeated investigations of the same sample possible by serial detection. Hence, established methods such as flow cytometry (FACS)[1] or immunofluorescence-based confocal microscopy[2] are capable of recording 10 or more parameters by using sequential excitation of differentially excited fluorophores. Multi-epitope-ligand cartography[3] (MELC) allows even more parameters to be investigated, over 100 within one sample, by using multiple cycles of labeling, detection, and bleaching. Although such approaches are appropriate for *ex vivo* investigations of fixed tissue, they are not suitable for intact, live tissue, which is highly dynamic on both the cellular and molecular levels. Referring especially to MELC, the great multiplexing potential but time-consuming acquisition can be used only as a preliminary step for a full understanding of the complex cellular interplay during immune responses. *In vivo* spectrally multiplexed imaging approaches are needed to visualize and understand the dynamic dimensions of pathophysiologic phenomena.

Over the last decades, *in vivo* two-photon microscopy has become the main tool for imaging cellular responses in live animals, with particular application in neuroscience and immunology[4–10]. The inherent optical sectioning, high penetration depth and low phototoxicity of two-photon microscopy allow visualization of cellular dynamics in space and time, in their natural environment *in vivo*. For instance, the dynamic processes taking place during the germinal center (GC) reaction are highly relevant to understanding mechanisms involving the maturation of B cell immune responses. *In vivo* imaging of GCs has allowed quantitative description and modeling of B cell

[1]Deutsches Rheumaforschungszentrum, a Leibniz Institute, Berlin, Germany. [2]Nikolaus-Fiebiger-Zentrum, Division of Genetics, Department of Biology, University of Erlangen-Nürnberg, Erlangen, Germany. [3]Immundynamics, Charité – Universitätsmedizin Berlin, Berlin, Germany. [4]NeuroCure Clinical Research Center, Clinical and Experimental Multiple Sclerosis Research Center, Department of Neurology, Charité – Universitätsmedizin Berlin, Berlin, Germany. Correspondence and requests for materials should be addressed to R.A.N. (email: niesner@drfz.de)

motility patterns as well as communication between antigen-specific B cells and T follicular helper (Tfh) cells and interactions of B cells with follicular dendritic cells (FDC)[5,10]. However, current *in vivo* techniques allow for simultaneous observation of typically 3 to 4 fluorophores[11–14] in addition to second and/or third harmonics generated from organized structures like collagen. This is not enough to monitor the communication and interplay of all cellular and tissue compartments involved in a germinal center reaction, as GC B cells, naive B cells, Tfh cells and FDCs must all be visualized, leaving no channels for reporters of signaling, clonality, cell division, or cell fate. How antigen-presenting cells, such as dendritic cells, communicate with T cells, how germinal center B cells in contrast to naïve B cells interact with T cells and/or with FDCs, how the selected germinal center B cells egress as plasma blasts or memory B cells from the germinal center and how the vasculature is involved in all these processes – all these phenomena have been studied in detail, however each in separate experiments. The interactions between GC B cells, Tfh cells, and FDCs also result in many signaling events which have also been imaged, but in isolation, with one signaling event per experiment. Only their correlated investigation in one and the same germinal center will allow conclusions on the spatiotemporal sequence of their occurrence, giving a more complete picture of the adaptive immune response.

The quantitative limit for simultaneous visualization of multiple fluorophores in current intravital microscopy can be overcome by solving three main challenges[15]: optimization of the excitation scheme, extension of the fluorescence range using far-red and near-infrared (NIR) probes, and improving the effectiveness of spectral unmixing.

For *in vivo* imaging, it is critical to simultaneously image all fluorophores. As cells move dynamically, sequential excitation of large volumes will lead to difficulties in synchronizing images acquired at different times. This requires efficient simultaneous excitation over the entire range of fluorophores, which is easily performed with relatively inexpensive continuous-wave lasers, but is difficult to achieve with the femtosecond-pulsed laser sources optimal for two-photon excitation. Different excitation schemes in two-photon microscopy were used to visualize multiple fluorophores in live animals by us and others: sequential single excitation by Ti:Sa laser[14], dual excitation by a Ti:Sa laser and an optical parametric oscillator (OPO)[11,12], and triple excitation using wavelength mixing of Ti:Sa and OPO, leading to two-color-two-photon excitation[13]. The two-color two-photon excitation using picosecond or even femtosecond lasers was first demonstrated as the wavelength mixing of 800 nm and its second harmonic of 400 nm on laser dyes (p-therphenyl, 2-methyl-5-tert-butyl-p-quaterphenyl) and on tryptophan[16,17].

Thanks to recent developments of nonlinear fiber optics[18] and ceramic-based electro-optic intensity modulators[19], cheaper alternative optical sources have become available for two-photon excitation, which are in principle applicable to sets of multiple fluorophores. The invention of photonic crystal fibers (PCF) in the 1990s[20,21] stimulated a rapid development of optical sources with extreme spectral broadening, termed supercontinuum (SC) generation. Due to the broad spectral bandwidth, a fiber SC offers simultaneous access to multiple wavelengths in a uniform spatial profile of a single-wavelength laser[22]. Furthermore, another alternative for multiple fluorophore excitation was achieved by using fast wavelength modulation based on ceramic PMN-PT intensity modulators and soliton self-frequency shift in nonlinear PCF[19]. This system switches wavelength of a 100 fs pulsed laser source within the range of 200 nm in approximately 5 μs, which is problematically long for point-scanning systems. While these excitation sources have great potential, their application with common fluorescent proteins *in vivo* needs to be better characterized.

The near infrared (NIR) region, known as the optical window, is optimal for deep imaging in live mammals, as it has relatively low scattering, reduced autofluorescence and high tissue transparency, due to low absorption of water and haemoglobin at these wavelengths[23]. Recent developments in the field of NIR fluorescent proteins[24,25] have extended the detection range of fluorescent probes, resulting in an increased number of available fluorophores for *in vivo* imaging experiments, and the longer emission wavelengths of these proteins should permit imaging deeper into tissue.

Spectrally multiplexed imaging implies not only the effective excitation and detection of multiple fluorophores, but also their unambiguous discrimination. In order to distinguish between multiple fluorophore signals, a large variety of spectral unmixing methods have been developed. Linear spectral unmixing is a simple, widely used method available both in commercial (Zeiss, Nikon) and in open-source software (Fiji/ImageJ, J. Walter PlugIn). The algorithm is based on the assumption that the detection signal is linearly dependent on the contributing fluorophores[26,27]. Alternatively, spectral deconvolution was applied to separate six different signals in the brain of triple transgenic mice by using sequentially collected hyper-stacks of fluorophore signatures[14]. Combining color balancing[28] and signal subtraction from adjacent channels allowed tumor cell lines expressing one of five different fluorophores to be distinguished in immunodeficient mice[11]. As scattering and wave front distortions are extremely nonlinear with respect to wavelength, we expect the tissue environment to change the spectra of the contributing fluorophores nonuniformly. In this case, the linear unmixing approach cannot isolate different components contributing to the emitted signal. Better separation quality may be achieved by using similarity approaches, which rely on reference spectra acquired *in situ*[29]. Further, current unmixing approaches do not allow the detection of more fluorophores than the available detection channels, in simultaneously acquired imaging data.

We demonstrate simultaneous spectrally multiplexed detection of seven fluorophore signals corresponding to seven cellular and tissue compartments in popliteal lymph nodes of live mice: naïve B cells, CD4+ T cells, antigen-specific B1-8 germinal center B cells, plasmablasts, follicular dendritic cells, blood vessels and macrophages, including tingible body macrophages. To achieve this aim, we combined: (i) wavelength mixing allowing for effective simultaneous triple two-photon excitation of fluorophores, (ii) extension of the fluorescence detection range by using far-red and NIR fluorophores and, (iii) effective non-analytic spectral unmixing. As an effective color discrimination technique, we developed a new algorithm based on the principle of similarity unmixing, called SIMI. This algorithm stays fully functional beyond the fundamental limit of linear unmixing, where the number of fluorophores cannot exceed the number of detection channels. Using this novel imaging

strategy, we were for the first time able to investigate the dynamics of naïve B cells, antigen-specific B cells, CD4+ T helper cells, follicular dendritic cells and tingible body macrophages as well as the immediate egress of plasma blasts during ongoing GC reactions, while highlighting the vasculature as the site of cellular exchange between different organs. Our technique is a versatile tool able to open new insights into mechanisms of complex dynamic immune processes *in vivo*, applicable to the investigation of any organ, in which the communication of various cell subtypes defines tissue function and dysfunction.

Results

Two-photon microscope setup for simultaneous triple excitation using wavelength mixing.

In order to achieve effective triple excitation in a two-photon microscope, for dynamic, spectrally multiplexed intra-vital imaging, we optimized a conventional setup, as described in the following (Fig. 1a). The excitation system of our microscope consists of two laser sources: a femtosecond Ti:Sa laser and an optical parametric oscillator (OPO) pumped by the Ti:Sa (Fig. 1a). Spatial overlap of OPO and Ti:Sa beams in the microscope allows simultaneous dual two-photon excitation of fluorophores[6]. We achieved optimal spatial overlap of the two laser sources by imaging sub-diffraction nano-spheres of 100 nm diameter and 605 nm emission, excitable by both lasers (Fig. 1c). In addition, we synchronized the pulse trains of Ti:Sa and OPO in time, using a customized delay stage as shown in Fig. 1a. The delay stage is positioned on the optical path of the OPO and consists of two 90° prisms, with broad-band reflecting catheti. One prism is fixed, the other is placed on a piezo stage with a translation step of 15 nm. Thus, by moving the piezo stage, the optical path length of the OPO can be varied with an accuracy of 50 attoseconds (0.05 fs). In this way, OPO and Ti:Sa pulse trains can be adjusted to perfectly overlap, since Ti:Sa and OPO have the same repetition rate, as the OPO is being pumped by the Ti:Sa. We verified synchronization of the pulse trains by measuring sum frequency generation (SFG) signals in a powder of birefringent potassium dihydrogen phosphate (Suppl. Video 1).

Spatial foci overlap of the two lasers in the microscope enables dual two-photon excitation originating from the individual laser sources, i.e. only Ti:Sa and only OPO – results in symmetric two-photon excitation processes. The additional time overlap of the pulse trains allows for a third excitation process: two-photon excitation triggered by the combination of one Ti:Sa and one OPO photon (Fig. 1e). This process represents an asymmetric two-photon excitation (ATPE) and is a wavelength mixing process of the two lasers in non-linear medium, similar to SFG. ATPE is equivalent to a two-photon excitation with a virtual wavelength $\lambda_3 = 2/(1/\lambda_1 + 1/\lambda_2)$, where λ_1 is the wavelength of Ti:Sa and λ_2 is the wavelength of OPO. We optimized this wavelength mixing configuration to effectively excite various blue and green emitting fluorophores by Ti:Sa ($\lambda_1 = 850$ nm), far-red and near-infrared emitting fluorophores by OPO ($\lambda_2 = 1230$ nm), and orange and red emitting fluorophores by ATPE (virtual $\lambda_3 = 1005$ nm). Hence, triple two-photon excitation of a broad range of fluorophores (Fig. 1e) and independent control of orange and red fluorophore signal are possible (Fig. 1d, Suppl. Video 2).

In order to perform triple two-photon excitation in an effective manner, a maximum ratio of peak to average power of both Ti:Sa and OPO is needed. Therefore, it is crucial to control the pulse widths of not only both lasers, but also of their wavelength mixing. Propagation through dispersive optical elements, such as animal tissue, causes significant broadening of femtosecond pulses due to group velocity dispersion (GVD). To counteract this, we used external prism-based pulse compressors for both the Ti:Sa and the OPO. For the Ti:Sa beam, a conventional pulse compressor[30] with a two-prism configuration was already integrated in our setup. In order to mitigate GVD in the OPO beam path, we built a compact single-prism pulse compressor[31]. The single-prism design consists of a main prism, a roof mirror and a corner cube (Fig. 1b). Negative dispersion of the pulses is achieved on the four-pass travel from the main prism to the corner cube, reducing the nominal distance in the pulse compressor to the half as compared to conventional "two-prism" pulse compressors. The use of only one prism and the optical properties of the corner cube simplify compensation of different spatiotemporal distortions in the output beam as well as alignment of the setup (*Suppl. Material*). Using a beam auto-correlator, we found that the OPO pulse width without GVD compensation increases from 190 fs at the laser output to 340 fs in the microscope. Our single-prism compressor narrows down the pulse duration to 160 fs at the focus of the microscope. The pulse width of the Ti:Sa beam in the microscope is ~250 fs after GVD compensation (Suppl. Figure 1). Finally, the cross-correlation pulse width of the wavelength mixing of 850 nm (Ti:Sa) and 1230 nm (OPO) as measured by ATPE of mOrange2 amounts to ~250 fs (Fig. 1d). All pulse width values were calculated by approximating the autocorrelation and cross-correlation curves with Gaussian functions. The peak intensity values at 10 mW average power at the focal plane (objective lens NA = 1.0) amount to $2.34 \cdot 10^{28}$ photon/cm²·s at 850 nm (Ti:Sa), $2.47 \cdot 10^{28}$ photon/cm²·s at 1230 nm (OPO) and $2.77 \cdot 10^{28}$ photon/cm²·s at virtual the 1005 nm for ATPE and SFG. The total real photon flux at the sample surface amounts to $4.81 \cdot 10^{28}$ photon/cm²·s, independent of the lasers wavelengths (in total approx. 20 mW average power). The dwell time of both lasers within one focus of the sample did not exceed 4 µs to avoid photobleaching and photodamage. Thus, the optical premises for effective, simultaneous triple two-photon excitation of fluorophores with emission spectra ranging from blue to near-infrared and its use in dynamic live imaging are given.

Spectrally multiplexed imaging of live cells by simultaneous triple excitation of up to six chromophores.

Using our setup, we demonstrated spectral multiplexing on mixtures of isolated cells either expressing fluorescent proteins or labeled by dyes for live imaging. We chose two different *in vitro* models, which can be easily translated to *in vivo* imaging experiments. First, we imaged a mixture of human embryonic kidney (HEK-293T) cell lines, each expressing one out of five fluorescent proteins: eCFP, eGFP, mOrange2, mKate2 and eqFP670 (Fig. 2a). This model resembles features of Brainbow3.0 or Confetti mice, which have been used in live animal imaging to monitor clonal relationships on the cellular level in various tissues[32, 33]. eGFP, mOrange2 and mKate2 were chosen as the core of the Brainbow3.0 transgenic line due to their high photo-stability, minor tendency to aggregate *in vivo*, low sequence homology and minimal spectral overlapping[32]. In order to extend the
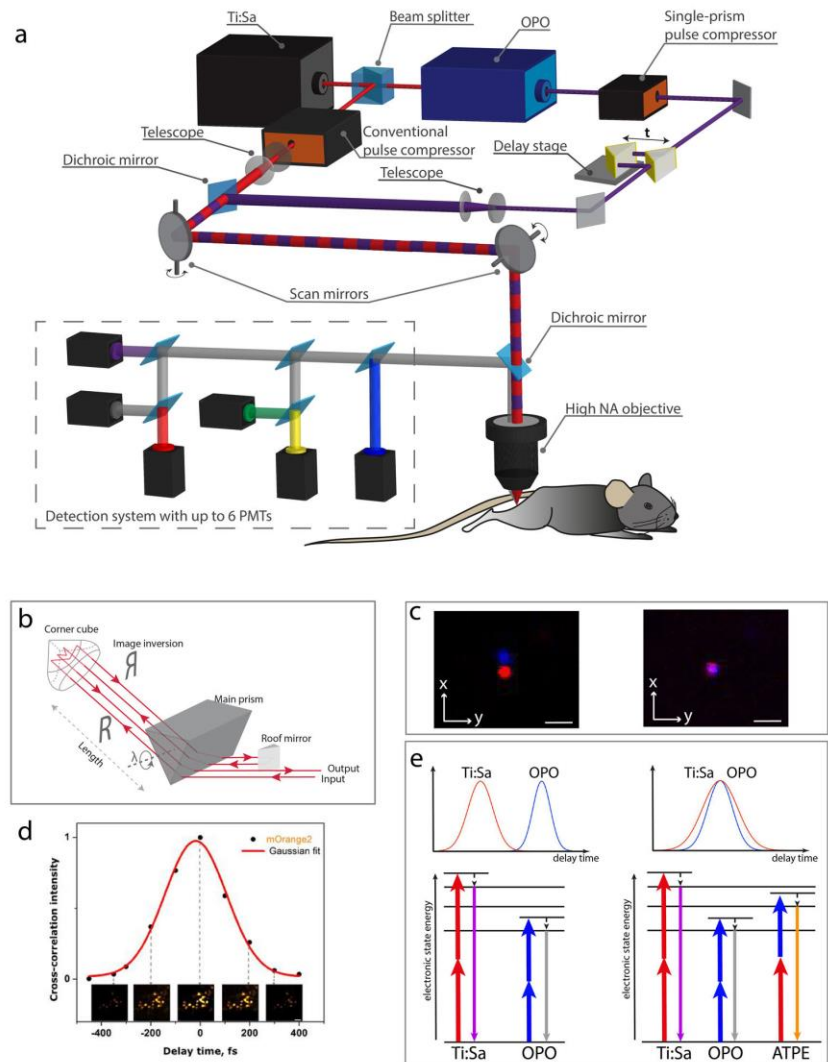
Figure 1. Principle of wavelength mixing two-photon microscopy: setup and characterization. (**a**) Imaging setup. A femtosecond laser (Ti:Sa) beam is divided in two fractions by a beam splitter. One is adjusted in a microscope, the second pumps an OPO. Pulses from Ti:Sa and OPO are synchronized using a delay stage (t) and spatially coaligned. GVD compensation is achieved using a conventional prism-based and a single-prism pulse compressors for Ti:Sa and OPO, respectively. The relative divergence of two laser beams is controlled using telescopes. Galvanoscan mirrors provide raster scanning the area up to $500 \times 500\,um^2$. Chromatic aberration between NIR and IR wavelength of two lasers is corrected by the high numerical aperture objective. The non-descanned detection system is equipped with six PMTs. (**b**) Single-prism pulse compressor. Negative dispersion is accumulated on the four-pass travel through the main prism. The distance between a corner cube and the main prism is half that of the conventional design due to the image inversion of the corner cube. Pulse compression at different wavelengths can be achieved by rotating only one prism. (**c**) Spatially separated (left) and overlapping (right) Ti:Sa (red) and OPO (blue) foci in the microscope, measured on a 100 nm fluorescent bead ($\lambda_{emission} = 605$ nm). Scale bars, $0.2\,\mu m$. (**d**) Optimization of the ATPE. The mOrange2 fluorescent signal can be independently controlled by adjusting the delay between pulses. The insets represent images of HEK cells expressing mOrange2 at different delay times. Scale bar, $50\,\mu m$. (**e**) Spatiotemporal overlapping of two laser pulses. Left side: unsynchronized pulses (850 nm and 1230 nm) provide dual two-photon excitation, i.e. two parallel symmetric two-photon excitation processes. Right side: The wavelength mixing appears only if the pulses are synchronized in time and the two foci are matched in space. A third, asymmetric two-photon excitation process additionally takes place, making further fluorophores visible. Hence, simultaneous triple two-photon excitation of a broad set of chromophores is achieved.
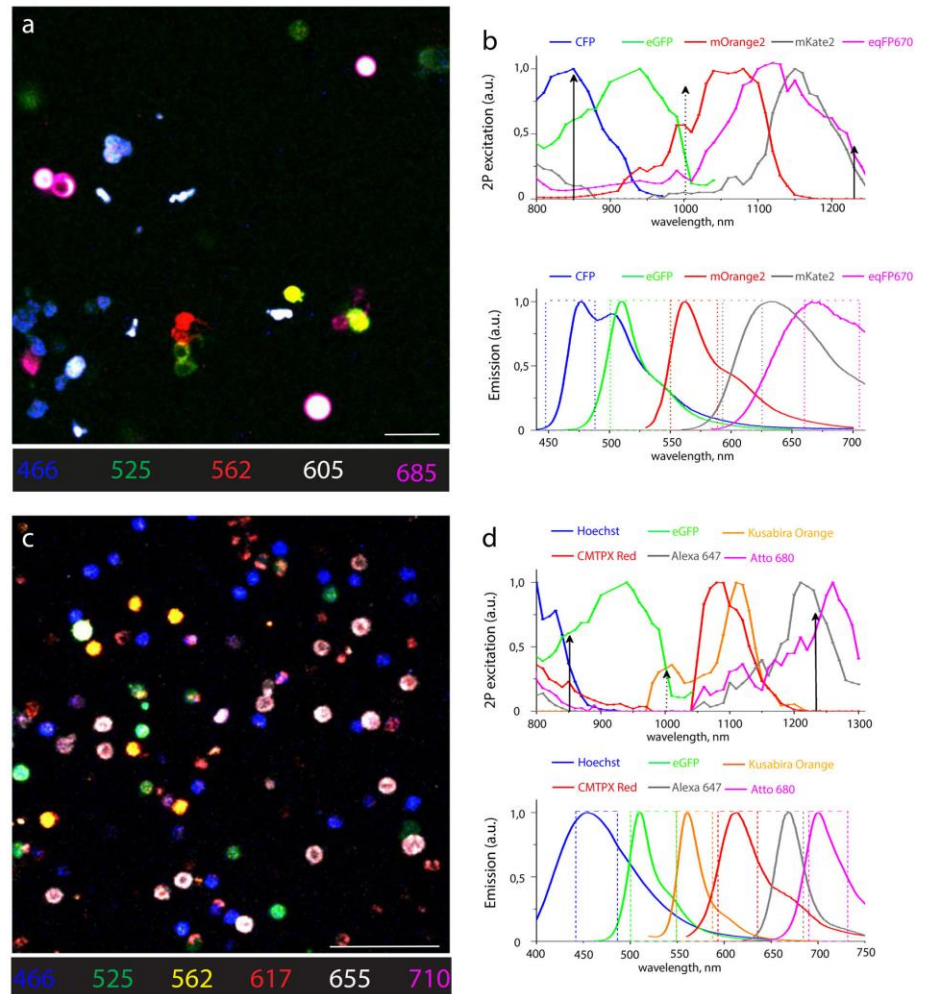
Figure 2. *In vitro* spectrally multiplexed imaging of five fluorescent proteins in HEK cells and six chromophores in murine splenocytes. (**a**) Raw fluorescence image of a mixture of HEK cells singly expressing one of five FPs: CFP, eGFP, mOrange2, mKate2, and eqFP670. (**b**) Two-photon excitation and emission spectra of CFP, eGFP, mOrange2, mKate2, and eqFP670. Two-photon spectra of mOrange2, mKate2, and eqFP670 were recorded in this work (Methods). Arrows indicate effective excitation wavelengths and rectangles indicate the filter bandwidth of the five detection channels (a.u., arbitrary units). (**c**) Raw image of a mixture of murine splenocytes each labelled with one of six fluorophores: Hoechst, eGFP, Kusabira Orange, CMTPX Red, Alexa 647, and Atto 680. (**d**) Two-photon excitation and emission spectra of Hoechst, eGFP, Kusabira Orange, CMTPX Red, Alexa 647, and Atto 680. 2P spectra of Hoechst, Kusabira Orange, CMTPX Red, Alexa 647, and Atto 680 were recorded (Methods). Arrows indicate optimal excitation wavelengths and rectangles indicate the filter bandwidth of the six detection channels (a.u., arbitrary units). Scale bars, 50 μm.

emission spectrum of the model (and its application range), we added two more proteins, eCFP and eqFP670. The eqFP670 is a NIR fluorescent protein based on the dimeric far-red fluorescent protein Katushka-9-5[25], characterized by high photo- and pH-stability, outstanding brightness and low cytotoxicity.

Secondly, we imaged isolated murine splenocytes containing one out of six fluorophores (Fig. 2c), commonly used in multiplexed intravital imaging of various cell subsets during immune reactions. The six fluorophores included both dyes, i.e. Hoechst, CMTPX Red, Alexa647 and Atto680, as well as the fluorescent proteins eGFP and monomeric Kusabira Orange. We chose these fluorophores based on their high photostability and brightness, low cytotoxicity, and minimal spectral overlap.

In order to ensure optimal triple excitation of the chosen chromophores, both fluorescent proteins and dyes, we measured their two-photon excitation spectra in cells, as previously described[12] (Fig. 2b,d; upper panels). Spectra were acquired in live cells to allow for better comparability with *in vivo* preparations. Thus, we found that

wavelength mixing of 850 nm (Ti:Sa) and 1230 nm (OPO) pulses is the optimal combination for efficient simultaneous excitation of both the five fluorescent proteins expressed by HEK cells and of the six chromophores used to label splenocytes (Fig. 2a,c).

Based on the emission spectra of our selected fluorophores (Fig. 2b,d; lower panels), we defined an optical system of dichroic mirrors and interference filters to distribute the emitted signal on the six PMT detectors (Fig. 1a), in order to achieve optimal spectral resolution of the chromophores. However, despite this optimized spectral separation of the detected signal, significant crosstalk is observed between several chromophores, thereby preventing their unambiguous spectral separation and detection. This shortcoming can only be resolved by post-processing of the imaging data, using specialized spectral unmixing approaches, as described in the next section.

SIMI – similarity unmixing approach for optimal post-processing chromophore resolution in imaging data.
Any spectral unmixing procedure represents a transformation of the image from the "detection channel space" to the "fluorophore space". In order to distinguish between chromophores excited by simultaneous triple two-photon excitation, we developed a new algorithm of spectral unmixing named similarity unmixing (SIMI). Starting from the concept of similarity between reference spectra and the measured signal[23], the SIMI approach is a numerical pixel-based method, which separates mixed colors based on similarities between overlapping fluorophores as well as on the spectral fingerprints of the individual fluorophores (spectral signatures). The SIMI approach originates from the widely-used linear unmixing method, but it does not follow its algebraic solving strategy. Thus, it enables the simultaneous identification of a higher number of chromophores than available detector channels from imaging data.

The linear unmixing algorithm is based on the assumption that the total signal S_i measured on every detection channel is linearly proportional to the combination of contributing fluorophores F_j[34]:

$$S_i = a_{1i} \times F_1 + a_{2i} \times F_2 + \cdots = \sum_{i=1}^{m} a_{ij} F_j, \quad i = 1 \div m \tag{1}$$

or in matrix form:

$$\begin{pmatrix} S_1 \\ \vdots \\ S_n \end{pmatrix} = \begin{bmatrix} a_{11} & \cdots & a_{1m} \\ \vdots & \ddots & \vdots \\ a_{n1} & \cdots & a_{nm} \end{bmatrix} \times \begin{pmatrix} F_1 \\ \vdots \\ F_m \end{pmatrix}, \tag{2}$$

where α_{ij} is the mixing matrix element, i is the channel index, j is the fluorophore index, n is the number of detection channels, m is the number of fluorophores. The principle of linear unmixing consists in finding the vector F_j by calculating the contribution values of the given fluorophores, i.e. by algebraically solving the system of linear equations (1) or (2)[26,27]. The matrix equation (2) may be also written as[35]:

$$\begin{pmatrix} S_1 \\ \vdots \\ S_n \end{pmatrix} = F_1 \cdot \begin{pmatrix} a_{11} \\ \vdots \\ a_{n1} \end{pmatrix} + F_2 \cdot \begin{pmatrix} a_{12} \\ \vdots \\ a_{n2} \end{pmatrix} + \cdots + F_m \cdot \begin{pmatrix} a_{1m} \\ \vdots \\ a_{nm} \end{pmatrix}, \tag{3}$$

where it can be interpreted in terms of fluorophore components or fingerprints. The column $a_{1j} \ldots a_{nj}$ on the right side of the equation (3) represents the fingerprint of the fluorophore F_j, satisfying the normalization condition $\sum_{i=1}^{m} a_{ij} = 1$, for $i = 1 \div m$. Each fingerprint can be defined from the normalized signals $c_1 \ldots c_n$ measured at single color condition, when only one fluorophore is present, $F_j \neq 0$ and $F_{j \neq k} = 0$, for $k = 1 \div m$. Thus, equation (3) becomes:

$$\begin{pmatrix} S_1 \\ \vdots \\ S_n \end{pmatrix} = S_{max} \cdot \begin{pmatrix} c_1 \\ \vdots \\ c_n \end{pmatrix} = F_j \cdot \begin{pmatrix} a_{1j} \\ \vdots \\ a_{nj} \end{pmatrix}, \tag{4}$$

with S_{max} and F_j as constant values. The fingerprint elements $a_{1j} \ldots a_{nj}$ represent a relative intensity distribution, which reflects the emission spectrum of fluorophore F_j.

SIMI algorithm assigns an unknown fluorescence signal fingerprint to a fluorophore by comparing and finding the closest match between the normalized signal column $b_{1j} \ldots b_{nj}$ measured from the images with mixed fluorophores and the fingerprint elements $a_{1j} \ldots a_{nj}$ obtained from images of single fluorophores:

$$\begin{pmatrix} S_1 \\ \vdots \\ S_n \end{pmatrix} = S_{max} \cdot \begin{pmatrix} b_1 \\ \vdots \\ b_n \end{pmatrix} \leftrightarrow F_1 \cdot \begin{pmatrix} a_{11} \\ \vdots \\ a_{n1} \end{pmatrix}, F_2 \cdot \begin{pmatrix} a_{12} \\ \vdots \\ a_{n2} \end{pmatrix}, \ldots, F_m \cdot \begin{pmatrix} a_{1m} \\ \vdots \\ a_{nm} \end{pmatrix}. \tag{5}$$

The matching procedure was performed by a gradient fitting approach that minimizes the square difference of the signal b_i and the fingerprint a_{ij} values:

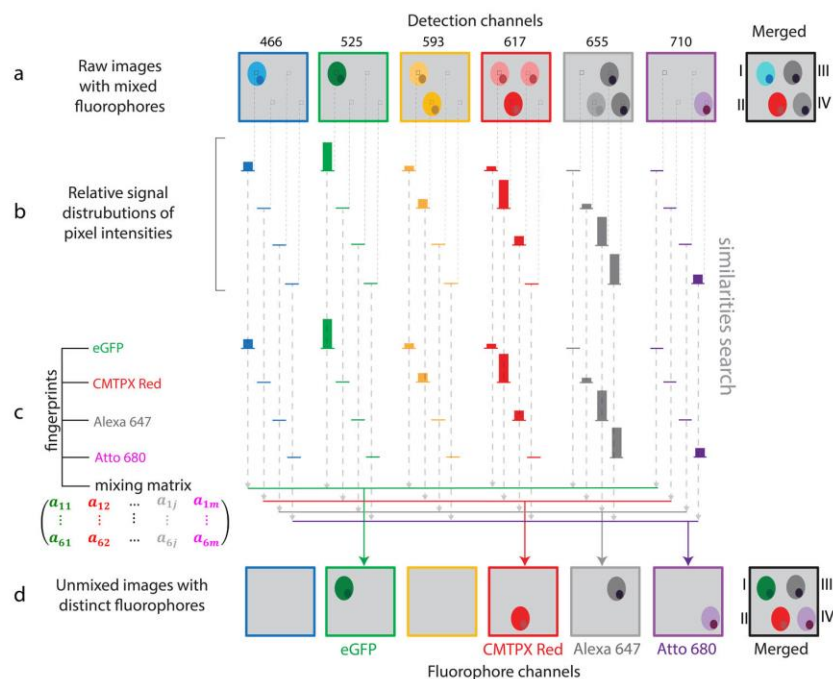$$R_j^2 = \sum_i \left(b_i - a_{ij} \right)^2. \tag{6}$$

Figure 3. Principle of similarity unmixing algorithm. (**a**) Raw images of cellular objects show crosstalk in six detection channels. The merged image illustrates color ambiguity of four cells labelled from I to IV. (**b**) The algorithm extracts a relative signal distribution from six channels pixel by pixel. (**c**) The fingerprints of eGFP, CMTPX Red, Alexa647, Atto680 are measured from single-labeled cells. The algorithm searches for similarities between the signatures of undefined fluorophores from (**b**) and the known fingerprints channel by channel (dashed arrows). (**d**) Unmixed images with separated distinct fluorophores. The closest match with one of the fingerprints indicates similarity of the undefined fluorophore from (**c**) with the fluorophore of this fingerprint. The determined fluorophore signal is collected in the distinct fluorophore channel (colored arrows). As a result, color separation of the cells I–IV is achieved in the merged image from the fluorophore channels.

Owing to the fact that our algorithm defines the degree of correlation, or similarity, but not the contribution value of the mixed fluorophores, the correct assignment of the mixed colors can be achieved only if each cell contains only one chromophore, i.e. one-fluorophore-per-cell condition.

We implemented the SIMI algorithm into the spectral unmixing PlugIn of Fiji/ImageJ (J. Walter). The SIMI procedure is schematically shown for the detection system with six channels in Fig. 3. Undefined fluorophore signals from four cell types show color mixing caused by bleed-through into neighboring channels (Fig. 3a). First, the algorithm extracts the normalized signal distribution over channels $b_1 \dots b_n$ according to equation (5) in each pixel. Individual fluorophores exhibit a signal distribution corresponding to their emission spectra (Fig. 3b). Next, the algorithm searches for similarities between the normalized distribution $b_1 \dots b_n$ and the measured fingerprints $a_{1j} \dots a_{nj}$ in equation (4) (dashed arrows in Fig. 3b,c). The closest match with one of the fingerprints identifies the signal origin and, thus, the fluorophore. Finally, the identified signal is displayed in a dedicated channel (Fig. 3d). As a result, the four cells have the closest match with the fingerprints of eGFP, CMTPX Red, Alexa647 and Atto680, respectively, and are placed in the corresponding fluorophore channels (Fig. 3d). The merged image of the fluorophore channels shows complete color unmixing. The cell pairs I–II and III–IV represent different levels of color mixing. Cells I and II show clear domination of the green and red channels, respectively. Color balance correction can easily assign these cells to eGFP and CMTPX Red expression, as seen on the merged image in Fig. 3a. In contrast, cells III and IV have their maximum signal in the same channel (grey) and are hardly distinguishable. To identify these cells, the information from all channels needs to be used. The SIMI algorithm is able to separate cells III and IV based on the signal difference in the red and magenta detection channels.

In order to determine the fingerprint of each fluorophore in our *in vitro* models, we imaged live cells containing only a single fluorophore, either a fluorescent protein or dye, as shown in the example of HEK-293T cells expressing mOrange2 (Fig. 4a). Each row corresponds to one of four excitation schemes: excitation only by Ti:Sa, excitation only by OPO, triple excitation by wavelength mixing of Ti:Sa and OPO, and dual excitation by temporally non-synchronized Ti:Sa and OPO. In HEK cells expressing one of five fluorescent proteins: eCFP, eGFP, mOrange2, mKate2 and eqFP670, mOrange2 was mostly excited by ATPE as highlighted by the difference
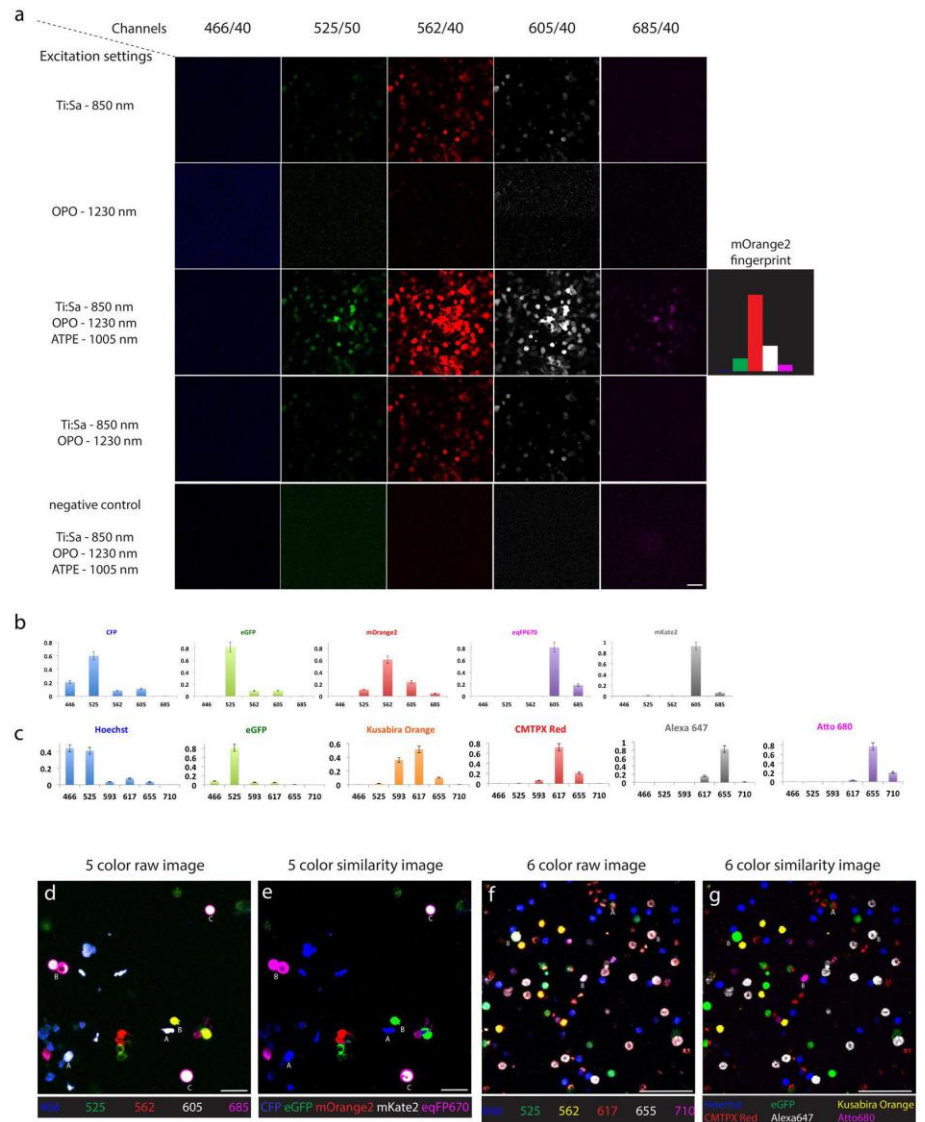
Figure 4. Similarity unmixing of spectrally multiplexed images of isolated cells. (**a**) Single color measurement of HEK cells expressing only mOrange2. Rows represent four excitation schemes: single 2P excitation at 850 nm by Ti:Sa laser; single 2P excitation at 1230 nm by OPO; the wavelength mixing 2P excitation at 850 nm, 1005 nm and 1230 nm by Ti:Sa laser, ATPE and OPO laser, respectively; dual unsynchronized 2P excitation at 850 nm and 1230 nm by Ti:Sa and OPO, respectively. The columns display images from five detection channels. The elements of the fingerprints are calculated as average signal values at the wavelength mixing scheme. (**b**) The fingerprints of five FPs, CFP, eGFP, mOrange2, mKate2, and eqFP670. (**c**) The fingerprints of six fluorophores, Hoechst, eGFP, Kusabira Orange, CMTPX Red, Alexa 647, and Atto 680. (**d,e**) Raw and unmixed images of HEK cell mixture expressing one of five FPs. Letter A indicates example of the crosstalk of the overexpressed signal from minimal spectrally overlapped FPs (case I and II cells in Fig. 3). Letter B indicates example of crosstalk from strong spectral overlap (case III and IV in Fig. 3). Letter C indicates example of both crosstalk effects, signal overexpression and strong spectral overlapping. (**f,g**) Raw and unmixed images of splenocyte mixture expressing six fluorophores at one-fluorophore-per-cell condition. Letter A indicates example of the crosstalk of the overexpressed signal from minimal spectrally overlapped fluorophores (case I and II cells in Fig. 3). Letter B indicates example of the crosstalk from strong spectral overlap (case III and IV in Fig. 3). Scale bars, 50 μm.

between the third and fourth row in Fig. 4a. The last row in Fig. 4a illustrates a negative control of HEK cells without any of our fluorescent proteins. The broad signal distribution from green to magenta channels represents the fingerprint of mOrange2, which is defined as the normalized intensity histogram calculated from the average signal intensities of images in all detection channels. In this way, we determined the fingerprints of all chromophores used in this study (Fig. 4b,c; Suppl. Figs 2 and 3) and applied them to distinguish the images acquired in mixtures of HEK cells (Fig. 4d,e) and splenocytes (Fig. 4f,g). Taken together, while color balance correction is able to resolve fluorophores with strongly differing fingerprints, SIMI provides spectral unmixing for spectral signatures with subtle differences.

SIMI algorithm allows the detection of more fluorophores than available channels *in vivo*. In contrast to the conventional linear unmixing approach, the SIMI algorithm provides solutions in the underdetermined case, i.e. when the number of fluorophores exceeds the number of detection channels. The ability of our algorithm to separate chromophores in the underdetermined case is highlighted in Fig. 5 for the case of two detection channels and three chromophores, i.e. Hoechst, CFP and YFP, in which case the bleed-through between the detection channels leads to ambiguity of the fluorophores in the merged image (Fig. 5a). In the same manner as for the determined or overdetermined case, the SIMI algorithm extracts the normalized signal distribution b_1, b_2 (Eq. 4) from each pixel (Fig. 5b), which is matched to the fluorophore fingerprints (Fig. 5b,c) by least square fitting (Eq. 6). Although the fingerprints contain only two elements b_1 and b_2, different ratios between these elements allow all three fluorophores to be distinguished (Fig. 5d). Theoretically, the number of fluorophores that can be separated from two or more detection channels is not limited (dashed cell in Fig. 5a,d). The larger the differences between the fluorophore fingerprints and the more elements these contain, i.e. the more detection channels are available, the better the quality of fluorophore unmixing. Concluding, the key feature of our algorithm is to separate fluorophores with different fingerprints, even if the number of detection channels is fewer than the number of fluorophores.

In order to demonstrate chromophore separation in the underdetermined case, under *in vivo* conditions, we applied the SIMI algorithm on images acquired in popliteal lymph nodes of anesthetized Rosa26^Confetti/Confetti. Cre^ERT2 mice[36], using three detection channels (466 ± 20 nm, 525 ± 25 nm and 593 ± 20 nm). In these mice, three tissue compartments are labeled by six distinct markers: the nucleus of naïve B cells is labeled by Hoechst, lymphocytes express one of the four fluorescent proteins encoded in the Confetti allele (CFP, hrGFP, YFP or DsRed (Rosa26^Confetti/Confetti.Cre^ERT2 mouse strain) and collagen fibers display second-harmonic generation (SHG) (Fig. 5e,f). The fluorescent proteins are expressed at different locations in lymphocytes: CFP on the membrane, hrGFP in the nucleus and YFP and DsRed in the cytoplasm, and indicate the clonal relations of the cells after tamoxifen induction (3x, every 24 h). The strong spectral overlap of Hoechst, CFP and hrGFP shows both naïve B cells and other lymphocytes mainly in the blue channel. Only the distinct cellular location of the labelling gives a vague hint regarding the different fluorophores and their cellular origin (Fig. 5e). Similarly, both DsRed in lymphocytes and SHG from collagen fibers are mainly observed in the red channel (593 ± 20 nm) and strongly overlap. Using the difference in the individually acquired fingerprints (Fig. 5g), SIMI allows us to separate all six signals and, thus, to unequivocally identify all labeled tissue compartments (Fig. 5f). Additionally, using SIMI, we identified a unique fingerprint for macrophages, including tingible body macrophages, – based on their autofluorescence due to their phagocytic activity, and separate them as a seventh signal within the lymph node germinal centers (Fig. 5f).

Imaging the dynamic orchestration of seven tissue compartments within germinal centers. Successful validation of triple two-photon excitation combined with the SIMI approach on isolated splenocytes labeled by six different chromophores (Fig. 2c,d) allowed us to translate our method to multicolor intravital imaging of germinal center reactions in murine lymph nodes. In order to dynamically investigate the various cellular and tissue players during a well-defined germinal center reaction, we transferred NP-specific B cells isolated from B1-8^+/+ Jκ^−/− Kusabira Orange × Blimp1-GFP mice into C57Bl/6 recipients. We immunized these mice with NP-CGG (Fig. 6a) according to previously published protocols[5, 37] and performed intravital imaging of the popliteal lymph node between day 7 and 9 after immunization, when we expected the peak of germinal center reaction[10]. Five days post-footpad immunization, we transferred Hoechst labeled naïve B cells and CMTPX Red labeled CD4+ T cells. One day prior to imaging, we intravitally labeled follicular dendritic cells (FDC) with CD21/35-Fab-Atto680 injected s.c. into the footpad. Quantum dots (Qdots) 655 were injected intravenously in order to visualize the vasculature immediately prior to imaging. Using triple excitation in our two-photon microscope, we acquired six-channel time-lapse 3D images of germinal centers within B cell zones of popliteal lymph nodes (Fig. 6c). The challenge to distinguish between the individual chromophores (and between the individual cellular compartments) in this image is related not only to the spectral overlap of the emission spectra of the chromophores, but also by the additional autofluorescence of tingible body macrophages. These cells engulf whole or parts of cells labeled by different fluorophores, leading to a combination of various fluorophore signals, i.e. yellow and green areas in Fig. 6c. The autofluorescence in macrophages obstructs especially the identification of germinal center B cells (Kusabira Orange) and of plasma blasts (GFP). Only FDC networks, labeled with a near-infrared dye, indicate the position of two germinal centers (dashed circles, Fig. 6c).

We processed the raw image in Fig. 6c using the SIMI algorithm in the underdetermined case, i.e. six detection channels and seven distinct fluorescence signals. Next to the fluorophores used for labeling of specific cells or structures (Hoechst, eGFP, Kusabira Orange, CMTPX Red, QD655 and Atto680), the autofluorescence of the tingible body macrophages is considered as an additional signal. The autofluorescence of macrophages and fluorescence resulting from Qdots655 inside the vasculature were not recorded in isolated cells, thus, no fingerprints was acquired for these signals. Nevertheless, due to their individual structures and specific origin we could easily define their fingerprints directly from the raw intravital image (Suppl. Fig. 4). Additionally, the spectrally sharp
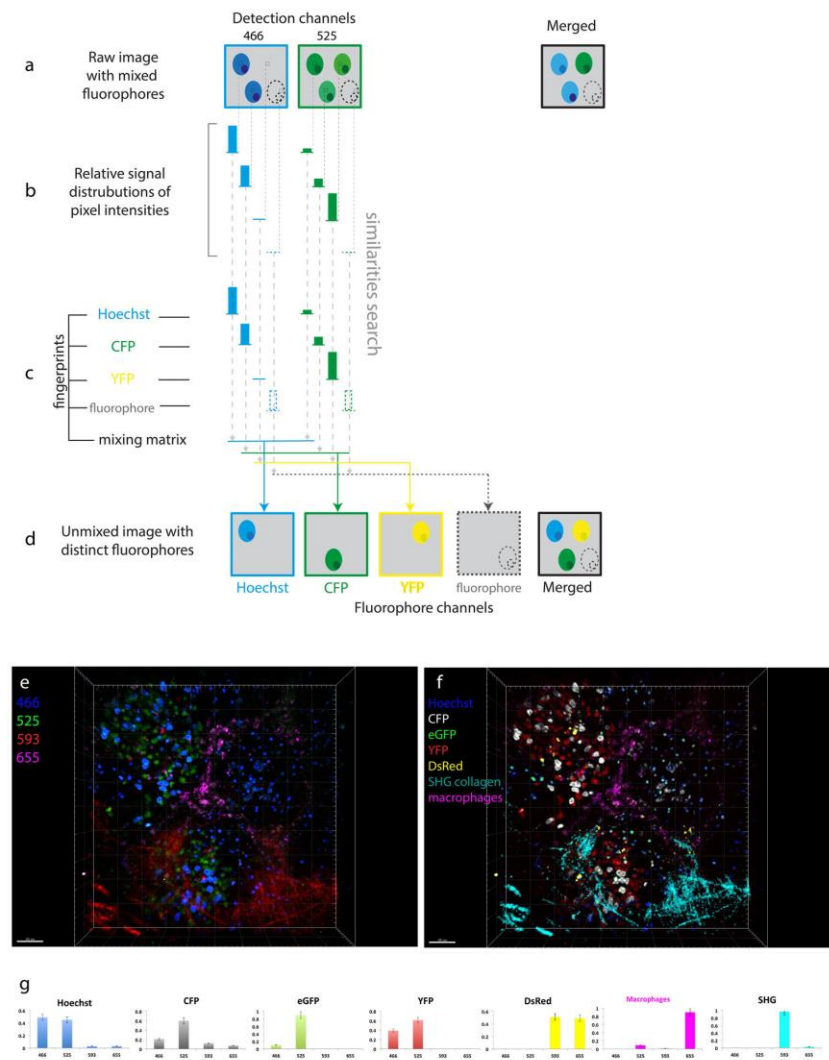
Figure 5. Similarity unmixing in the underdetermined case *in vivo*. (**a**–**d**) Schematic of the similarity algorithm in the underdetermined condition. (**a**) Raw images of cellular objects show crosstalk in two detection channels. The merged image illustrates color ambiguity of cells. The dashed contour represents a cell expressing any additional fluorophore. (**b**) The algorithm extracts a relative signal distribution from two channels pixel by pixel. The pixels containing the cellular fluorescent signal indicate signature of ambiguous fluorophores. (**c**) The fingerprints of Hoechst, CFP, YFP are measured at the single color condition. The algorithm searches for similarities between the signatures of undefined fluorophores from (**b**) and the known fingerprints channel by channel (dashed arrows). The key point for color separation in the underdetermined condition is the different ratios between the fingerprint elements of various fluorophores. The number of fluorophores is not limited unless the difference between their fingerprints is negligible (dashed bars of the fluorophore fingerprint). (**e**) Raw three-dimensional view of murine lymph node imaged on four channels. The lymphocytes are labeled with one of five fluorophores: Hoechst, CFP, hrGFP, YFP, DsRed. (**f**) Unmixed image of (**e**) containing seven color parameters (five fluorescent colors, second harmonic generation (SHG) from collagen and autofluorescence from macrophages). (**g**) The fingerprints of Hoechst, CFP, hrGFP, YFP, DsRed, macrophages and SHG. Scale bars, 50 μm.

signal of second harmonic generation (SHG) of collagen fibers constituting the conduits and the capsule of lymph nodes is the eighth signal distinguishable in our setup (not shown in Fig. 6). The spectrally unmixed 3D image clearly shows the two germinal centers, with labeled FDCs spatially correlating with the accumulation of Kusabira
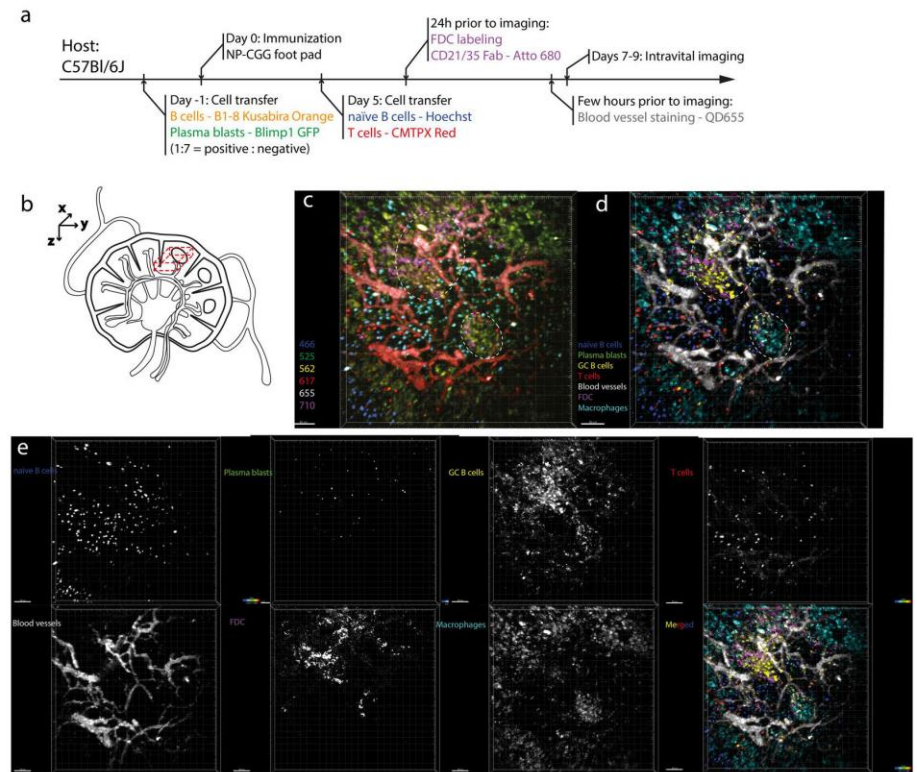
Figure 6. Dynamic multiplex *in vivo* imaging of germinal centers in the lymph node. (**a**) Preparation scheme of six-color mouse model. (**b**) Imaging region of popliteal lymph node (dashed 3D volume). (**c**) Raw 3D fluorescence images ($500 \times 500 \times 40\,\mu m^3$) in the popliteal lymph node of a recipient mouse prepared as described in (**a**) – NP-CGG immunization, imaging at day 7 after immunization. The time-lapse 3D images are recorded in six channels: $466 \pm 20\,nm$ (blue), $525 \pm 25\,nm$ (green), $562 \pm 20\,nm$ (orange), 617 ± 35 (red), 655 ± 20 (grey), 710 ± 20 (magenta). Dashed circles represent ongoing germinal centers identified by the accumulation of B1-8 cells and FDC cells. (**d**) SIMI-unmixed 3D fluorescence image of (**c**). The unmixed image contains seven distinct cellular and tissue compartments (Hoechst – naïve B cells, Blimp1+ plasma blasts – eGFP, GC B1-8 cells - Kusabira Orange, CD4+ T helper cells – CMTPX Red, blood vessels – QD655, FDCs CD21/35 – Atto 680, tingible body macrophages – autofluorescence due to phagocytosis). (**e**) Individual fluorophore channels of the seven tissue compartments in grey scale. Scale bars, $50\,\mu m$.

Orange-labeled GC B cells. Further, the unmixed image reveals the spatial distribution of naïve B cells, CD4+ T cells as well as of plasma blasts, the presence of macrophages within germinal centers and also in the cortical areas of the lymph nodes (Fig. 6d,e).

Using the SIMI algorithm, we could also spectrally unmix time-lapse 3D fluorescence images of germinal centers (Suppl. Video 3). We could analyze the dynamics of all seven cellular and tissue compartments and could track in the same video both naïve B cells and the CD4+ T cells (Fig. 7a,b, Suppl. Videos 4 and 5) labeled with Hoechst and CMTPX red, respectively. In line with previous findings[9], the CD4+ T helper cells show faster dynamics than the naïve B cells. We found significantly higher mean velocities and displacement rates of T cells ($n = 165$ cells) as compared with naïve B cells ($n = 282$ cells) (Fig. 6h,i). The mean velocity of T cells amounts to $10.55 \pm 0.29\,\mu m/min$ and of B cells to $6.30 \pm 0.14\,\mu m/min$ (s.e.m.), in agreement with previously measured values for naïve B cells and T helper cells[9] as illustrated in Fig. 7d. The displacement rate of T cells amounts to $4.20 \pm 0.27\,\mu m/min$, whereas that of B cells is $1.93 \pm 0.11\,\mu m/min$ (s.e.m.).

In order to quantify the tissue burden caused by two excitation lasers as compared to one excitation laser, we compared the motility of naïve B cells in the popliteal lymph node using our triple excitation approach (Fig. 7a,b) and a single-wavelength excitation approach (Ti:Sa tuned at 930 nm, photon flux $2.2 \cdot 10^{28}$ photon/$cm^2 \cdot s$, Fig. 7c, Suppl. Video 6). We found the same mean velocity (Fig. 7d) and the same displacement rate (Fig. 7e) of naïve B cells in both cases. The imaging time window was in both cases longer than an hour, with one $40\,\mu m$ stack of images acquired every 15 s. Hence, we conclude that two excitation lasers (Ti:Sa and OPO) do not cause more cellular burden or damage than one laser (Ti:Sa). Moreover, we have previously used a neuronal Ca^{2+} reporter as an indicator of cellular dysfunction for prolonged imaging. Upon neuronal damage, their intracellular Ca^{2+}
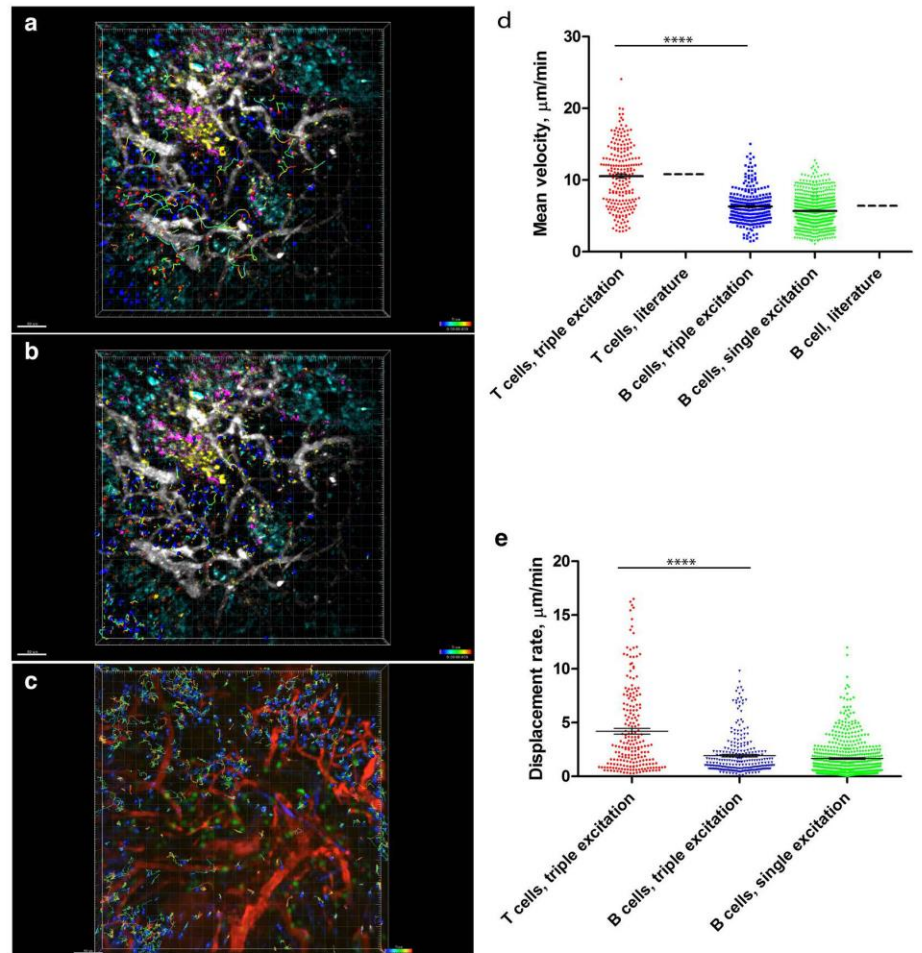
Figure 7. Naïve B and T helper cell motility patterns are similar in conventional and multiplex *in vivo* imaging, respectively, during GC reactions. (**a,b**) SIMI-unmixed time-lapsed 3D fluorescence images ($500 \times 500 \times 40\,\mu m^3$) as described in Fig. 6, with tracked CD4+ T and naïve B cells. The cell tracks are depicted as rainbow colored lines. We performed triple two-photon excitation at 850 nm (Ti:Sa), 1230 nm (OPO) and virtually at 1005 nm. (**c**) Time-lapsed 3D fluorescence images ($500 \times 500 \times 30\,\mu m^3$) in the lymph node of an anesthetized mouse, at day 7 after NP-CGG immunization. Naïve B cells labelled by Hoechst are depicted in blue, B1-8 GFP cells (GCs cells) are depicted in green and blood vessels labeled by rhodamine-dextran are shown in red. In this case, we performed a single two-photon excitation at 930 nm (Ti:Sa). Mean velocity distribution (**d**) and the displacement rate (**e**) of naïve B- and T helper cells, respectively, is significantly different, as previously reported. The absolute values of the mean velocity of both naïve B cells and T cells match the published values for B and T cell velocities[9], depicted in graph (**d**). Additionally, both the mean velocity and the displacement rate of naïve B cells after triple two-photon excitation (with Ti:Sa and OPO), obtained from (**a,b**), are the same as the values measured after single two-photon excitation (with only Ti:Sa), obtained from (**c**), as indicated in the graphs (**d**) and (**e**). Mann-Whitney non-parametric tests were used for statistical analysis of the data. (*$p < 0.05$, **$p < 0.01$, ***$p < 0.001$, ****$p < 0.0001$). Scale bars, $50\,\mu m$.

levels increase, which is visible through Förster resonance energy transfer (FRET). We imaged 3D stacks of $300 \times 300 \times 50\,\mu m^3$ every minute, over two hours at similar laser powers as described here, using dual excitation (Ti:Sa at 850 nm and OPO at 1100 nm), with no increase in neuronal calcium, i.e. no signs of neuronal dysfunction[12].

Discussion

In the last decade, *in vivo* imaging in secondary lymphoid organs has revealed unique insights into the dynamics and cellular communication during immune responses[5,9,10,38]. With regard to the germinal center reaction, imaging has helped to place key stages in B cell differentiation as well as the initiation of immunological memory in the

genuine, *in vivo* context. Still, while germinal center reactions as well as immune responses, in general, are influenced by the interplay of multiple cellular subsets and tissue compartments, conventional intravital microscopy is limited to a maximum of four colors, i.e. four distinguishable cellular and tissue compartments. In order to understand the dynamics and interactions of all contributing players *in vivo*, a multicolor intravital imaging approach is needed. While pointing in this direction, the approach of Mahou *et al.*[13] demonstrates by wave-mixing of OPO and Ti:Sa lasers only four-color dynamic deep-tissue imaging (two fluorescence signals, in addition to second and third harmonics), which is not sufficient to investigate the complexity of immune or neuronal responses *in vivo*.

We present in this work a synergistic strategy for multicolor *in vivo* imaging with three major components: wavelength mixing for simultaneous triple two-photon excitation of all components, a wide range of fluorophores from blue to near infrared, and an effective spectral unmixing approach using SIMI, our novel similarity unmixing algorithm. The combination of these methods allowed us to overcome the color limitation of current intravital imaging techniques and to monitor the interplay of dynamic cellular processes at a new level of complexity during germinal center reactions *in vivo*.

The wavelength mixing two-photon excitation is a promising approach with appealing features. Unlike sequential single-laser excitation[14], it provides the simultaneous and effective excitation of many fluorophores that is required for imaging of dynamic processes. Our synchronized two-laser approach simultaneously enables three distinct excitation opportunities, two symmetric two-photon excitations and an asymmetric two-photon excitation. It simplifies the alignment procedure as compared to the use of a three-laser system[11] by requiring the alignment of only two lasers.

The use of either supercontinuum (SC) generation and fast wavelength-switchable systems as a multiphoton excitation source may be a good alternative to multiple femtosecond-pulsed conventional laser systems for certain applications, but for several reasons these optical sources have not found yet broad application in biosciences and biomedicine. Having an extremely broad bandwidth, SC sources suffer from serious chromatic aberration, which leads to poor optical sectioning and low contrast[22]. Moreover, the lack of independent power control of different spectral ranges of both the SC generation and the fast switchable laser systems makes them unsuitable for the simultaneous excitation of fluorophores with strongly different excitation and emission properties, for which an individual power adjustment is required. The SC platforms based on coupling of femtosecond pulses into nonlinear PCF show often low spectral power density that limits their application in multi-photon microscopy, especially deep in tissue[18]. Successful applications of both ns, ps and fs SC systems as well as rapid wavelength-switchable systems for in *in vivo* multi-photon microscopy, as compared to conventional femtosecond-lasers, still need to be demonstrated.

Moreover, the palette of fluorophores and fluorescent proteins used in cell biology now spans the spectral range from deep blue to near infrared[33, 39]. We selected fluorophores covering the whole range of this available spectrum, and chose them in order to minimize spectral overlap. This strategy allowed us to increase the number of colors, which label multiple cellular and tissue players in secondary lymphoid organs, during germinal center reactions *in vivo*.

Still, the major bottleneck of simultaneous multiplexed fluorescence imaging is the ability to distinguish between multiple fluorophores. The crosstalk originating from spectral overlap of neighboring fluorophores hinders the unambiguous identification of different cell types in complex dynamic processes. In order to separate distinct colors labeling up to seven different cell and tissue compartments in the popliteal lymph node, we developed and applied the similarity-unmixing algorithm SIMI. SIMI shows distinct advantages over conventional spectral unmixing techniques. Unlike spectral deconvolution, which identifies only the reference channel (the channel with the highest intensity)[14], it takes information from all detection channels, for each fluorophore into account. For this reason, we are able to distinguish those fluorophores, which have the same reference channel but different signatures in other channels. Further, the SIMI algorithm is independent from crosstalk relations between the mixing signals, in contrast to the subtraction approach[11], in which the color discrimination is possible only for the independent crosstalk of mixed pairs. In spectrally multiplexed images, the number of detection channels often limits the number of fluorophores that can be simultaneously resolved. This restriction represents the underdetermined case, for which the widely used linear unmixing fails but our similarity algorithm remains fully functional. An appealing alternative to SIMI is the use of a phasor unmixing approach, recently demonstrated in one-photon excitation confocal microscopy of zebra fishes[40]. Since Fourier transforms needed in this approach are very sensitive to signal noise, its use has to be verified on the rather noisy emission signals originating from optically non-linear processes, like in our case.

In conclusion, simultaneous triple two-photon excitation based on wavelength mixing in combination with an extended set of fluorophores towards the near infrared opens new horizons for intravital imaging of dynamic processes in the immune system. Further, our technology opens new perspectives of functional analysis in the genuine context, if combined with FRET approaches to probe molecular parameters, and with Confetti or Brainbow mouse lines, e.g. to analyze clonal relations and competition of antigen-specific B cells during immune responses[38]. We demonstrated here that the SIMI approach is able to solve underdetermined detection problems in the case of single chromophore labeling. However, the use of our approach is not limited to such applications: to use SIMI for the analysis of FRET data, it must be extended to compare the detection signal per pixel with the linear combination of two fingerprints, i.e. of the donor and acceptor[41]. The FRET ratio results from the coefficients of the linear combination. We expect that in the future our strategy will shed light on the complexity of spatiotemporal dynamic interplay of various cell types involved in germinal center reactions, in immune niches within the bone marrow, and chronic or acute tissue inflammation of other organs, in addition to applications in neurosciences and developmental biology.

Material and Methods

Two-photon laser-scanning microscope setup. Two-photon fluorescence imaging experiments were performed as previously described[42], using a specialized laser-scanning microscope based on a commercial scan head (TriMScope II, LaVision BioTec, Bielefeld, Germany). A near-infrared laser (Ti:Sa, Chameleon Ultra II, Coherent, Dieburg, Germany) and an infrared laser (OPO, APE, Berlin, Germany) were used as excitation sources. The Ti:Sa and OPO beams, both linearly polarized, were combined in the scan head using a dichroic mirror (T1045, Chroma, US). A water-immersion objective lens (20x, NA 1.0, Plan-Apochromat, Carl Zeiss, Jena, Germany) was used to focus both laser beams into the sample. The laser pulse trains were temporally synchronized using a piezo-motorized delay stage (MS30, Qioptiq, Göttingen, Germany), while the relative divergence of the two lasers was controlled by beam expanders. The laser power was controlled by combinations of $\lambda/2$ waveplates and polarizers. The ultrashort pulses of both lasers were compressed using external compressors: a commercial two-prism-based compression for the Ti:Sa beam and a home-built single-prism compressor for OPO. Fluorescence, SHG, SFG and wavelength mixing signals were collected in the backward direction using dichroic mirror (775, Chroma, US) and directed to six photo multiplier tubes (H7422, Hamamatsu, Japan). All PMTs were assembled in a detection system with different optical channels, where every channel was determined by individual fluorescence filter and a set of dichroic mirrors as indicated in the manuscript: $466 \pm 20\,nm$, $525 \pm 25\,nm$, $562 \pm 20\,nm$, $593 \pm 20\,nm$, $617 \pm 35\,nm$, $655 \pm 20\,nm$ and $710 \pm 20\,nm$. In all imaging experiments we used an average maximum laser power of $10\,mW$ to avoid photodamage. The acquisition time for an image with a field-of-view of $500\,\mu m \times 500\,\mu m$ and a digital resolution of 1024×1024 pixel was $944\,ms$. We acquired $40\,\mu m$ z-stacks (z-step $2\,\mu m$) every $20\,s$ over a total time course of typically 30 minutes.

Data analysis. Image segmentation and tracking of all cells were performed using existing segmentation, object-recognition and tracking plugins in Imaris (Bitplane, UK). Statistical analysis of the data was performed using Graph Pad Prism. The SIMI algorithm was integrated as PlugIn in the linear unmixing PlugIn of Fiji/ImageJ written by Joachim Walter. The custom-written code is available from the authors upon request.

HEK cells transfection and imaging. We prepared two types of isolated HEK cell samples. First, we prepared samples containing HEK-293T cells expressing a single color of one out of the five FPs. For each single-labeled fluorophore, we acquired images on all six PMT channels and extracted a fingerprint, also known as a signature, of a given fluorescent protein. The fingerprint represents a ratio of relative intensities in different PMT channels and serves as the main criterion in our spectral unmixing analysis. Second, we prepared samples containing a mixture of single-labeled HEK-293T cells, each expressing one of five FPs. To achieve 'one cell – one color' labeling in the sample mixture first we transfected HEK-293T cells separately with different FP-encoding vectors, and then mixed these cells in equal proportions on one collagen-coated plate. We transfected HEK cells following the protocol provided for Lipofectamine 3000 (ThermoFischer Scientific, Waltham, MA), using vectors encoding eCFP, eGFP, mOrange2, mKate2 (Addgene, Cambridge, MA) and eqFP670 (Evrogen, Moscow, Russia).

Splenocyte isolation, labelling and imaging. We isolated splenocytes from the spleen of C57Bl/6 mice and prepared, similarly to the HEK cells, two types of isolated splenocyte samples: single color samples to acquire the spectral signatures of the chromophores and mixed samples. For the cell isolation, the spleen was cut into small pieces, pressed through a strainer and suspended in RPMI medium containing 10% FCS. Erythrocyte lysis buffer was added to the cell suspension to remove erythrocytes. The suspension was centrifuged and the pellet was resuspended in PBS. The labeling of the splenocytes was performed following existing protocols, using Hoechst, CMTPX Red, Alexa647 (ThermoFischer Scientific, Waltham, MA) and Atto680 (AttoTEC, Siegen, Germany). Splenocytes from B1-8$^{+/+}$ J$\kappa^{-/-}$ Kusabira Orange mice as well as of mice ubiquitously expressing eGFP were isolated from the spleen in a similar manner as described for C57/Bl6 mice.

Mice. All mice used were on a C57Bl/6 background. We used B1-8$^{+/+}$ J$\kappa^{-/-}$ Kusabira Orange x Blimp1-GFP mice, generated by crossing of B1-8$^{+/+}$ J$\kappa^{-/-}$ mice (kindly provided by K. Rajewski and A. Haberman) with Blimp1-GFP mice. Other experiments used F1 mice from a breeding of Rosa26-Brainbow2.1 mice[36] (obtained from Jackson Laboratories) with Rosa26-Cre^{ERT2} mice[43] (obtained from Taconic). All animal experiments were approved by Landesamt Für Gesundheit und Soziales, Berlin, Germany in accordance with institutional, state and federal guidelines.

Mouse immunization strategy. In order to a defined model of germinal center reaction in the popliteal lymph node, we immunized mice according to the scheme in Fig. 3a, as previously described[5, 37]. Therefore, we isolated B cells from B1-8$^{+/+}$ J$\kappa^{-/-}$ Kusabira Orange x Blimp1-GFP mice and mixed them with non-fluorescent B cells from non-fluorescent B1-8$^{+/+}$ J$\kappa^{-/-}$ mice at a ratio of 1:7. We transferred intravenously 10^6 isolated B cells per animal into recipient C57Bl/6 mice, one day prior to immunization with NP-CGG. In addition we isolated naïve B cells and CD4+ T cells from C57Bl/6 mice, stained them with Hoechst and cell tracker CMTPX Red, respectively, and transferred $3 \cdot 10^7$ B cells and $3 \cdot 10^7$ T cells per mouse into the recipients, five days after immunization. We injected CD21/35-Fab antibodies conjugated with Atto680 in the food pad of recipient mice 24 hours prior to imaging, in order to label the FDC network. The vasculature of the recipient mice was labeled with QD655 immediately before intravital imaging. We intravitally imaged the popliteal lymph node of the mice between day 7 and day 9 after immunization, corresponding to the peak of the germinal center reaction.

Surgical preparation of the popliteal lymph node for intravital imaging. The preparation of popliteal lymph nodes for intravital imaging was performed as previously reported[5]. Mice were anaesthetized by i.p. injection of ketamin/xylazin, according to their weight. Reflexes were tested to monitor the depth of anesthesia over the entire imaging period. The anaesthetized mouse was transferred to a custom-built surgery and

microscopy stage and fixed with dedicated tweezers. The popliteal lymph node was exposed, kept moist using isotonic 0.9% NaCl and covered with a glass cover slip of 0.13 mm thickness. A temperature of 37 °C was maintained at all times during imaging using a heating coil, and the body temperature was also maintained at 37 °C with a specialized heating foil placed under the animal. After each imaging experiment, mice were sacrificed.

Recording of two-photon spectra of various chromophores. In order to ensure optimal triple excitation of the chosen chromophores, both fluorescent proteins and dyes, we measured their two-photon excitation spectra in cells, as we previously described[12] (Fig. 2b,d; upper panels). Spectra were recorded in live cells for a better comparability with the *in vivo* situation and were measured in a wide wavelength range by the means of Ti:Sa ($760 \leq \lambda_{Ti:Sa} \leq 1040$ nm) and OPO ($1060 \leq \lambda_{OPO} \leq 1300$ nm). To achieve a continuous two-photon spectrum, the row data were corrected for background signal and peak photon flux, which includes squared laser power (measured simultaneously by reflecting about 4% of laser beams into a photodiode), photon energy in pulse peak, pulse width in focus (measured by external auto-correlator), repetition rate of lasers and excitation volume at each excitation wavelength. To avoid saturation and to support two-photon process we kept the laser power at moderate values.

Data availability. The data that support the findings of this study are available from the corresponding author upon request.

References

1. Perfetto, S. P., Chattopadhyay, P. K. & Roederer, M. Innovation - Seventeen-colour flow cytometry: unravelling the immune system. *Nat Rev Immunol* **4**, 648–U645 (2004).
2. Gerner, M. Y., Kastenmuller, W., Ifrim, I., Kabat, J. & Germain, R. N. Histo-cytometry: a method for highly multiplex quantitative tissue imaging analysis applied to dendritic cell subset microanatomy in lymph nodes. *Immunity* **37**, 364–376 (2012).
3. Schubert, W. *et al.* Analyzing proteome topology and function by automated multidimensional fluorescence microscopy. *Nat Biotechnol* **24**, 1270–1278 (2006).
4. Nimmerjahn, A., Kirchhoff, F. & Helmchen, F. Resting microglial cells are highly dynamic surveillants of brain parenchyma *in vivo*. *Science* **308**, 1314–1318 (2005).
5. Hauser, A. E. *et al.* Definition of germinal-center B cell migration *in vivo* reveals predominant intrazonal circulation patterns. *Immunity* **26**, 655–667 (2007).
6. Denk, W., Strickler, J. H. & Webb, W. W. Two-photon laser scanning fluorescence microscopy. *Science* **248**, 73–76 (1990).
7. Dittgen, T. *et al.* Lentivirus-based genetic manipulations of cortical neurons and their optical and electrophysiological monitoring *in vivo*. *Proc Natl Acad Sci USA* **101**, 18206–18211 (2004).
8. Bajenoff, M. *et al.* Natural killer cell behavior in lymph nodes revealed by static and real-time imaging. *J Exp Med* **203**, 619–631 (2006).
9. Miller, M. J., Wei, S. H., Parker, I. & Cahalan, M. D. Two-photon imaging of lymphocyte motility and antigen response in intact lymph node. *Science* **296**, 1869–1873 (2002).
10. Victora, G. D. & Nussenzweig, M. C. Germinal centers. *Annu Rev Immunol* **30**, 429–457 (2012).
11. Entenberg, D. *et al.* Setup and use of a two-laser multiphoton microscope for multichannel intravital fluorescence imaging. *Nat Protoc* **6**, 1500–1520 (2011).
12. Herz, J. *et al.* Expanding two-photon intravital microscopy to the infrared by means of optical parametric oscillator. *Biophys J* **98**, 715–723 (2010).
13. Mahou, P. *et al.* Multicolor two-photon tissue imaging by wavelength mixing. *Nat Methods* **9**, 815–818 (2012).
14. Ricard, C. & Debarbieux, F. C. Six-color intravital two-photon imaging of brain tumors and their dynamic microenvironment. *Front Cell Neurosci* **8**, 57 (2014).
15. Tang, J. Y., van Panhuys, N., Kastenmuller, W. & Germain, R. N. The future of immunoimaging - Deeper, bigger, more precise, and definitively more colorful. *Eur J Immunol* **43**, 1407–1412 (2013).
16. Quentmeier, S., Denicke, S., Ehlers, J. E., Niesner, R. A. & Gericke, K. H. Two-color two-photon excitation using femtosecond laser pulses. *J Phys Chem B* **112**, 5768–5773 (2008).
17. Lakowicz, J. R., Gryczynski, I., Malak, H. & Gryczynski, Z. Two-color two-photon excitation of fluorescence. *Photochem Photobiol* **64**, 632–635 (1996).
18. Tu, H., Boppart, S. A. Coherent fiber supercontinuum for biophotonics. *Laser Photon Rev* **7** (2013).
19. Adany, P., Price, E. S., Johnson, C. K., Zhang, R. & Hui, R. Switching of 800 nm femtosecond laser pulses using a compact PMN-PT modulator. *Rev Sci Instrum* **80**, 033107 (2009).
20. Knight, J. C. Photonic crystal fibres. *Nature* **424**, 847–851 (2003).
21. Russell, P. Photonic crystal fibers. *Science* **299**, 358–362 (2003).
22. Lefort, C. *et al.* Multicolor multiphoton microscopy based on a nanosecond supercontinuum laser source. *J Biophotonics* **9**, 709–714 (2016).
23. Weissleder, R. A clearer vision for *in vivo* imaging. *Nat Biotechnol* **19**, 316–317 (2001).
24. Shcherbakova, D. M. & Verkhusha, V. V. Near-infrared fluorescent proteins for multicolor *in vivo* imaging. *Nat Methods* **10**, 751–754 (2013).
25. Shcherbo, D. *et al.* Near-infrared fluorescent proteins. *Nat Methods* **7**, 827–829 (2010).
26. Neher, R. & Neher, E. Optimizing imaging parameters for the separation of multiple labels in a fluorescence image. *J Microsc* **213**, 46–62 (2004).
27. Zimmermann, T., Rietdorf, J., Girod, A., Georget, V. & Pepperkok, R. Spectral imaging and linear un-mixing enables improved FRET efficiency with a novel GFP2-YFP FRET pair. *FEBS Lett* **531**, 245–249 (2002).
28. Sahai, E. *et al.* Simultaneous imaging of GFP, CFP and collagen in tumors *in vivo* using multiphoton microscopy. *BMC Biotechnol* **5**, 14 (2005).
29. Garini, Y., Young, I. T. & McNamara, G. Spectral imaging: principles and applications. *Cytometry A* **69**, 735–747 (2006).
30. Fork, R. L., Martinez, O. E. & Gordon, J. P. Negative dispersion using pairs of prisms. *Opt Lett* **9**, 150–152 (1984).
31. Akturk, S., Gu, X., Kimmel, M. & Trebino, R. Extremely simple single-prism ultrashort-pulse compressor. *Opt Express* **14**, 10101–10108 (2006).
32. Cai, D., Cohen, K. B., Luo, T., Lichtman, J. W. & Sanes, J. R. Improved tools for the Brainbow toolbox. *Nat Methods* **10**, 540–547 (2013).
33. Day, R. N. & Davidson, M. W. The fluorescent protein palette: tools for cellular imaging. *Chem Soc Rev* **38**, 2887–2921 (2009).
34. Zimmermann, T. Spectral imaging and linear unmixing in light microscopy. *Adv Biochem Eng Biotechnol* **95**, 245–265 (2005).
35. Broida, J. G., Williamson, S. G. *A comprehensive introduction to linear algebra.* Addison-Wesley (1989).

93

36. Snippert, H. J. *et al.* Intestinal crypt homeostasis results from neutral competition between symmetrically dividing Lgr5 stem cells. *Cell* **143**, 134–144 (2010).
37. Roth, K. *et al.* Tracking plasma cell differentiation and survival. *Cytometry A* **85**, 15–24 (2014).
38. Tas, J. M. *et al.* Visualizing antibody affinity maturation in germinal centers. *Science* **351**, 1048–1054 (2016).
39. Rodriguez, E. A. *et al.* The Growing and Glowing Toolbox of Fluorescent and Photoactive Proteins. *Trends Biochem Sci* (2016).
40. Cutrale, F. *et al.* Hyperspectral phasor analysis enables multiplexed 5D *in vivo* imaging. *Nat Methods* (2017).
41. Bremer, D. *et al.* Longitudinal Intravital Imaging of the Retina Reveals Long-term Dynamics of Immune Infiltration and Its Effects on the Glial Network in Experimental Autoimmune Uveoretinitis, without Evident Signs of Neuronal Dysfunction in the Ganglion Cell Layer. *Front Immunol* **7**, 642 (2016).
42. Andresen, V. *et al.* High-resolution intravital microscopy. *PLoS One* **7**, e50915 (2012).
43. Seibler, J. *et al.* Rapid generation of inducible mouse mutants. *Nucleic Acids Res* **31**, e12 (2003).

Acknowledgements

Author Contributions

A.R., A.E.H. and R.A.N. designed the study, analyzed data and interpreted results. A.R., R.L., H.Z., R.G., P.M., A.A., C.U., D.R. and A.U.B. performed experiments. A.E.H., R.L.L. and T.H.W. provided expertise for the design of the experiments concerning germinal center reactions. A.R., R.L.L., R.A.N. and A.E.H. wrote the manuscript.

Additional Information

Supplementary information accompanies this paper at doi:10.1038/s41598-017-07165-0

Competing Interests: The authors declare that they have no competing interests.

Publisher's note: Springer Nature remains neutral with regard to jurisdictional claims in published maps and institutional affiliations.

94

SYNERGISTIC STRATEGY FOR MULTICOLOR TWO-PHOTON MICROSCOPY: APPLICATION TO THE ANALYSIS OF GERMINAL CENTER REACTIONS IN VIVO

ASYLKHAN RAKHYMZHAN, RUTH LEBEN, HANNA ZIMMERMANN, ROBERT GÜNTHER, PEGGY MEX, DAVID REISMANN, CAROLIN ULBRICHT, ANDREAS ACS, ALEXANDER U. BRANDT, RANDALL L. LINDQUIST, THOMAS H. WINKLER, ANJA E. HAUSER, RALUCA A. NIESNER
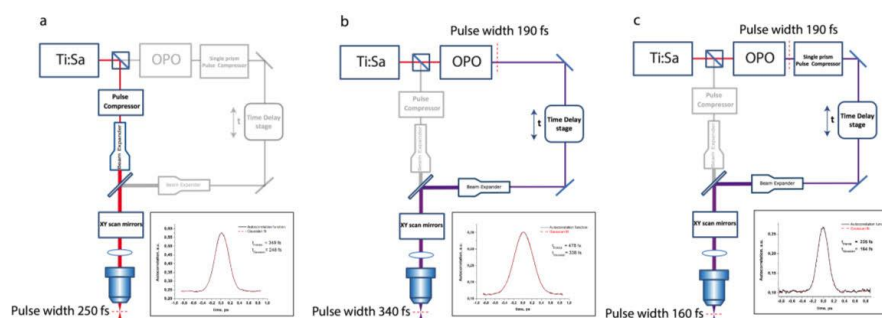
SUPPLEMENTARY FIGURES

FIGURE S1

PULSE WIDTH OF TI:SA AND OPO LASERS IN THE MICROSCOPE WITH AND WITHOUT PULSE COMPRESSION. The pulse width of both Ti:Sa and OPO was measured using an optical auto-correlator (APE, Berlin, Germany), based on the second harmonic generation of birefringent KDP powder in the two-photon microscope. (a) The Ti:Sa pulse width was measured only with a conventional "two-prism" pulse compressor. (b, c) The OPO pulse width was measured without and with a single-prism pulse compressor, respectively. The pulse compression of the OPO beam was achieved using the single-prism design described in Fig. 1b. Having all positive features of two-prism configuration, the single-prism design offers many advantages over conventional prism-based pulse compressors. Significantly simplified alignment is achieved due to the

corner cube optical properties of anti-parallel beam reflection and precise compensation of the spatiotemporal distortions (angular and spatial dispersion, pulse-front-tilt) in the output beam. It is also very compact because the beam double-passes the prism corner cube path, which is half the size of the two-prism design. The wavelength tuning is achieved by rotation only one prism, unlike in the two-prism configuration, where proper angles of two prisms have to be maintained.
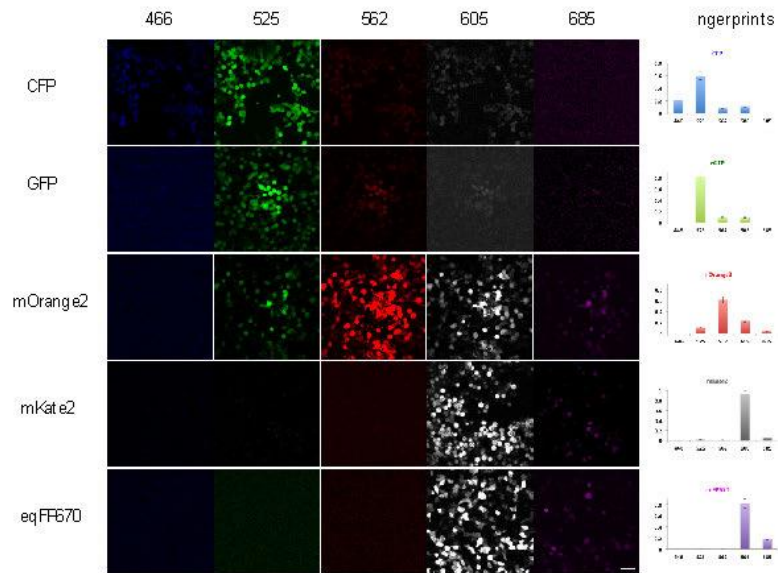
FIGURE S2

FINGERPRINT ASSESSMENT IN SINGLE-COLOR CONTROLS OF HEK CELLS. The single-color controls of isolated HEK cells were excited at 850 nm, 1230 nm, by spatially overlapped wavelengths with pulse trains synchronization. Their fluorescence signal was detected on five PMTs, as previously described (Fig. 1a). Each row illustrates images of HEK cells on five detection channels corresponding to one of the fluorescent proteins with its fingerprint. Scale bar, 50 µm.
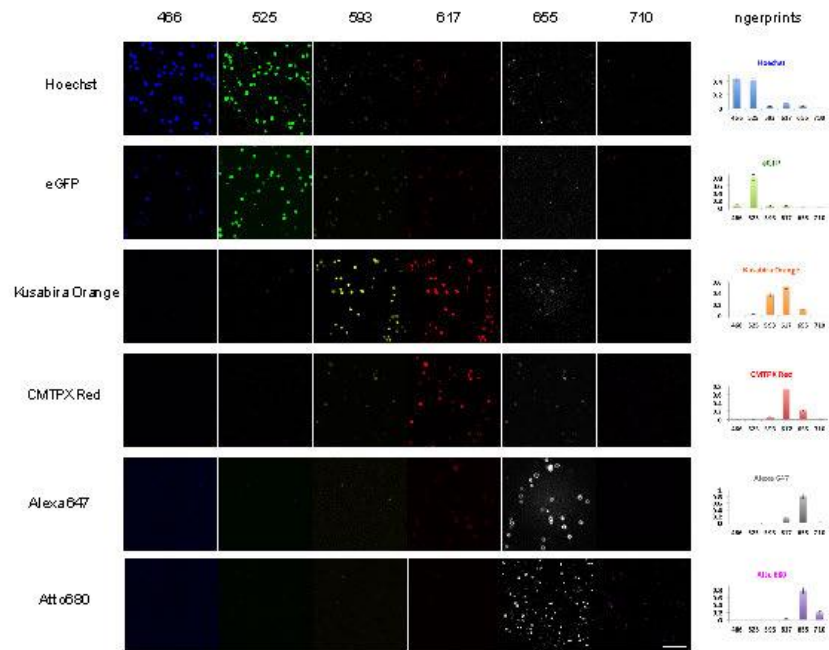
FIGURE S3

FINGERPRINT ASSESSMENT IN SINGLE-COLOR CONTROLS OF SPLENOCYTES. The single-color controls of isolated splenocytes were excited at 850 nm, 1230 nm, by both spatially overlapped wavelengths with pulse trains synchronization. Their fluorescence signal was detected on six PMTs, as previously described (Fig. 1a). Each row illustrates images of splenocytes on six detection channels corresponding to one of the fluorophores with its fingerprint. Scale bar, 50 μm.
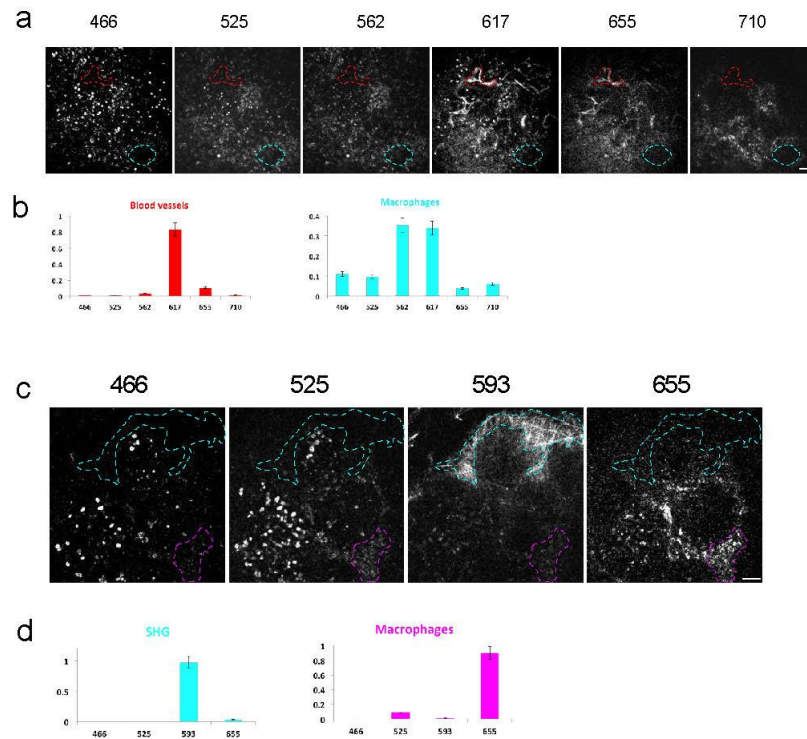
FIGURE S4

IN SITU ACQUIRED FINGERPRINTS OF THE SIGNALS USED FOR INTRAVITAL IMAGING OF GERMINAL CENTER REACTIONS AND FOR THE UNDERDETERMINED CASE *IN VIVO*.

(a, b) Raw data and fingerprints of machrophages and blood vessels from intravital measurement of popliteal lymph node (Fig. 6c). Macrophages, including tingible body macrophages, show a autofluorescent signal in the intravital raw data, which helped us to generate their specific fingerprint from the dashed area (colored cyan), containing only the macrophages autofluorescent signal, and ultimately, to resolve them from other cellular compartments in lymph node imaging. The fingerprint of blood vessels, stained by quantum dots 655, was also acquired *in situ*, since its structure can be easily determined from the raw data (dashed area colored red). (c, d) Raw data and fingerprints of SHG from collagen fibers and machrophages from in vivo measurement of popliteal lymph node at the underdetermined condition (Fig.

5e). Signals from SHG and macrophages can be easily identified on the raw data (dashed areas colored cyan and magenta, respectively). The SHG signal appears in only one detection channel. Scale bars, 50 μm.
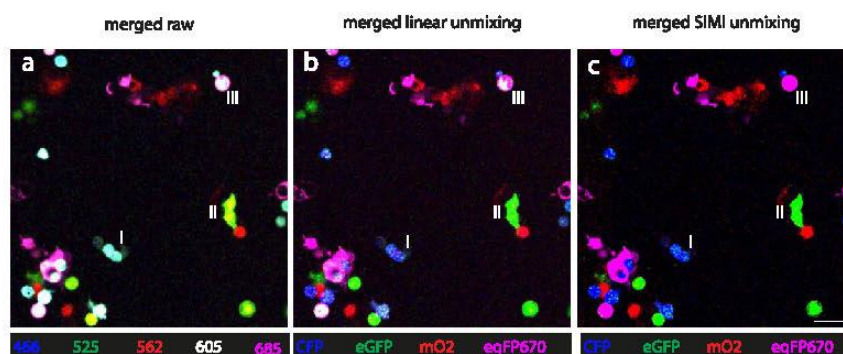
FIGURE S5

COMPARISON OF LINEAR UNMIXING AND SIMI ALGORITHM ON HEK CELLS IMAGE.

(a) Merged raw image of HEK cells mixture expressing four fluorescent proteins: CFP, eGFP, mOrange2 and eqFP670. Some cells, examples denoted by I, II and III, show a significant crosstalk on five channels. (b) Merged image processed by linear unmixing approach. The cases I and II, assigned as CFP and eGFP, respectively, demonstrate full color unmixing. The linear unmixing was incapable to determine the case III cells. (c) Merged image processed by SIMI algorithm. All cases, I, II and III, were completely assigned as CFP, eGFP and eqFP670, respectively. The SIMI algorithm demonstrates higher spectral unmixing capacity in compare with the linear unmixing approach. Scale bar, 50 μm.

MOVIE CAPTIONS

S VIDEO 1

DEPENDENCE OF SUM FREQUENCY GENERATION IN POTASSIUM DIHYDROGEN PHOSPHATE (KDP) POWDER ON THE OVERLAP OF TI:SA AND OPO PULSE TRAINS. (a) SHG signal from 850 nm on blue channel (447±30 nm). (b) Sum frequency generation of OPO (1230 nm) and Ti:Sa (850 nm) lasers in birefringent KDP powder is detected on green channel (525±25) at 502 nm only if their pulse trains overlap and disappears if the pulse trains are shifted with respect to each other, thus, generating a cross-correlation signal of the two lasers. (c) The OPO pulse train moves with respect to the Ti:Sa pulse train by changing the optical path length of the OPO beam into the microscope. Therefore, a delay stage consisting of two 90° prisms is used, one of the prisms being mounted on a piezo stage allowing for its translation as shown in Fig. 1a. The step of the piezo motor is 15 nm, corresponding to 50 attoseconds. (d) SHG signal from 1230 nm on red channel (617±35 nm).

S VIDEO2

DEPENDENCE OF MORANGE2 FLUORESCENCE SIGNAL EXPRESSED BY HEK CELLS ON THE OVERLAP OF TI:SA AND OPO PULSE TRAINS. Similar to SFG, the mOrange2 fluorescence can be detected at 562 nm only if the pulse trains of Ti:Sa and OPO overlap and disappears if the pulse trains are shifted with respect to each other (inset video), thus generating a cross-correlation signal of the two lasers.

S VIDEO3

INTRAVITAL SPECTRALLY MULTIPLEXED IMAGING OF A GERMINAL CENTER. Left: raw video. Right: video processed by SIMI algorithm. Time-lapse 3D fluorescence imaging of germinal centers (500x500x40 μm^3) in the popliteal lymph node of a mouse immunized with NP-CGG recorded after triple wavelength mixing excitation at 850 nm (Ti:Sa) and 1230 nm (OPO). The signals of naïve B cells (Hoechst, blue), germinal center B1-8 cells (Kusabira Orange, yellow), plasma blasts (Blimp1 GFP, green), CD4+ follicular T helper cells (CMTPX, red), follicular dendritic cells (CD21/35-Fab-ATTO680, magenta), blood vessels (QD655, grey) and macrophages including tingible body macrophages (autofluorescence, cyan) could be detected and resolved over time. 3D images were recorded every 20 s, the z-step was 2 μm.

S VIDEO4

INTRAVITAL SPECTRALLY MULTIPLEXED IMAGING OF A GERMINAL CENTER –
TRACKING CD4+ T CELLS. Time-lapse 3D fluorescence imaging of germinal
centers (500x500x40 μm^3) in the popliteal lymph node of the same mouse
immunized with NP-CGG recorded after triple wavelength mixing excitation at
850 nm (Ti:Sa) and 1230 nm (OPO). The colored track paths shown in the right
video indicate the tracks of CD4+ T helper cells.

S VIDEO5

INTRAVITAL SPECTRALLY MULTIPLEXED IMAGING OF A GERMINAL CENTER –
TRACKING NAIVE B CELLS. Time-lapse 3D fluorescence imaging of germinal
centers (500x500x40 µm^3) in the popliteal lymph node of the same mouse
immunized with NP-CGG recorded after triple wavelength mixing excitation at
850 nm (Ti:Sa) and 1230 nm (OPO). The colored track paths shown in the right
video indicate the tracks of naive B cells.

S VIDEO6

INTRAVITAL SINGLE EXCITATION IMAGING OF A GERMINAL CENTER − TRACKING NAIVE B CELLS. Time-lapse 3D fluorescence imaging of germinal centers (500x500x40 μm^3) in the popliteal lymph node of the B1-8 Jk-/- GFP mouse immunized with NP-CGG recorded after single excitation at 930 nm (Ti:Sa). The colored track paths shown in the left video indicate the tracks of naive B cells. The signals of naïve B cells (Hoechst, blue), germinal center B cells (GFP, green), blood vessels (rhodamin dextran, red) could be detected and resolved over time. 3D images were recorded every 20 s, the z-step was 2 μm.

7. Declaration of shareholding in the publications made

I, David Reismann, contributed as follows to the following publications:

Publication 1

David Reismann, Jonathan Stefanowski, Robert Günther, Asylkhan Rakhymzhan, Romano Matthys, Reto Nützi, Sandra Zehentmeier, Katharina Schmidt-Bleek, Georg Petkau, Hyun-Dong Chang, Sandra Naundorf, York Winter, Fritz Melchers, Georg Duda, Anja Hauser, Raluca Niesner; **Longitudinal intravital imaging of the femoral bone marrow reveals plasticity within marrow vasculature**. Nature Communications, 2017.

DOI: 10.1038/s41467-017-01538-9

Contribution in detail:

Mainly contributing to the development and design of the implant and the setup for microscopy (Fig. 1 a-d; Suppl. Fig. 1,2), the imaging microendoscopes (Fig. 1 d) and the procedure of the surgical operations, as well as performing them (Suppl. Fig. 3).

Generation and evaluation of the intravital data from the LIMB experiments (Fig. 1 e, h, i; 4 a, b, e; 5 a; 6 a-d; 7 c; Suppl. Fig. 6;9;10; Suppl. Movie 3;5-7,10-13), as well as contributing to the generation and evaluation of intravital data from tibia and calvarium (Fig. 4 c-e; 5 b; 6 e.; Suppl. Fig. 7; Suppl. Movie 4,8).

Generation and interpretation of ex vivo µCT scans (Fig. 2 b, c, f; Suppl. Movie 1).

Monitoring and interpretation of the activity and behavior of the operated animals (Fig. 2 h; Suppl. Movie 2).

Contributing to the generation and interpretation of histological analyses (Fig. 3 a-f; 7 a, b; Suppl. Fig. 4;8).

Contributing to the preparation and review of the manuscript.

Publication 2

Asylkhan Rakhymzhan, Ruth Leben, Hanna Zimmermann, Robert Günther, Peggy Mex, **David Reismann**, Carolin Ulbricht, Andreas Acs, Alexander Brandt, Randall Lindquist, Thomas Winkler, Anja Hauser, Raluca Niesner; **Synergistic strategy for multicolor two-photon microscopy: application to the analysis of germinal center reactions in vivo.** Scientific Reports; 2017.

DOI: 10.1038/s41598-017-07165-0

Contribution in detail:

Contributing to the selection and purification of plasmids.

Performing imaging experiments on transfected HEK cells and splenocytes.

Support in installing the pulse compressor and testing the delay stage.

Berlin,

D. Reismann

8. Eidesstattliche Erklärung

David Reismann

Wendenschloßstr. 257

12557 Berlin, Deutschland

Hiermit erkläre ich, David Reismann, dass ich die vorliegende Arbeit selbstständig, ohne unerlaubte fremde Hilfe und ausschließlich unter Verwendung der aufgeführten Quellen und Hilfsmittel angefertigt habe.

Berlin,

_____

D. Reismann

9. CV

The CV has been removed for data protection reasons

The CV has been removed for data protection reasons

The CV has been removed for data protection reasons